

A New Technique for Measuring Polycyclic Aromatic Hydrocarbon Emission in Different Environments

Yanxia Xie¹, Luis C. Ho^{1,2}, Aigen Li³, and Jinyi Shangguan²

ABSTRACT

We present a new method to decompose the emission features of polycyclic aromatic hydrocarbons (PAHs) from mid-infrared spectra using theoretical PAH templates in conjunction with modified blackbody components for the dust continuum and an extinction term. The primary goal is to obtain robust measurements of the PAH features, which are sensitive to the star formation rate, in a variety of extragalactic environments. We demonstrate the effectiveness of our technique, starting with the simplest Galactic high-latitude clouds to extragalactic systems of ever-increasing complexity, from normal star-forming galaxies to low-luminosity active galaxies, quasars, and heavily obscured infrared-luminous galaxies. In addition to providing accurate measurements of the PAH emission, including the upper limits thereof, our fits can reproduce reasonably well the overall continuum shape and constrain the line-of-sight extinction. Our new PAH line flux measurements differ systematically and significantly from those of previous methods by $\sim 15\%$ to as much as a factor of ~ 6 . The decomposed PAH spectra show remarkable similarity among different systems, suggesting a uniform set of conditions responsible for their excitation.

Subject headings: dust, extinction — galaxies: active — galaxies: ISM — galaxies: nuclei — galaxies: Seyfert — infrared: ISM

1. Introduction

Quantifying star formation in galaxies is essential to understanding their evolution. To this end, different observables have been used to calibrate the star formation rate in galaxies

¹Kavli Institute for Astronomy and Astrophysics, Peking University, Beijing 100871, China; yanxia.xie@pku.edu.cn, lho.pku@gmail.com

²Department of Astronomy, School of Physics, Peking University, Beijing 100871, China, shangguan@pku.edu.cn

³Department of Physics and Astronomy, University of Missouri, Columbia, MO 65211, USA lia@missouri.edu

(Kennicutt & Evans 2012). The emission features from polycyclic aromatic hydrocarbons (PAHs) have long been proposed as a useful tracer of star formation on galactic scales. Peeters et al. (2004) showed that local star-forming regions and nearby starburst galaxies obey a tight empirical correlation between the $6.2\ \mu\text{m}$ PAH emission feature and the far-infrared (FIR) luminosity, implying that the PAH $6.2\ \mu\text{m}$ feature is an effective tracer of the star formation rate. The advent of the *Infrared Space Observatory* and especially the Infrared Spectrograph (IRS) onboard the *Spitzer Space Telescope* (Houck et al. 2004; Werner et al. 2004) has enabled the unambiguous detection of a set of distinct spectral features at 3.3 , 6.2 , 7.7 , 8.6 , and $11.3\ \mu\text{m}$, which are ubiquitously detected in the mid-infrared (MIR) spectra of a variety of Galactic and extragalactic sources. For instance, these features are seen in protoplanetary disks around intermediate-mass, pre-main-sequence Herbig Ae/Be stars (e.g., Acke et al. 2010), and their low-mass analog T Tauri stars (e.g., Geers et al. 2006), as well as debris disks around main-sequence stars (e.g., Seok & Li 2015). Moreover, they are also prevalent in external star-forming and starburst galaxies, accounting for more than 10% of their total IR luminosity (Smith et al. 2007; Tielens 2008). The relatively broad wavelength coverage and prominence of these bands facilitate their detection in star-forming regions both in local and distant (e.g., $z \gtrsim 1$) galaxies (e.g., Huang et al. 2009; Magdis et al. 2011). The emission feature at $11.3\ \mu\text{m}$ can be robustly detected even in some active galactic nuclei (AGNs; Alonso-Herrero et al. 2014, 2016). The exact nature of the carriers of these emission bands remains unknown, with PAHs being the leading candidate (e.g., Léger & Puget 1984; Allamandola et al. 1985). The PAH molecules are transiently heated by ultraviolet (UV) photons from newly formed stars, and they are predominantly associated with photodissociation regions. The observed close coupling between PAH molecules and star-forming regions supports this hypothesis.

Rigorous application or interpretation of the PAH features requires that they be quantitatively measured. This is challenging, however, for several reasons. First, the PAH features lie on top of a complex continuum, whose intrinsic underlying shape is quite uncertain because it arises, depending on the physical nature of the source, from the superposition of dust emission from different components with different temperatures. The AGNs complicate matters further by introducing very hot dust from a central torus. At the shortest IR wavelengths, even stellar emission may be nonnegligible. Second, the PAH lines have intrinsically broad, extended profiles, which, in concert with their close wavelength separations, render them heavily blended, especially given the rather low spectral resolution of instruments such as the IRS. In the spectral region $\sim 6\text{--}9\ \mu\text{m}$, for example, there are so many overlapping PAH features that it is almost impossible to define a line-free continuum region. Moreover, some PAH features are also blended with ionic fine-structure lines (e.g., the $12.7\ \mu\text{m}$ PAH feature with the $12.8\ \mu\text{m}$ [Ne II] line). Lastly, all of the above components, line and continuum, may

be affected further by the broad silicate emission or absorption features at ~ 10 and $\sim 18 \mu\text{m}$. Dust absorption is especially severe in some of the most luminous, high-redshift systems.

PAHFIT is one of the most popular tools used to decompose MIR spectra of galaxies (Smith et al. 2007). This technique fits the underlying continuum with a combination of stellar continuum, represented by blackbody emission with a temperature fixed at 5000 K, plus eight modified blackbodies with preassigned temperatures (from 35 to 300 K) to reproduce the dust continuum. The PAH features are modeled simultaneously with Drude functions of fixed full width at half maximum (FWHM) and wavelength positions, and single Gaussian functions are added to fit the molecular hydrogen and ionic fine-structure lines.

Another frequently used method performs a spline fit to continuum anchor points apparently free of line emission, and the PAH flux is derived by integrating the line emission above the local continuum (e.g., Peeters et al. 2004; Brandl et al. 2006). In this approach, the choice of continuum anchor points strongly depends on the subjective, visual inspection of the spectrum, which varies greatly from galaxy to galaxy. Moreover, as mentioned previously, the broad, overlapping PAH features have such extended wings that there are hardly any truly line-free continuum regions available. Comparison between PAH strengths measured using PAHFIT and spline fit shows large scatter and systematic discrepancies. In general, the spline fit method underestimates the PAH line fluxes by factors of ~ 2 – 6 , depending on the feature (Smith et al. 2007).

In their spectral energy distribution (SED) fitting software “Continuum And Feature Extraction” (CAFE), Marshall et al. (2007) constructed a semiempirical PAH template by applying PAHFIT to an average spectrum of starburst galaxies (Brandl et al. 2006). After subtracting the continuum, they extracted individual profiles for a large number of PAH features between ~ 3 and $19 \mu\text{m}$. CAFE fits the SED in two steps. In the first step, a model is fit to the continuum after the PAH template is subtracted from the overall spectrum. Then, the residual, continuum-subtracted PAH spectrum is fit by adjusting the strengths of individual PAH features.

This paper presents a new technique to measure the PAH features in the MIR spectra of galaxies by making use of a theoretically calculated PAH template in combination with three dust components, allowing all the parameters to vary simultaneously and self-consistently. We illustrate the effectiveness of our method by applying it first to one of the simplest environments in which PAH emission is found, the Galactic high-latitude clouds (HLCs; Blitz et al. 1984; Magnani et al. 1985). We then extend it to a range of extragalactic systems of increasing levels of complexity, from nearby normal star-forming galaxies, to AGNs with a range of activity spanning low-ionization nuclear emission-line regions (LINERs; Heckman 1980) to Seyferts and quasars, and finally to highly obscured ultraluminous IR galaxies

(ULIRGs). Our technique can measure the absolute strength of the PAH emission features and derive upper limits on them when undetected. At the same time, we can describe the underlying dust continuum with a minimum number of dust components (Y. Xie et al. 2018, in preparation) and simultaneously solve for the line-of-sight extinction.

We organize the paper as follows. Section 2 introduces the MIR spectra used in the paper. Section 3 explains our new method and describes the different components that make up our model. The application of the new method to objects of different levels of complexity is presented in §4. We discuss the implications of our results in §5 and summarize in §6.

2. MIR Emission Features and *Spitzer*/IRS Spectroscopic Data

The MIR spectrum of galaxies contains rich information on gas and dust. A wealth of ionic emission lines of different ionization potentials and levels (e.g., [S IV] 10.51 μm , [Ne II] 12.81 μm , [Ne III] 15.56 μm , [Ne V] 14.32, 24.32 μm , [S III] 18.71, 33.48 μm , [O IV] 25.8 μm , [Si II] 34.82 μm) provides powerful tools to diagnose the excitation, density, and metallicity of the ionized gas (e.g., Genzel et al. 1998; Lutz et al. 1998; Dale et al. 2006; Hao et al. 2009; Veilleux et al. 2009; Sargsyan et al. 2011). The MIR spectral range also covers a suite of pure rotational lines of molecular hydrogen: H₂ *S*(6) 6.11 μm , H₂ *S*(5) 6.91 μm , H₂ *S*(4) 8.03 μm , H₂ *S*(3) 9.67 μm , H₂ *S*(2) 12.27 μm , H₂ *S*(1) 17.03 μm , and H₂ *S*(0) 28.22 μm , among which H₂ *S*(5) 6.91 μm is blended with [Ar II] 6.99 μm . Dust emission features are key components in the MIR. Apart from PAH emission at 6.2, 7.7, 8.6, 11.3, 12.7, 16.4, and 17.1 μm , silicate dust exhibits two broad bumps/troughs at ~ 10 and ~ 18 μm . Here [Ne II] 12.8 μm is blended with PAH 12.7 μm , and H₂ *S*(1) 17.03 μm is blended with PAH features at 16.4 and 17.1 μm . To complicate matters further, the line emission sits on top of continuum emission from dust spanning a range of temperatures and grain sizes. In particular, the MIR region contains continuum emission from very small grains that are heated via single-photon absorption (Y. Xie et al. 2018, in preparation). The main dust and gas features are illustrated in Figure 1.

All of the MIR spectra data used in the current paper were obtained with the IRS instrument onboard *Spitzer*. The IRS has both a low-resolution and a high-resolution mode. The low-resolution data cover the 5.2–38 μm wavelength range with a resolving power of $R \equiv \lambda/\Delta\lambda = 57 - 128$; the high-resolution mode covers 9.9–37.2 μm with $R \approx 600$. The low-resolution spectra are split into the short low (SL; $\lambda < 14$ μm) and the long low (LL; $\lambda \gtrsim 14.5$ μm) modes. In particular, the main PAH features populate the SL spectra, which, unfortunately, have a lower signal-to-noise ratio because the slit size of the SL mode is ~ 3 times smaller than that of the LL mode.

For the data utilized in this paper, we give priority to the spectra archived in the Cornell AtlaS of *Spitzer*/IRS Sources (CASSIS), which were extracted according to the extent of the sources. CASSIS includes $\sim 13,000$ low-resolution spectra of $> 11,000$ distinct sources observed in standard staring mode and provides publishable-quality spectra (Lebouteiller et al. 2011). Spectra for galaxies not included in CASSIS were collected from the literature. For the Galactic HLCs, Ingalls et al. (2011) published spectra of 15 clouds that have strong molecular hydrogen-line emission in the MIR. Our analysis includes the four HLCs that have complete IRS low-resolution spectra from 5 to $38 \mu\text{m}$. The reduced spectra for nearby star-forming galaxies and low-luminosity AGNs are taken from the NASA/IPAC InfraRed Science Archive (IRSA).¹

3. Methodology

We develop a new technique to decompose MIR IRS spectra into their dominant emission components from PAH features and the dust continuum, simultaneously accounting for dust extinction. Our technique greatly reduces the number of free parameters (to eight in total) and is easy to apply to astronomical sources with various levels of complexity. We adopt a linear combination of a theoretical template for PAH emission, three modified blackbodies for the continuum, plus an extinction component. After shifting the spectra to the rest frame, we mask strong, unblended ionic and molecular hydrogen emission lines, assuming that the lines are unresolved at the minimum instrumental resolution of $\text{FWHM} = 0.34 \mu\text{m}$. We do not mask or attempt to fit [Ne II] $12.8 \mu\text{m}$ and $\text{H}_2 S(1)$ $17.03 \mu\text{m}$, both of which are blended with PAH features, because their intensity is negligible compared to that of PAH emission and will not affect the fit significantly.

In light of the complexity of the spectral region in question, we perform the analysis in a stepwise fashion, starting with fits to the relatively simple Galactic HLCs and then proceeding to extragalactic environments of ever-increasing complexity, from star-forming galaxies, to low-luminosity active galaxies, to more powerful quasars, and finally to highly obscured AGNs and nuclear starbursts in ULIRGs. The luminous sources encompass a wide range of PAH strengths, from objects with unambiguously strong features to those with barely any signs of PAH emission, for which we are able to place meaningful upper limits.

¹<http://irsa.ipac.caltech.edu/data/SPITZER/SINGS/>

3.1. The Model

The spectral model used to fit the MIR spectra contains five components: three modified blackbodies of different temperatures (hot, warm, and cold) to represent the continuum emission, a theoretical PAH template calculated from Draine & Li (2007), and an extinction term that affects the continuum and line emission. The model, expressed as

$$F_\nu(\text{mod}) = [A^{\text{PAH}} J_\nu^{\text{PAH}} + A^h B_\nu(T^h)/\lambda^\beta + A^w B_\nu(T^w)/\lambda^\beta + A^c B_\nu(T^c)/\lambda^\beta] \exp(-\tau_\lambda), \quad (1)$$

contains eight free parameters: the scale factor A^{PAH} of the PAH template J_ν^{PAH} ; the scale factors A^h , A^w , and A^c for the hot, warm, and cold dust components represented as modified blackbodies $B_\nu(T)$ of temperature T^h , T^w , and T^c ; the dust emissivity index β , assumed to be the same for all three modified blackbodies and fixed² to $\beta = 2$; τ_λ , is the total optical depth applied to all components, with $\tau_\lambda = \tau_{9.7} \times (A_\lambda/A_{9.7})$, where $A_\lambda/A_{9.7}$ is the interstellar extinction curve of Wang et al. (2015) normalized at $9.7 \mu\text{m}$ (Figure 2) and $\tau_{9.7}$ is the optical depth at $9.7 \mu\text{m}$, the only adjustable parameter for the extinction term.

In principle, the observed MIR continuum arises from a mixture of dust components spanning a wide range of temperatures. However, as we have very limited constraints on the exact dust temperature distribution, we simply adopt a minimum number (three) of modified blackbodies to represent the dust continuum emission. The temperatures derived from the current model should only be regarded as representative of the average values of certain dust components.

3.2. Theoretical PAH Template

The PAH model attributes the observed 3.3, 6.2, 7.7, 8.6, 11.3, and $12.7 \mu\text{m}$ features to the vibrational modes of PAHs, with the $3.3 \mu\text{m}$ feature assigned to C–H stretching modes, the 6.2 and $7.7 \mu\text{m}$ features to C–C stretching modes, the $8.6 \mu\text{m}$ feature to C–H in-plane

²Assuming that all dust particles are spherical and are composed of electrons and ions, they can be treated as a dipole of a classical Lorentz harmonic oscillator, oscillating under the force of an electromagnetic field. For submicron-sized grains and very small grains that satisfy the Rayleigh limit in the IR ($2\pi a/\lambda \ll 1$), the absorption by dust of incident radiation can be approximated as $\sim \lambda^{-2}$ (i.e., $\beta = 2$), in accordance with the solution for the motion of a harmonic oscillator, where λ is the wavelength of the incident electromagnetic wave. In practical situations, β may vary from ~ 1.5 to ~ 2 , which indicates that the vibration of the dust grain deviates from that of ideal harmonic oscillation (see Draine 2003 and Li 2009 for more details). The determination of the exact value of β requires full information on the IR SED. In this paper, we fix β to 2.

bending modes, and the 11.3 and 12.7 μm features to C–H out-of-plane bending modes (Léger & Puget 1984; Allamandola et al. 1985). The relative strengths of these bands depend on the charge, size, and molecular structure of the PAH molecule (see Li 2004). While the emission from ionized PAHs dominates at 6.2, 7.7, and 8.6 μm , neutral PAHs emit strongly at 3.3 and 11.3 μm (see Hudgins & Allamandola 2004 and references therein). On the other hand, with a larger heat capacity—which is proportional to N_C , the number of C atoms—a larger PAH molecule will be heated to a lower peak temperature (i.e., $T_{\text{peak}} \propto N_C^{-1/4}$) upon absorption of a single stellar photon. Therefore, the bulk emission of larger PAHs occurs at longer wavelengths than that of smaller PAHs (Li & Mann 2012). Finally, compared to catacondensed PAHs, which have a more open structure, compact, pericondensed PAHs (e.g., coronene, ovalene, and circumcoronene) have a lower hydrogen-to-carbon ratio (H/C). Thus, for PAHs of the same size (i.e., N_C), pericondensed PAHs are expected to have a lower 11.3–7.7 μm band ratio (e.g., Hony et al. 2001; Vermeij et al. 2002; Shannon et al. 2016).

The PAH model readily explains the general PAH band patterns observed in various regions in terms of a mixture of neutral and charged PAHs of different sizes (e.g., see Allamandola et al. 1999; Li & Draine 2001; Peeters et al. 2004; Draine & Li 2001; Bauschlicher et al. 2010; Cami et al. 2011; Rosenberg et al. 2011; Boersma et al. 2013, 2014; Andrews et al. 2015). Draine & Li (2007) calculated the IR emission spectra of PAHs³ for the Galactic diffuse interstellar medium (ISM), with the PAH charging⁴ determined from the balance between photoionization and electronic recombination (Bakes & Tielens 1994; Weingartner & Draine 2001b), and with the PAH size distribution constrained by the broadband photometric data of *COBE*/DIRBE at 3.5, 4.9, 12 and 25 μm , together with the spectroscopic data at 2.8–12 μm obtained by the *Infrared Telescope in Space* (Onaka et al. 1996; Tanaka et al. 1996) and 5–40 μm data from *Spitzer*/IRS (Smith et al. 2007).⁵

Li & Draine (2001) unified PAHs and graphite into a single population of dust grains:

³The PAHs are assumed to be compact and pericondensed, as catacondensed PAHs are less stable in hostile interstellar environments (see Eq. 4 of Li & Draine 2001).

⁴The PAH charging is measured by the PAH ionization fraction ϕ_{ion} , the probability of finding a PAH molecule in a nonzero charge state. It depends on the quantity $U\sqrt{T_{\text{gas}}/n_e}$ (Bakes & Tielens 1994; Weingartner & Draine 2001b), where U is the starlight density in units of the solar neighborhood interstellar radiation field (ISRF; Mathis et al. 1983, hereafter MMP83), T_{gas} is the gas temperature, and n_e is the electron number density.

⁵The Galactic UV extinction curve cannot constrain the size distribution of PAHs because, even in the far-UV, PAHs are in the Rayleigh regime, and the extinction cross sections of PAHs on a per unit volume basis are size-independent; therefore, the UV extinction curve only constrains the quantity of PAHs, not the detailed size distribution (Wang et al. 2015).

“carbonaceous” grains. The so-called carbonaceous grain population extends from grains with graphitic properties at radii $a \gtrsim 50 \text{ \AA}$ down to particles with PAH-like properties at very small sizes.⁶ Using the size-distribution functional form of Weingartner & Draine (2001a), Draine & Li (2007) described the size distribution of the carbonaceous grain population with two lognormal components and a component similar to an exponentially cut off power law. The lognormal components are for PAHs and are characterized by the peak size $a_{0,j}$ (where $j = 1, 2$), the width σ_j , and $(\text{C}/\text{H})_j$, the amount of C (relative to H) locked up in each component. Draine & Li (2007) derived the best-fit parameters to be $a_{0,1} \approx 4 \text{ \AA}$, $\sigma_1 \approx 0.4$, and $(\text{C}/\text{H})_1 \approx 45 \text{ ppm}$ (where ppm refers to parts per million) for the smaller component and $a_{0,2} \approx 20 \text{ \AA}$, $\sigma_2 \approx 0.55$, and $(\text{C}/\text{H})_2 \approx 15 \text{ ppm}$ for the larger component. For these lognormal components, the mass distributions peak at $a_{0,j} \exp(3\sigma_j^2) \approx 6.5 \text{ \AA}$ for $j = 1$ and $\sim 50 \text{ \AA}$ for $j = 2$ (see Figure 11 of Draine & Li 2007).

In Figure 3, we show the IR spectra in the 5–40 μm wavelength range emitted by the carbonaceous grain population for which the size distribution was constrained by Draine & Li (2007) using the functional form of Weingartner & Draine (2001a). The grains are illuminated by an MMP83-type ISRF but with the starlight intensity enhanced by a factor of $U = 1, 10^2, \dots, 10^6$. To explore the role of PAH size in contributing to the major PAH bands at 6.2, 7.7, 8.6, 11.3, and 12.7 μm , we consider three size ranges: (i) $3.5 \text{ \AA} < a < 20 \text{ \AA}$, (ii) $3.5 \text{ \AA} < a < 50 \text{ \AA}$, and (iii) $3.5 \text{ \AA} < a < 1 \mu\text{m}$.⁷ While the first two size ranges are mostly for PAHs, the third size range contains both PAHs and large graphitic grains.

Figure 3 demonstrates that the major PAH bands at 6.2, 7.7, 8.6, 11.3, and 12.7 μm are predominantly emitted by PAHs of $a < 20 \text{ \AA}$. For $1 \lesssim U \lesssim 10^6$, the emission spectra of PAHs of $a < 50 \text{ \AA}$ are not appreciably different from those of $a < 20 \text{ \AA}$. Also, for $1 \lesssim U \lesssim 10^4$, the emission spectra of the entire carbonaceous grain population of $3.5 \text{ \AA} < a < 1 \mu\text{m}$ are not appreciably different from those of PAHs of $a < 20 \text{ \AA}$. Only with $U \gtrsim 10^5$, the emission spectra of the entire carbonaceous grain population of $3.5 \text{ \AA} < a < 1 \mu\text{m}$ show considerable deviations from those of PAHs of $a < 20 \text{ \AA}$. This is because, exposed to an ISRF of $U \gtrsim 10^5$, grains of several tens of nanometers attain an equilibrium temperature high enough to emit in the MIR and raise the continuum at $\lambda > 5 \mu\text{m}$.

Figure 3 also shows that the emission spectra of PAHs at $\lambda < 15 \mu\text{m}$ of both $a < 20 \text{ \AA}$

⁶ Following Li & Draine (2001), the “radius” a of a PAH containing N_C C atoms is defined to be the radius of a sphere with the carbon density of graphite containing the same number of C atoms (i.e., $a \approx 1.286 N_C^{1/3} \text{ \AA}$).

⁷The lower size cutoff is set at $a = 3.5 \text{ \AA}$ (corresponding to $N_C = 20$), since PAHs smaller than $N_C = 20$ are not stable in the Galactic ISM (see Li & Draine 2001 and references therein).

and $a < 50 \text{ \AA}$, after being scaled by U , are essentially independent of U . This is expected from the single-photon heating nature of PAHs.⁸ This is also true for the entire carbonaceous grain population of $3.5 \text{ \AA} < a < 1 \mu\text{m}$, provided $U \lesssim 10^4$. For $U \gtrsim 10^5$, the PAH emission spectra at $\lambda < 15 \mu\text{m}$ differ appreciably from those of $U \lesssim 10^4$ due to the continuum emission from grains of several tens of nanometers, which are heated sufficiently to emit at $\lambda > 5 \mu\text{m}$.

Taking all these together, in the following for the PAH model template, we will adopt the PAH emission spectra calculated from PAHs of $a < 20 \text{ \AA}$ illuminated by $U = 1$. As discussed earlier, the PAH emission spectra at $\lambda < 15 \mu\text{m}$ (after being scaled by U) are essentially independent of U and are predominantly emitted by PAHs of $a < 20 \text{ \AA}$, the only exception being that, in regions with an extremely intense ISRF, the model spectra could have an unusually strong underlying continuum emitted by grains of several tens of nanometers. As will be demonstrated in §4, the selection of this particular PAH template is justified by the fact that it works very well for a wide range of environments.

We should note that the Draine & Li (2007) PAH model is actually for “astronomical” PAHs in the sense that, in modeling the observed PAH emission spectra, an empirical approach was taken to construct “astro-PAH” absorption properties that are consistent with both laboratory measurements and quantum-chemical computations (e.g., see Figure 2 of Draine & Li 2007) and spectroscopic observations of PAH emission in various astrophysical environments (Smith et al. 2007). Astro-PAHs do not represent any specific PAH molecules but approximate the actual absorption properties of the PAH mixture in astrophysical regions. Furthermore, neither laboratory-measured nor quantum-chemically computed spectra of individual PAH molecules accurately resemble the band positions and widths of observed PAH emission spectra. For example, the PAH bands of laboratory-measured spectra, which are commonly detected in absorption, are too narrow to be compatible with astronomical spectra, which are commonly seen in emission. On the other hand, the quantum-chemically computed spectra suffer from the fact that the band positions and strength are often not accurate and need to be scaled (Yang et al. 2017a, 2017b). Finally, the laboratory measurements are so far limited to PAHs smaller than ~ 50 C atoms (Hudgins & Allamandola 2005), while interstellar PAHs can be much larger (see Figure 7 of Draine & Li 2007). Li & Draine (2001) derived a mean PAH size of $N_C \approx 100$ in the diffuse ISM. Hence, it is desirable to synthesize a set of vibrational bands for “astro-PAHs” by adopting empirical PAH band

⁸Single-photon heating implies that the shape of the high- T end of the temperature (T) probability distribution function for a PAH molecule is the same for different levels of starlight intensity, and, therefore, the emission spectra (after being scaled by U) remain the same (see Li & Mann 2012). What really matters is the mean photon energy, which determines to what peak temperature a PAH molecule will reach upon absorption of such a photon.

positions, widths, and cross sections to mimic astronomical observations (e.g., Smith et al. 2007).

3.3. Algorithm and Error Estimation

We obtain the best fit for each galaxy using the IDL code `MPFIT`, a χ^2 -minimization routine based on the Levenberg-Marquardt algorithm (Markwardt 2009). The goodness-of-fit is measured by the reduced χ^2 ,

$$\chi_{\text{global}}^2/\text{dof} = \sum_{j=1}^{N_{\text{obs}}} \left\{ \frac{F_{\nu}(\text{mod}) - F_{\nu}(\text{obs})}{\sigma_{\nu}(\text{obs})} \right\}^2 / \{N_{\text{obs}} - N_{\text{mod}}\} \quad , \quad (2)$$

where $F_{\nu}(\text{mod})$ is the calculated model flux density, $F_{\nu}(\text{obs})$ is the observed flux density, $\sigma_{\nu}(\text{obs})$ is the observed 1σ uncertainty at each flux density point, N_{obs} is the number of data points, and N_{mod} is the total number of free parameters in the model.⁹

We estimate the uncertainties for the eight model parameters by performing Monte Carlo simulations. For the IRS spectrum of each source, we assume that each flux density point statistically follows a normal distribution. The dispersion is characterized by the observed 1σ error, which comprises statistical and systematic errors. The latter arises from the flux differences between the two nods of the IRS spectra, sky background contamination, and IRS pointing and flux calibration errors (Lebouteiller et al. 2011). A new random spectrum is generated, and then the same model is fit to derive the best-fit parameter set. We perform 500 simulations for each galaxy, and the final fitted spectrum is calculated with the median value of each parameter from their simulated distributions. The uncertainty is derived from the standard deviation of the distribution. Figure 4 illustrates our technique for Mrk 33.

⁹ The signal-to-noise ratio of an IRS spectrum in the $\sim 5\text{--}14.5\ \mu\text{m}$ interval is lower than that in the $\sim 14.5\text{--}38\ \mu\text{m}$ interval. This is caused by the different observation modules: the $5\text{--}14.5\ \mu\text{m}$ SL module has a slit width of $3''6$, and the $14.5\text{--}38\ \mu\text{m}$ LL module has a slit width of $11''2$. To better fit the $5\text{--}8\ \mu\text{m}$ continuum emission, PAHs, and the $9.7\ \mu\text{m}$ silicate feature, we arbitrarily increase the weights for the data points at $5\text{--}8\ \mu\text{m}$ by a factor of 4 and those at $8\text{--}14.5\ \mu\text{m}$ by a factor of 3 relative to those at $14.5\text{--}38\ \mu\text{m}$.

4. Applications

4.1. Galactic HLCs

To test our new technique, we first apply it to four Galactic HLCs, whose MIR dust spectrum is relatively pure and simple. HLCs, initially reported as FIR “cirrus” (Low et al. 1984), were discovered by the *Infrared Astronomical Satellite (IRAS)* at Galactic latitudes $|b| \gtrsim 25$ deg and 100 pc away from the Galactic center. They are mostly translucent clouds that are cospatial with atomic HI gas and molecular CO gas (Blitz et al. 1984; Magnani et al. 1985). As HLCs generally have very small optical extinctions ($A_V \lesssim 1$ mag; A. Mishra et al. 2018, in preparation), their MIR extinction, $\tau_{9.7\mu\text{m}} \approx A_V/18$ (Roche & Aitken 1984), is expected to be negligible. Thus, contamination by silicate absorption features (at ~ 10 and $18\mu\text{m}$) is minimal. Moreover, as HLCs reside far from the Galactic plane and contain little embedded ongoing star formation activity, there will be minimal emission from silicate dust heated by internal ionizing photons. Consequently, the overall $5\text{--}15\mu\text{m}$ emission of HLCs is expected to arise simply from PAH molecules and grains of different temperatures. The basic parameters of the HLCs analyzed in this paper are tabulated in Table 1.

The MIR spectra of the four HLCs display prominent PAH emission at 6.2 , 7.7 , 8.6 , 11.3 , and $12.7\mu\text{m}$ (Figure 5). Their complete IRS data also show strong molecular hydrogen lines of $\text{H}_2 S(2)$ 12.3 , $\text{H}_2 S(1)$ 17.0 , and $\text{H}_2 S(0)$ $28.2\mu\text{m}$. Since $\text{H}_2 S(2)$ 12.3 and $\text{H}_2 S(1)$ $17.0\mu\text{m}$ are blended with PAH features and their relative strength is significantly lower compared to adjacent PAH features, we retain these two lines in the fit, but we omit the strongest line, $\text{H}_2 S(0)$ $28.2\mu\text{m}$. It is apparent that the PAH template, in conjunction with three modified blackbodies, can fairly well describe the PAH emission and continuum emission of HLCs. The flux density ratio between the data and the fit (bottom of each subpanel) also indicates that the global difference is less than 10%. The largest discrepancy occurs around $17\mu\text{m}$, which coincides with $\text{H}_2 S(1)$. The model slightly overpredicts the emission between PAH 6.2 and $7.7\mu\text{m}$, and the wing of $8.6\mu\text{m}$ is underestimated.

We note that the dust temperature (and standard deviation¹⁰) required to produce the continuum emission in the four HLCs is 460 ± 59 , 102 ± 10 , and 45 ± 1 K on average for the hot, warm, and cold components, respectively. The temperature for the hot component is especially high for HLCs, which have a deficit of UV radiation. Additionally, it seems that the

¹⁰The uncertainties on the dust temperatures, particularly for the cold component, are generally very small and likely underestimated because of the small errors of the flux densities at $\lambda \gtrsim 20\mu\text{m}$. The true uncertainties are dominated by systematic effects such as the omission of FIR data and the choice of PAH template, which we discuss in Section 5.1.

temperature variation from cloud to cloud is rather small for the hot and warm components, despite the rather different spatial distributions of the HLCs. In the next section, we will show that this fact remains true in extragalactic H II regions.

The best-fit MIR extinction (Table 8) is negligible, consistent with the expectation from the low values of A_V toward HLCs. We place an upper limit on $\tau_{9.7}$ by iteratively adjusting its value while keeping the other model parameters fixed. The goodness-of-fit is judged by $\chi^2(\text{sil})$ defined over 9–11 μm to closely bracket the silicate absorption feature at 10 μm . We estimate an upper limit on $\tau_{9.7}$ when $\chi^2(\text{sil})$ changes by 1%.

4.2. Star-forming Galaxies

Proceeding to the next level of complexity, we apply our technique to nearby galaxies whose dominant or only known source of excitation is star formation. We utilize data from the Spitzer Infrared Nearby Galaxy Survey (SINGS; Kennicutt et al. 2003; Smith et al. 2007), which comprises 75 nearby galaxies with distances $\lesssim 30$ Mpc, including both star-forming (H II) nuclei, LINERs, and Seyfert galaxies. SINGS is designed to span a wide range of galaxy morphology, luminosity, star formation rate, and extinction. The sample has comprehensive multiwavelength data from X-rays to radio, allowing derivation of a variety of physical properties, including those of dust and gas. Among the 75 SINGS galaxies, we first choose the 24 classified as H II nuclei (Table 2). The best-fit results for two cases are illustrated in Figure 6; the fits for the rest are available in the electronic figure set.

Our five-component model can successfully recover the PAH and continuum emission. In some galaxies, there is a dip around 15 μm that the model fails to fit. Such a feature is prominent in NGC 337, 628, 925, 2403, 2976, 4254, 4625, and 7793. We note that this feature is absent from HLCs. The median temperature of the cold, warm, and hot dust components are 34 ± 8 , 70 ± 8 , and 386 ± 78 K, respectively. The hot dust component has a temperature distribution of ~ 300 – 400 K, similar to that of HLCs. This strikingly high dust temperature for extragalactic H II regions and Galactic HLCs cannot originate from dust in temperature equilibrium, as the IR SEDs of the SINGS star-forming galaxies and HLCs peak around 100 μm (Dale et al. 2012; A. Mishra et al. 2018, in preparation). Nor can the observed high temperatures be explained by an intense UV radiation field because HLCs have no embedded star formation and are located far from the Galactic disk (70 ± 15 pc). For H II regions, if such a high temperature is generated from hot dust heated by intense UV photons, we would expect to see silicate emission around 10 and 18 μm , which can be produced in an environment with high photon density and optically thin MIR conditions. Yet the H II nuclei show no emission or only mild silicate absorption. The fairly uniform

high temperatures detected in H II nuclei and HLCs indicate some common physical process at work. Y. Xie et al. (2018, in preparation) propose that this hot component is produced by nanometer-sized dust grains transiently heated by single-photon absorption.

Our best-fit results also yield estimates of the MIR extinction. The majority (19/24) of the H II nuclei have no detectable extinction, with upper limits of $\tau_{9.7} \lesssim 0.01$.

4.3. Low-luminosity AGNs

We continue with a subset of 22 nearby, well-studied, low-luminosity AGNs from SINGS with high-quality IRS spectra (Table 2). In these systems, the MIR light comes from a mixture of emission from the AGN torus and star-forming regions from the central kpc-scale region of the galaxy. All the sources display prominent PAH features. The best-fit results for two cases are illustrated in Figure 7; the fits for the rest are available in the electronic figure set.

The global MIR emission for the AGN sample is also well fit with a combination of a PAH template and three modified blackbodies. As in the H II nuclei, seven objects (NGC 3521, 3938, 4579, 4669, 4736, 5033 and 5055) show a prominent dip feature around $15 \mu\text{m}$ that is not well captured by the model. The entire PAH spectrum is generally very well recovered. A notable exception, also observed in HLCs and H II nuclei, is that the left wing of PAH $8.6 \mu\text{m}$ is slightly underestimated in 10 out of 22 objects. The signal-to-noise ratio of the IRS spectrum of NGC 2915 and NGC 4579 is very low for $\lambda \lesssim 14.5 \mu\text{m}$, and their PAH $6.2 \mu\text{m}$ and $8.6 \mu\text{m}$ measurements are reported as nondetections.

As for the continuum, the median temperatures of the cold ($45 \pm 8 \text{ K}$) and hot ($391 \pm 266 \text{ K}$) dust components are comparable to those of H II nuclei, while the temperature of the warm component ($101 \pm 56 \text{ K}$) is more elevated and has a larger dispersion.

4.4. High-luminosity AGNs

The SINGS sample contains only relatively low-luminosity AGNs. It is known that PAH emission is present in some high-luminosity quasars (e.g., Shi et al. 2014; Xie et al. 2017), wherein the radiation from the AGN dominates the UV and optical emission of the entire host galaxy and a hot dusty torus complicates the MIR band. We apply our technique to a few representative Palomar-Green (PG; Schmidt & Green 1983) quasars. To demonstrate the potential of our decomposition method, we select as examples three PG quasars that have distinctive MIR characteristics (Table 3). We show that our methodology can be extended

to more complicated galaxy systems that contain bright AGNs. Both PAH features and the overall continuum are well reproduced in the fits, and upper limits on the PAH strength can be placed for systems with undetected PAH emission.

4.4.1. *PG 1351+236*

The MIR spectrum of PG 1351+236 is characterized by moderately strong PAH emission features at 6.2, 7.7, 8.6, and 11.3 μm sitting on top of a flat continuum (Figure 8 (a)). There are also several ionic lines of high ionization potential, including [S IV] 10.5 μm , [Ne V] 14.3 μm , [Ne V] 24.3 μm , and [O IV] 25.89 μm . Our generic five-component model well captures the PAH spectrum, while successfully depicting the MIR continuum emission. The derived temperatures are 375 ± 3 , 141 ± 1 , and 59 ± 1 K for the hot, warm, and cold components, respectively. The extinction toward this source is consistent with zero.

4.4.2. *PG 1244+026*

By contrast, PG 1244+026 exhibits only a flat, featureless continuum with no detectable PAH or ionic line emission. The best-fit result of this galaxy is show in Figure 8 (b). The fit of the overall continuum is fairly well reproduced by the superposition of three continuum components with temperatures 394 ± 5 K, 165 ± 1 K, and 77 ± 1 K. We place an upper limit on the strength of the PAH component, which accounts for only 1.3% of the total MIR luminosity.

4.4.3. *PG 1617+175*

PG 1617+175 represents another example of a quasar with little to no PAH or ionic line emission, but in this case, the continuum is not featureless (Figure 8 (c)). Two prominent emission features from amorphous silicate dust appear at 10 and 18 μm . Apart from the standard three blackbodies for the continuum, we add an additional warm silicate component, which is assumed to be optically thin in the MIR. Equation 2 is supplemented with an extra component, $\kappa_\nu B_\nu(T)$, where κ_ν represents the mass absorption coefficient of silicate dust as a function of frequency,¹¹ and $B_\nu(T)$ is the Planck function for silicate emission of temperature

¹¹The function κ_ν depends on the grain size and chemical composition of a specific dust. Here we adopt parameters for silicate dust that can represent the majority of PG quasars, with grain size $a = 1.5 \mu\text{m}$ and

T. This relatively simple model can successfully describe the MIR emission of PG 1617+175: the dust temperatures for the hot, warm, and cold blackbodies are 464 ± 5 , 144 ± 1 , and 62 ± 1 K, respectively, and the silicate emission component has a temperature of 410 ± 17 K. The PAH emission contributes less than 1% of the total MIR power.

A cautionary note: the silicate profile of AGNs that exhibit strong MIR m silicate emission can vary significantly from source to source. The silicate dust parameters that we adopt for PG 1617+175 may not be applicable to other sources.

4.5. Heavily Obscured Galaxies

Thus far, we have applied our technique to galaxies that suffer from little or no MIR extinction (§4.1–§4.3) or that are optically thin (§4.4). However, the nuclear regions of some galaxies, especially merging systems such as ULIRGs, are heavily dust-obscured. The MIR emission of these galaxies is strongly extinguished, and observationally it shows deep silicate absorption at 10 and $18 \mu\text{m}$ (e.g., Spoon et al. 2006), which substantially further complicates the decomposition of the PAHs. This phenomenon is also expected to be common in the high-redshift universe, where galaxies are generically more gas- (and hence dust-) rich. In this section, we extend our technique to more complex galaxy systems whose central source (AGN or nuclear starburst) is extremely enshrouded by dust and gas. We use as illustration two sources, one with PAH detected and another without (Table 3).

4.5.1. *Arp 220*

The optically heavily obscured late-stage merger Arp 220 is the nearest (78 Mpc) ULIRG. Its radio morphology suggests that the galaxy comprises two nuclei separated by 370 pc (Norris 1988; Barcos-Muñoz et al. 2015). While the presence of X-ray emission and radio variability reveals the presence of a weak AGN (Iwasawa et al. 2001; Batejat et al. 2012), most of the IR luminosity in Arp 220 is powered by a nuclear starburst (Armus et al. 2007).

The MIR spectrum of Arp 220 is characterized by deep silicate absorption troughs around 9.7 and $18 \mu\text{m}$, but PAH emission at 6.2, 7.7, and $11.3 \mu\text{m}$ can be clearly seen. Our fitting scheme successfully accommodates both (Figure 9 (a)). The temperatures of the three continuum components are 1500, 192 ± 1 , and 82 ± 0.1 K. The temperature reached

“astronomical silicate” (Draine & Lee 1984). The mass absorption coefficient is calculated from Mie theory; see Xie et al. (2017) and references therein for more details.

by the hot component (1500 K) is the maximum value allowed and corresponds to the sublimation limit of graphite dust. The higher temperature detected here presumably reflects significant heating from the embedded AGN.

Interestingly, the observed silicate absorption profile in Arp 220 differs from the silicate profile of the Galactic extinction curve of Wang et al. (2015), which peaks at a shorter wavelength ($\sim 9.5 \mu\text{m}$) and has a broader width. The extinction curve of Wang et al. (2015) is constrained via modeling observed Galactic extinctions from optical to MIR toward multiple lines of sight with theoretical “astronomical silicate” and graphite dust from Draine & Lee (1984). The “astronomical silicate” profile was calibrated using the observed $9.7 \mu\text{m}$ silicate emission profile from the inner region of the Orion H II (Trapezium) region, which is found to be very similar to absorption features in dense molecular clouds in terms of having a shorter wavelength peak and broader width (Gillett et al. 1975). The poor match between the $9.7 \mu\text{m}$ silicate absorption profile of Arp 220 and that of Wang et al.’s extinction curve might be caused by variations in ISM properties in different environments. We therefore adopt the extinction curve derived from the diffuse ISM, whose $9.7 \mu\text{m}$ silicate feature generally has a longer peak wavelength and narrower width, considering extinction curves based on observations in the solar circle (Chiar & Tielens 2006) and toward the Galactic center (Smith et al. 2007)¹². We find that both extinction curves can match the silicate absorption profile equally well at 9.7 and $18 \mu\text{m}$ for Arp 220; Figure 9 (a) illustrates the best-fit result obtained using the curve of Chiar & Tielens (2006). Chiar & Tielens (2006) found that the silicate profile and relative feature strength ($9.7/18$) of the local ISM extinction curve can be better explained using porous pyroxene silicate combined with a small fraction of amorphous olivine, while for the diffuse ISM in the Galactic center an amorphous olivine mass fraction of more than 80% is required to explain the silicate profile at $9.7 \mu\text{m}$ (Kemper et al. 2004). Nevertheless, the silicate absorption profiles in Arp 220 definitely share closer characteristics with the diffuse ISM.

¹²The extinction curve of Smith et al. (2007) is composed of a power law and silicate extinction peaking at 9.7 and $18 \mu\text{m}$. The silicate component consists of the observed absorption profile that covers $8\text{--}13 \mu\text{m}$ (Kemper et al. 2004) and a Drude profile with a peak at $18 \mu\text{m}$ and a FWHM of $4.45 \mu\text{m}$ to form the extinction above $13 \mu\text{m}$. The curve is extended to $\lambda < 8 \mu\text{m}$ by assuming $\tau_\lambda = \tau_8 \times \exp[2.03(\lambda - 8)]$, with τ_8 being the observed silicate absorption at $8 \mu\text{m}$. A power law with an index of 1.7 is adopted to represent the carbon dust extinction and is joined to the silicate profile to form the complete extinction curve. See Smith et al. (2007) for more details.

4.5.2. IRAS F08572+3915

IRAS F08572+3915 is another late-stage merger ULIRG, one that possesses double nuclei detected in the X-rays (Iwasawa et al. 2011). Optical emission-line ratios indicate the presence of an obscured AGN in the northwestern core (Yuan et al. 2010). There is no PAH emission detected in the MIR, and the whole spectrum is dominated entirely by two deep absorption troughs at 10 and 18 μm , which arise from amorphous silicate dust. Besides amorphous silicate, IRAS F08572+3915 also shows unambiguous crystalline silicate absorption at 11, 16, and 18 μm (Spoon et al. 2006).

Figure 9 (b) shows that our technique can recover the observed silicate absorption features, together with the continuum emission, reasonably well. The dust continuum is characterized by temperatures of 690 ± 90 , 250 ± 42 , and 69 ± 12 K for the hot, warm, and cold components, respectively. The PAH component contributes $< 1\%$ to the total MIR luminosity, and we are able to only place an upper limit on the PAH strength for this galaxy. We note, in passing, that the popular PAHFIT code performs especially poorly for galaxies such as IRAS F08572+3915 that have a highly complex continuum. In this particular example, the PAH flux derived from PAHFIT is significantly overestimated.

Similar to Arp 220, IRAS F08572+3915 shows a redder peak and broader width for the 9.7 μm silicate absorption profile with respect to the extinction curve of Wang et al. (2015), but its 18 μm absorption profile appears normal. The extinction curve of Chiar & Tielens (2006) can fit the observed 9.7 μm silicate profile but not that at 18 μm , which shows a bluer peak in the observations. The best overall fit is achieved by the extinction curve of Smith et al. (2007), which is based on observations of the diffuse ISM toward the Galactic center.

5. Discussion

We demonstrated that a simple technique comprising a theoretical PAH template, three modified blackbodies, and an extinction term can successfully decompose the PAH spectrum and the main dust components. We apply this technique to a variety of systems, from the simplest HLCs to galaxies with increasingly complex properties. We successfully recover the strength of the PAH emission (or upper limits thereof), characteristic temperatures of the dust continuum, and the level of dust extinction. Below, we discuss the robustness of our technique (§5.1), and we perform a detailed comparison between the PAH strengths measured by our technique with those derived from other methods (§5.2).

5.1. Robustness Demonstration

5.1.1. The Effect of the FIR

Our methodology fits the MIR spectrum with a simple model comprising a PAH template and three modified blackbodies to represent the continuum. We do not consider longer-wavelength data in the FIR, and it is legitimate to wonder to what extent our results might be affected by this choice. Here we test this effect by explicitly fitting two objects with and without including FIR data from *Herschel*, which allows us to extend the SED out to 500 μm .

Prior to combining the IRS spectra with the *Herschel* photometry, we need to consider a possible aperture mismatch between the two data sets. The slit width of the SL module ($\sim 5.1\text{--}14.5 \mu\text{m}$) is $3''.6$, and for the LL module ($\sim 14.5\text{--}38 \mu\text{m}$) it is $10''.5$, whereas the coarsest point-spread function of SPIRE on *Herschel* has $\text{FWHM} = 36''.6$ at 500 μm . In this paper, the flux density of the SL module is scaled to that of the LL module to compensate for possible flux loss due to the aperture difference. We use *IRAS* 25 μm images to verify that the vastly different resolutions between the MIR and FIR sample the same physical scale. We require that the galaxies included in our analysis are fully enclosed within the LL slit width.

We choose the ULIRG IRAS F01364–1042 at $z = 0.048$ and the quasar PG 1351+236 at $z = 0.055$ for our tests (Table 3). The FIR photometry, obtained using *Herschel*/PACS for 70, 100, and 160 μm and *Herschel*/SPIRE for 250, 350, and 500 μm , are given in Chu et al. (2017) and Shangguan et al. (2018). A single modified blackbody with $\beta = 2$ is adopted to account for the FIR SED. The SEDs and their best fits are shown in Figure 10 for IRAS F01364–1042 and in Figure 11 for PG 1351+236. In each figure, the top panel (a) shows the SED from ~ 5 to 40 μm , while the bottom panel (b) shows the full IR SED from ~ 5 to 500 μm . We see that a single, additional modified blackbody of temperature $T^f \approx 25 - 30$ K can well describe the FIR portion of the SED. Nevertheless, this extra cold dust component has little noticeable effect on the temperature of the hot, warm, and cold dust components. The derived extinction and the scale factor for the PAH template are also essentially unchanged. This test verifies that our standard fitting technique, which is based exclusively on the IRS spectrum, not only gives robust measurements of PAH but also places reasonable constraints on the overall dust continuum emission in the MIR.

5.1.2. *The Effects of Photon Density and PAH Parameters on the PAH Theoretical Template*

All of the fits thus far are based on a theoretical PAH template calculated assuming a photon density of $U = 1$. In Section 3.2, we showed that, for grain sizes $a \lesssim 20 \text{ \AA}$ or $a \lesssim 50 \text{ \AA}$, the PAH spectrum for $\lambda \lesssim 15 \text{ \mu m}$ is quite uniform for a wide range of photon densities from $U = 1$ to 10^6 (Figure 2). Beyond 15 \mu m , the emission mainly originates from the continuum associated with PAHs. The power drops in high- U environments because for $U \gtrsim 10^4$ the timescale for photon absorption becomes less than the cooling timescale for some grains due to the high photon density. These grains will not cool completely and hence gradually will attain a temperature close to the equilibrium temperature. Nevertheless, the deviation of the PAH spectrum beyond 15 \mu m will not seriously affect the recovery of the observed PAH emission. This is demonstrated in Figure 12, where we fit NGC 1482 using theoretical templates of different U at $a \lesssim 20 \text{ \AA}$. The uppermost panel shows the standard, default fit with $U = 1$, and the subsequent panels display the best-fit ratio between higher values of U and $U = 1$. It can be seen that the scale factor for the PAH template varies by less than 20% across six orders of magnitude in U . As for the derived dust temperatures and extinction, they remain practically constant up till $U = 10^4$; for $U \gtrsim 10^5$, the temperature and extinction vary markedly because of changes in the template spectra longer than 15 \mu m under conditions of extremely high photon density. We therefore suggest that, under most conditions, the $U = 1$ template is sufficient to measure accurate PAH strengths.

In the case of grains with a full size distribution, PAHs dominate the spectrum at wavelengths $\lesssim 15 \text{ \mu m}$ for $U \lesssim 10^3$. When U increases to sufficiently large values (e.g., $\gtrsim 10^4$), some large grains ($a \gtrsim 50 \text{ \AA}$) will gain high temperatures and peak at short wavelengths, causing changes of spectral shape, and the MIR emission will no longer be purely emitted from PAHs. Repeating our analysis for all galaxies using the PAH template for $U = 10^4$ and grains with a full size distribution, we find that the fits are considerably worse. PAH emission is generally underestimated, and the 10 \mu m silicate feature is not well reproduced.

Besides photon density U , the characteristics of the theoretical PAH template are determined by the combined effects of chemical composition, grain size distribution, gas temperature, electron density, and mass fraction locked in ultra-small grains. The physical parameters for the theoretical PAH spectra used in the current paper are constrained by observations of the Milky Way and the Magellanic Clouds. Although, in principle, these parameters should vary in different galaxies, currently we have very limited information on them for external galaxies because of the difficulty in determining the extinction curve and chemical depletion in distant galaxies. In spite of these complications, our study highlights the interesting fact that the PAH spectrum is surprisingly homogeneous across an extraor-

dinarily wide range of galactic environments (§ 5.1.3).

5.1.3. *The Uniformity of the PAH Spectrum and the Peculiar Emission Spectra in Elliptical Galaxies*

For each object with clear PAH detection, we derive two PAH spectra, one from the best-fit theoretical PAH template and the other directly from the residuals between the observed total spectrum and best-fitting continuum model (after removal of isolated ionic emission lines). The two versions of the PAH spectra are compared directly in Figure 13 for HLCs, in Figure 14 for H II nuclei, and in Figure 15 for AGNs. It is remarkable that a *single* theoretical PAH template can successfully match the observed PAH spectrum over such a diverse range of astrophysical environments. This implies that, to first order, the PAH spectrum is essentially invariant, demonstrating that, although the PAH spectral shape (and, as a result, the PAH band ratio) does show some variations among different systems, it remains fairly constant in a wide variety of environments. The most notable exception is for the feature at $8.6\ \mu\text{m}$, for which the model generally underestimates the PAH flux by $\sim 30\%$. In several AGNs, the PAH $7.7\ \mu\text{m}$ band is overpredicted in the best-fit model, while the PAH $11.3\ \mu\text{m}$ band is underestimated. This phenomenon is quite obvious in NGC 3627, 4569, 4736, 5195, 7331 and PG 1351+236. For the sample of AGNs investigated here, the mean and standard deviation of the ratio of the $7.7\ \mu\text{m}$ band to the $11.3\ \mu\text{m}$ band is 3.11 ± 0.03 from the best-fit template and 3.02 ± 0.80 from the observed spectrum. By contrast, for the six AGNs having an apparent deficit in the $7.7\ \mu\text{m}$ band, $7.7\ \mu\text{m}/11.3\ \mu\text{m} = 2.40 \pm 0.35$, which is consistent with the ratio of 2.15 ± 0.52 derived from PAHFIT (§ 5.2).

We note that appreciable variations in the PAH spectral profiles have been detected, often in extreme environments (e.g., Diamond-Stanic & Rieke 2010, Sales et al. 2010). In some elliptical galaxies, the PAH $7.7\ \mu\text{m}$ band is significantly suppressed relative to the PAH $11.3\ \mu\text{m}$ band (e.g., see Kaneda et al. 2005, 2008; Rampazzo et al. 2013). This is also true in the centers of active galaxies (e.g., see Smith et al. 2007). We have also applied our technique to NGC 2974 and NGC 5018, two elliptical galaxies exhibiting unusual PAH spectra (Kaneda et al. 2008). As shown in Figure 16, the current technique can reasonably well characterize the overall continuum emission underlying the PAH features. However, the PAH emission features are not closely reproduced by the PAH template spectrum: both galaxies show a strong enhancement at the PAH $11.3\ \mu\text{m}$ band in comparison with the template. Our technique also fails to reproduce the dip around $15\ \mu\text{m}$. This is not unexpected, since the theoretical template has a fixed PAH spectral shape. The peculiar $11.3/7.7$ band ratios seen in these elliptical galaxies indicate that the PAH sizes may be affected in the hot plasmas

of ellipticals; smaller PAHs may be preferentially destroyed while larger ones survive in the hostile environment. As a matter of fact, these sources will serve as a backbone to remove the contamination of old stars to star formation rates estimated from PAH emission (Y. Xie et al. 2018, in preparation).

We note that, with a fixed PAH spectral shape, the current technique by itself does not automatically yield PAH band ratios for sources whose PAH spectra differ considerably from the theoretical template. Nevertheless, variations of the PAH band ratios among different astronomical environments can be investigated from the residual spectrum once the underlying MIR continuum and extinction are self-consistently described and subtracted (see, e.g., Figures 13–15). The total luminosity of PAHs can be determined straightforwardly. Our technique also allows us to place upper limits on the strength of PAH emission in galaxies that are highly obscured and/or hosting luminous AGNs, for which PAH features are often difficult to detect.

5.2. Comparison with Other Techniques

We compare the fluxes of the individual PAH features at 6.2, 7.7, 8.6, and 11.3 μm measured with our technique (Table 4) with those obtained from PAHFIT (Table 5; Figure 17), spline fit (Table 6; Figure 18), and CAFE (Table 7; Figure 19)¹³. We duplicated the PAH template of CAFE based on the parameters tabulated in Table 1 of Marshall et al. (2007). The fluxes for individual PAH bands were derived directly from the observed spectra by fitting them with Drude profiles with FWHM parameters taken from Draine & Li (2007), after subtraction of the best-fit continuum model, while the total PAH flux was derived from integrating the observed, continuum-subtracted PAH spectra from 5 to 20 μm where PAH emission dominates the radiation. In general, our new technique yields roughly the same level of PAH strength as PAHFIT for the individual bands at 6.2, 7.7, 8.6, and 11.3 μm , suggesting that the two methods derive a similar level of continuum emission. By contrast, spline fit systematically and significantly underestimates the PAH strength by factors of ~ 1.5 –2 for the 6.2 and 11.3 μm features and by as much as factors of ~ 4 –6 for the 7.7 and 8.6 μm features. The large discrepancy arises from the fact that spline fit does not properly account for the flux in the wings of the lines. As for the comparison with CAFE,

¹³ A number of studies (e.g., Rieke et al. 2009; da Cunha et al. 2010; Wu et al. 2010; Brown et al. 2014) have used starburst templates to explore the multiwavelength SEDs of galaxies. However, most of these templates were derived directly from observed spectra, which contain both dust continuum and line emission and therefore do not directly yield fluxes for the PAH features. Here we limit our discussion to the three methods (PAHFIT, spline fit, and CAFE) that are closest in methodology to ours.

the PAH fluxes of the 6.2, 8.6, and 11.3 μm bands are consistent with ours within $\sim 10\%$, but those of the 7.7 μm band are $\sim 20\%$ lower. As shown in Figure 20, the PAH template used in CAFE matches our template fairly well at main PAH features at 6.2, 7.7, 8.6 and 11.3 μm , except for the deep drop at $\sim 10 \mu\text{m}$. At $\lambda > 20 \mu\text{m}$, the CAFE template declines precipitously relative to our theoretical template. Both discrepancies can be accounted for with the continuum emission associated with the PAH molecules (see Li & Draine 2001).

Figure 21 examines the total flux from all PAH bands as measured using PAHFIT and CAFE. Our technique recovers $\sim 30\%$ more total PAH flux than either of these two methods; the difference varies from $\sim 20\%$ to $\sim 40\%$ as the integration interval changes from 5–15 to 5–30 μm . This primarily reflects our treatment of the long-wavelength continuum emission of PAHs. To account for the laboratory-measured long-wavelength skeletal vibrations of PAHs (e.g., see Moutou et al. 1996), Draine & Li (2007) incorporated a “continuum” opacity from $\sim 13 \mu\text{m}$ longward, represented by a Drude profile peaking at 15 μm with an FWHM of 12 μm (see Table 1 in Draine & Li 2007). This is clearly demonstrated in Figure 22, where we compare the “residual” PAH spectra of the star-forming galaxy Mrk 33, obtained by subtracting (from the observed *Spitzer*/IRS spectrum) the best-fit continuum derived, respectively, from our technique, PAHFIT, and CAFE. It is apparent that the “residual” PAH spectra at $\lambda \lesssim 13 \mu\text{m}$ are essentially the same for all three methods. This explains why the fluxes for individual PAH bands derived from all three methods agree with each other fairly well. However, the PAH continuum emission at $\lambda \gtrsim 13 \mu\text{m}$ from our method considerably exceeds that of PAHFIT and CAFE. With the PAH continuum emission included, our technique requires a smaller amount of thermal continuum emission and thus a larger amount of PAH emission. The extinction, as discussed below, only plays a minor role, since most of our sample galaxies are only mildly extinguished.

We suggest that the total PAH flux (both features and continuum) emitted in the ~ 5 – $20 \mu\text{m}$ wavelength range is a better star formation rate indicator compared to the flux of an individual PAH feature (e.g., the 7.7 μm feature), since the latter is sensitive to PAHs of a particular size and a particular charging status (e.g., neutral or ionized). Also, physically speaking, the PAH continuum is excited by stellar photons in the same way as the PAH features. The absorption of stellar UV photons is balanced by the emission of both PAH features and PAH continuum. Therefore, a proper counting of the absorbed UV starlight (and thus the star formation rate) should also include the PAH continuum emission. For a given source, the template method proposed here determines the dust continuum emission and therefore readily allows us to derive the total PAH flux (both PAH features and PAH continuum) by simply integrating the “residual” spectrum (e.g., continuum-subtracted observational spectrum) over ~ 5 – $20 \mu\text{m}$. To allow for a fair comparison with other techniques (e.g., PAHFIT), a scaling factor of ~ 1.3 is needed because our template technique recovers

$\sim 30\%$ more total PAH flux than PAHFIT.

Lastly, we compare the extinction derived from our technique with that from PAHFIT (Table 8; Figure 23a). For SINGS galaxies that have significant silicate absorption ($\tau_{9.7} \gtrsim 0.2$; e.g., NGC 1266, 1482, 3198, and 6946), the two techniques obtain comparable results. On the other hand, for galaxies for which PAHFIT derives small ($\tau_{9.7} \lesssim 0.2$) but nonzero extinction, our technique obtains systematically lower values, most of them are upper limits (e.g., the average extinction for HLCs from PAHFIT is ~ 0.2 , whereas our technique only derives an upper limit for all of them). Similar trends appear when our extinctions are compared to those derived using the CAFE template (Figure 23b). This is consistent with the optical analysis of the SINGS galaxies by Dale et al. (2006), who derived $A_V \approx 1$ mag. A. Mishra et al. (2018, in preparation) also report a small optical extinction for HLCs, with $A_V \lesssim 1$ mag. Assuming $A_V/\tau_{9.7} = 18$ for the diffuse ISM (Roche & Aitken 1984), SINGS galaxies and HLCs have a typical MIR extinction of $\langle \tau_{9.7} \rangle \approx 0.05$.

6. Summary

We present a new technique to decompose PAH emission from MIR spectra by making use of a theoretical PAH template in conjunction with three continuum emission components and an extinction term. Our future goals are to understand the physical processes responsible for the production of the pervasive PAH spectrum and to use the PAH strength as a quantitative measure of the star formation rate in different extragalactic environments. The main results of this paper are as follows.

- We can robustly extract the PAH spectrum in a wide range of galactic environments, from the simplest Galactic HLCs to nearby star-forming galaxies, low-luminosity active galaxies, luminous quasars, and highly obscured IR-luminous galaxies. When PAH is undetected, an upper limit can be placed on its strength.
- We can simultaneously describe the associated continuum reasonably well and derive the MIR extinction. Galaxies that have strong emission or absorption features at 9.7 and $18 \mu\text{m}$ appear to have diverse silicate dust properties (grain size and chemical composition) and extinction curves.
- To achieve a robust decomposition of the PAH spectrum from the MIR SED, FIR observations are not needed.
- The PAH spectrum is surprisingly invariant with galactic environment, suggesting a uniform set of conditions responsible for its excitation.

- The PAH fluxes of individual bands derived from the current method are consistent with those obtained using PAHFIT and CAFE, whereas the total PAH fluxes derived from our method are as much as $\sim 30\%$ higher. The primary cause for the difference in total PAH flux is the long-wavelength continuum emission of PAHs associated with their skeletal vibrations, which is incorporated in the theoretical PAH template used in our work. A scaling factor of ~ 1.3 is needed when one compares the total PAH flux derived from our template method with that from PAHFIT. The PAH fluxes obtained from the spline fit method are lower than ours because it underestimates the wings of the PAH features.

- This technique is motivated to decompose PAH emission and derive upper limits in complicated systems, which will set a uniform baseline for calibrating PAH emission to star formation rate. In parallel, PAHFIT, CAFE, and other techniques have their own advantages in dealing with different systems by allowing the band ratios to change inherently.

We thank the referee, J. D. Smith, for stimulating comments and suggestions that helped to improve the quality and presentation of our paper, as well as for his careful explanation of the IRS spectra of SINGS galaxies. H. Kaneda kindly shared the IRS spectra of NGC 2974 and NGC 5018, and J. Ingalls sent us the IRS spectra of the four Galactic high-latitude clouds. B. T. Draine and L. H. Jiang provided helpful discussions and suggestions. This work was supported by the National Key R&D Program of China (2016YFA0400702) and the National Science Foundation of China (11473002, 11721303). Y. X. is supported by China Postdoctoral Science Foundation Grant 2016 M591007. The Cornell Atlas of *Spitzer*/IRS Sources (CASSIS) is a product of the Infrared Science Center at Cornell University, supported by NASA and JPL.

REFERENCES

- Acke, B., Bouwman, J., Juhász, A., et al. 2010, *ApJ*, 718, 558
- Allamandola, L. J., Tielens, A. G. G. M., & Barker, J. R. 1985, *ApJ*, 290, L25
- Allamandola, L. J., Hudgins, D. M., & Sandford, S. A. 1999, *ApJ*, 511, L115
- Alonso-Herrero, A., Poulton, R., Roche, P. F., et al. 2016, *MNRAS*, 463, 2405
- Alonso-Herrero, A., Ramos Almeida, C., Esquej, P., et al. 2014, *MNRAS*, 443, 2766
- Andrews, H., Boersma, C., Werner, M. W., et al. 2015, *ApJ*, 807, 99
- Armus, L., Charmandaris, V., Bernard-Salas, J., et al. 2007, *ApJ*, 656, 148
- Bakes, E. L. O., & Tielens, A. G. G. M. 1994, *ApJ*, 427, 822
- Barcos-Muñoz, L., Leroy, A. K., Evans, A. S., et al. 2015, *ApJ*, 799, 10
- Batejat, F., Conway, J. E., Rushton, A., et al. 2012, *A&A*, 542, L24
- Bauschlicher, C. W., Jr., Boersma, C., Ricca, A., et al. 2010, *ApJS*, 189, 341-351
- Blitz, L., Magnani, L., & Mundy, L. 1984, *NASA Conference Publication*, 2345, 231
- Boersma, C., Bregman, J. D., & Allamandola, L. J. 2013, *ApJ*, 769, 117
- Boersma, C., Bregman, J., & Allamandola, L. J. 2014, *ApJ*, 795, 110
- Brandl, B. R., Bernard-Salas, J., Spoon, H. W. W., et al. 2006, *ApJ*, 653, 1129
- Brown, M. J. I., Moustakas, J., Smith, J.-D. T., et al. 2014, *ApJS*, 212, 18
- Cami, J. 2011, *EAS Publications Series*, 46, 117
- Chiar, J. E., & Tielens, A. G. G. M. 2006, *ApJ*, 637, 774
- Chu, J. K., Sanders, D. B., Larson, K. L., et al. 2017, *ApJS*, 229, 25
- da Cunha, E., Charmandaris, V., D´iaz-Santos, T., et al. 2010, *A&A*, 523, A78
- Dale, D. A., Aniano, G., Engelbracht, C. W., et al. 2012, *ApJ*, 745, 95
- Dale, D. A., Smith, J. D. T., Armus, L., et al. 2006, *ApJ*, 646, 161
- Diamond-Stanic, A. M., & Rieke, G. H. 2010, *ApJ*, 724, 140

- Draine, B. T. 2003, *ARA&A*, 41, 241
- Draine, B. T., & Lee, H. M. 1984, *ApJ*, 285, 89
- Draine, B. T., & Li, A. 2007, *ApJ*, 657, 810
- Draine, B. T., & Li, A. 2001, *ApJ*, 551, 807
- Geers, V. C., Augereau, J.-C., Pontoppidan, K. M., et al. 2006, *A&A*, 459, 545
- Gillett, F. C., Forrest, W. J., Merrill, K. M., Soifer, B. T., & Capps, R. W. 1975, *ApJ*, 200, 609
- Genzel, R., Lutz, D., Sturm, E., et al. 1998, *ApJ*, 498, 579
- Hao, L., Wu, Y., Charmandaris, V., et al. 2009, *ApJ*, 704, 1159
- Heckman, T. M. 1980, *A&A*, 87, 152
- Hony, S., Van Kerckhoven, C., Peeters, E., et al. 2001, *A&A*, 370, 1030
- Houck, J. R., Roellig, T. L., Van Cleve, J., et al. 2004, *Proc. SPIE*, 5487, 62
- Huang, J.-S., Faber, S. M., Daddi, E., et al. 2009, *ApJ*, 700, 183
- Hudgins, D. M., & Allamandola, L. J. 2004, in *ASP Conf. Ser. 309, Astrophysics of Dust*, ed. A.N. Witt, G.C. Clayton, & B.T. Draine (San Francisco, CA: ASP), 665
- Hudgins, D. M., & Allamandola, L. J. 2005, in *IAU Symp. 231, Astrochemistry: Recent Successes and Current Challenges*, ed D.C. Lis, G.A. Blake, & E. Herbst (Cambridge: Cambridge Univ. Press), 443
- Ingalls, J. G., Bania, T. M., Boulanger, F., et al. 2011, *ApJ*, 743, 174
- Iwasawa, K., Sanders, D. B., Teng, S. H., et al. 2011, *A&A*, 529, A106
- Iwasawa, K., Matt, G., Guainazzi, M., & Fabian, A. C. 2001, *MNRAS*, 326, 894
- Kaneda, H., Onaka, T., & Sakon, I. 2005, *ApJ*, 632, L83
- Kaneda, H., Onaka, T., Sakon, I., et al. 2008, *ApJ*, 684, 270
- Kemper, F., Vriend, W. J., & Tielens, A. G. G. M. 2004, *ApJ*, 609, 826
- Kennicutt Jr., R. C., Armus, L., Bendo, G., et al. 2003, *PASP*, 115, 928

- Kennicutt Jr., R. C., & Evans, N. J. 2012, *ARA&A*, 50, 531
- Léger, A., & Puget, J. L. 1984, *A&A*, 137, L5
- Lebouteiller, V., Barry, D. J., Spoon, H. W. W., et al. 2011, *ApJS*, 196, 8
- Li, A. 2004, in *ASP Conf. Ser. 309, Astrophysics of Dust*, ed. A.N. Witt, G.C. Clayton, & B.T. Draine (San Francisco, CA: ASP), 417
- Li, A. 2009, in *Small Bodies in Planetary Sciences (Lecture Notes in Physics Vol. 758)*, ed. I. Mann, A. Nakamura, & T. Mukai (Springer), 167
- Li, A., & Draine, B. T. 2001, *ApJ*, 554, 778
- Li, A., & Mann, I. 2012, in *Astrophys. Space Sci. Library, Vol. 385, Nanodust in the Solar System: Discoveries and Interpretations* (Berlin: Springer-Verlag), 5
- Low, F. J., Young, E., Beintema, D. A., et al. 1984, *ApJ*, 278, L19
- Lutz, D., Spoon, H. W. W., Rigopoulou, D., Moorwood, A. F. M., & Genzel, R. 1998, *ApJ*, 505, L103
- Magdis, G. E., Elbaz, D., Dickinson, M., et al. 2011, *A&A*, 534, A15
- Magnani, L., Blitz, L., & Mundy, L. 1985, *ApJ*, 295, 402
- Markwardt, C. B. 2009, *Astronomical Data Analysis Software and Systems XVIII*, 411, 251
- Marshall, J. A., Herter, T. L., Armus, L., et al. 2007, *ApJ*, 670, 129
- Mathis, J. S., Mezger, P. G., & Panagia, N. 1983, *A&A*, 128, 212
- Moutou, C., Léger, A., & D'Hendecourt, L. 1996, *A&A*, 310, 297
- Norris, R. P. 1988, *MNRAS*, 230, 345
- Onaka, T., Yamamura, I., Tanabe, T., Roellig, T. L., & Yuen, L. 1996, *PASJ*, 48, L59
- Peeters, E., Spoon, H. W. W., & Tielens, A. G. G. M. 2004, *ApJ*, 613, 986
- Rampazzo, R., Panuzzo, P., Vega, O., et al. 2013, *MNRAS*, 432, 374
- Rieke, G. H., Alonso-Herrero, A., Weiner, B. J., et al. 2009, *ApJ*, 692, 556
- Roche, P. F., & Aitken, D. K. 1984, *MNRAS*, 208, 481

- Rosenberg, M. J. F., Berné, O., Boersma, C., Allamandola, L. J., & Tielens, A. G. G. M. 2011, *A&A*, 532, A128
- Sales, D. A., Pastoriza, M. G., & Riffel, R. 2010, *ApJ*, 725, 605
- Sargsyan, L., Weedman, D., Lebouteiller, V., et al. 2011, *ApJ*, 730, 19
- Seok, J. Y., & Li, A. 2015, *ApJ*, 809, 22
- Schmidt, M., & Green, R. F. 1983, *ApJ*, 269, 352
- Shangguan, J., Ho, L. C., & Xie, Y. 2018, *ApJ*, 854, 158
- Shannon, M. J., Stock, D. J., & Peeters, E. 2016, *ApJ*, 824, 111
- Shi, Y., Rieke, G. H., Ogle, P. M., Su, K. Y. L., & Balog, Z. 2014, *ApJS*, 214, 23
- Smith, J. D. T., Draine, B. T., Dale, D. A., et al. 2007, *ApJ*, 656, 770
- Spoon, H. W. W., Tielens, A. G. G. M., Armus, L., et al. 2006, *ApJ*, 638, 759
- Tanaka, M., Matsumoto, T., Murakami, H., et al. 1996, *PASJ*, 48, L53
- Tielens, A. G. G. M. 2008, *ARA&A*, 46, 289
- Veilleux, S., Rupke, D. S. N., Kim, D.-C., et al. 2009, *ApJS*, 182, 628
- Vermeij, R., Peeters, E., Tielens, A. G. G. M., & van der Hulst, J. M. 2002, *A&A*, 382, 1042
- Wang, S., Li, A., & Jiang, B. W. 2015, *ApJ*, 811, 38
- Weingartner, J. C., & Draine, B. T. 2001a, *ApJ*, 548, 296
- Weingartner, J. C., & Draine, B. T. 2001b, *ApJ*, 553, 581
- Werner, M. W., Roellig, T. L., Low, F. J., et al. 2004, *ApJS*, 154, 1
- Wu, Y., Helou, G., Armus, L., et al. 2010, *ApJ*, 723, 895
- Xie, Y., Li, A., & Hao, L. 2017, *ApJS*, 228, 6
- Yang, X. J., Glaser, R., Li, A., & Zhong, J. X. 2017a, *New A Rev.*, 77, 1
- Yang, X. J., Li, A., Glaser, R., & Zhong, J. X. 2017b, *ApJ*, 837, 171
- Yuan, T.-T., Kewley, L. J., & Sanders, D. B. 2010, *ApJ*, 709, 884

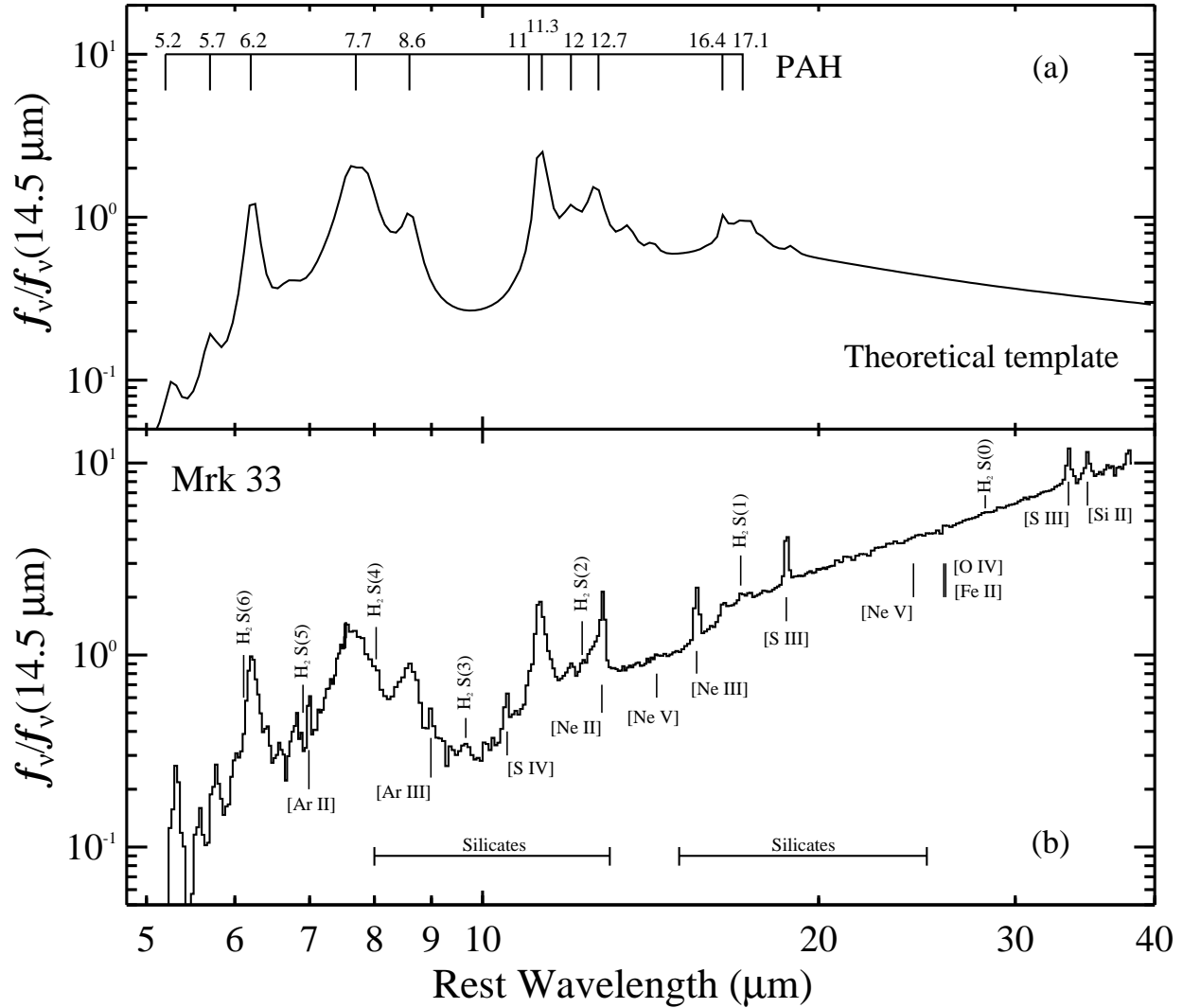


Fig. 1.— (a) Sample theoretical PAH spectrum from Draine & Li (2007), calculated with starlight intensity scale factor $U = 1$, illustrating the location of the prominent PAH emission features in the MIR. (b) Sample IRS spectrum of the star-forming galaxy Mrk 33, highlighting the locations of the most prominent ionic and molecular hydrogen emission lines and broad silicate absorption features at ~ 10 and $18 \mu\text{m}$.

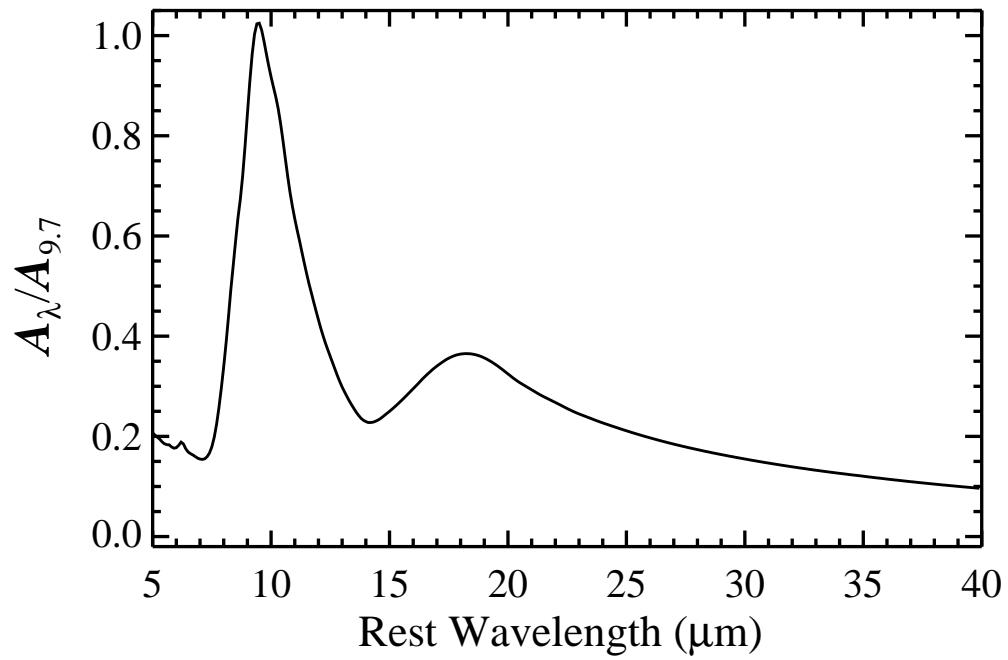


Fig. 2.— The MIR extinction curve normalized at $9.7\ \mu\text{m}$ adopted in the current work, from Wang et al. (2015).

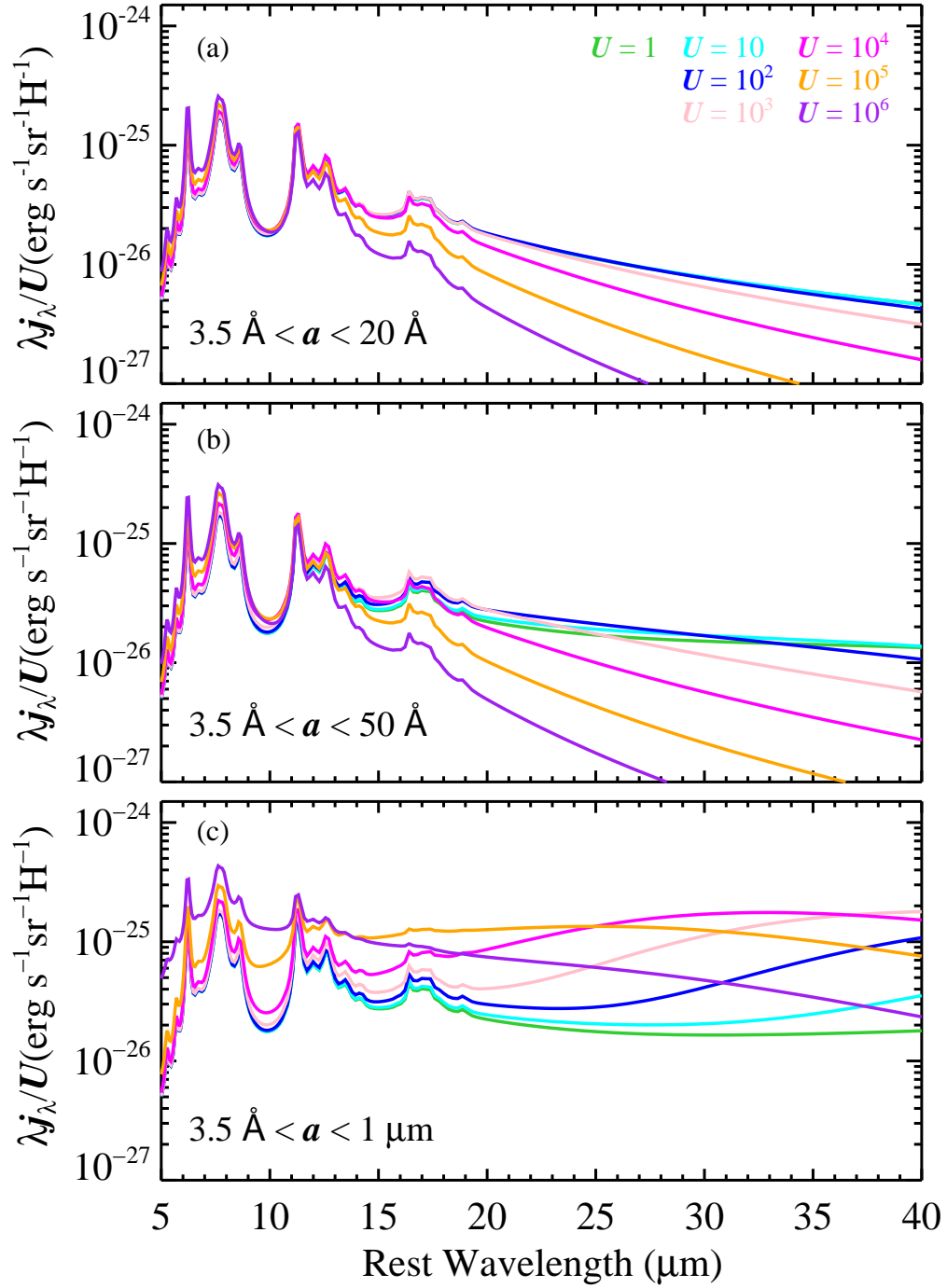


Fig. 3.— Theoretical emission spectra of carbonaceous dust for selected starlight intensity scale factors U ranging from 1 to 10^6 , for (a) grain sizes $< 20 \text{ \AA}$, (b) grain sizes $< 50 \text{ \AA}$, and (c) the full grain size distribution.

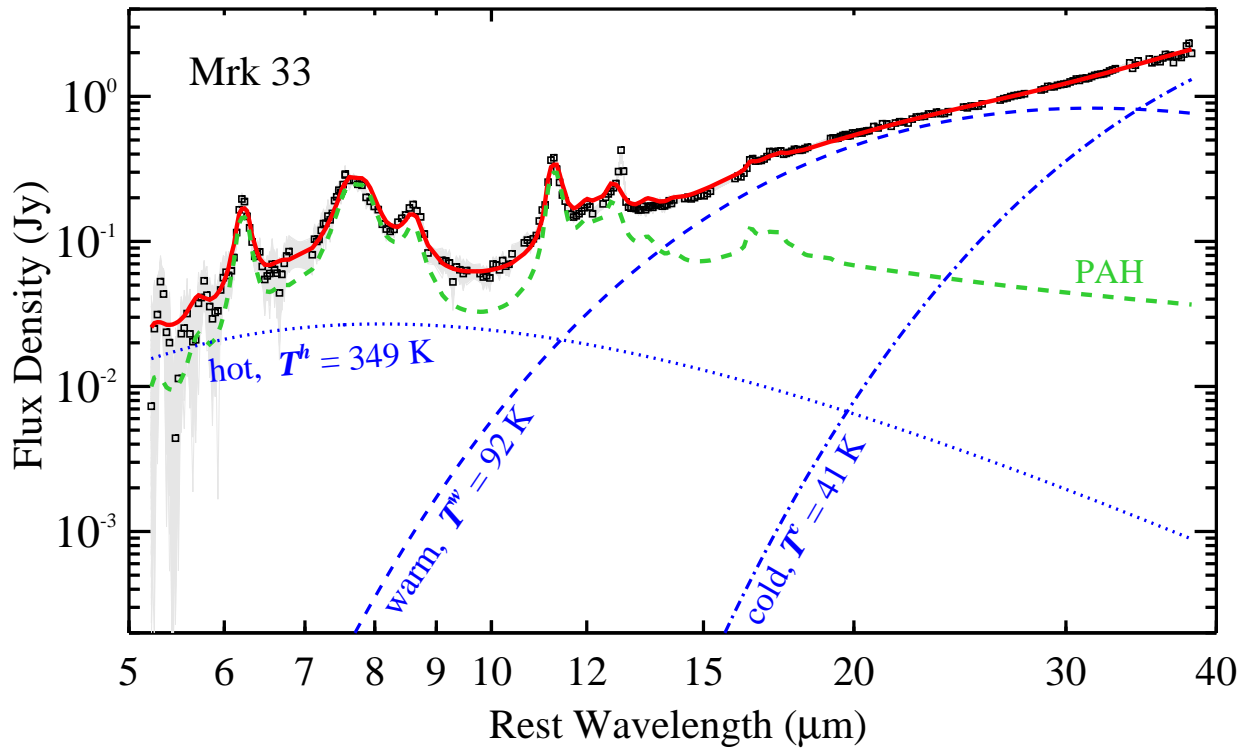


Fig. 4.— Illustration of the method to determine the errors of the best-fit parameters for Mrk33. The observed IRS spectrum is plotted as black squares. The best-fit model (solid red line) comprises the theoretical PAH template (green dashed line) and three modified blackbody components (blue lines) for the hot (dotted), warm (dashed), and cold (dot-dashed) dust continuum. The gray shaded region denotes simulated spectra generated from 500 Monte Carlo realizations.

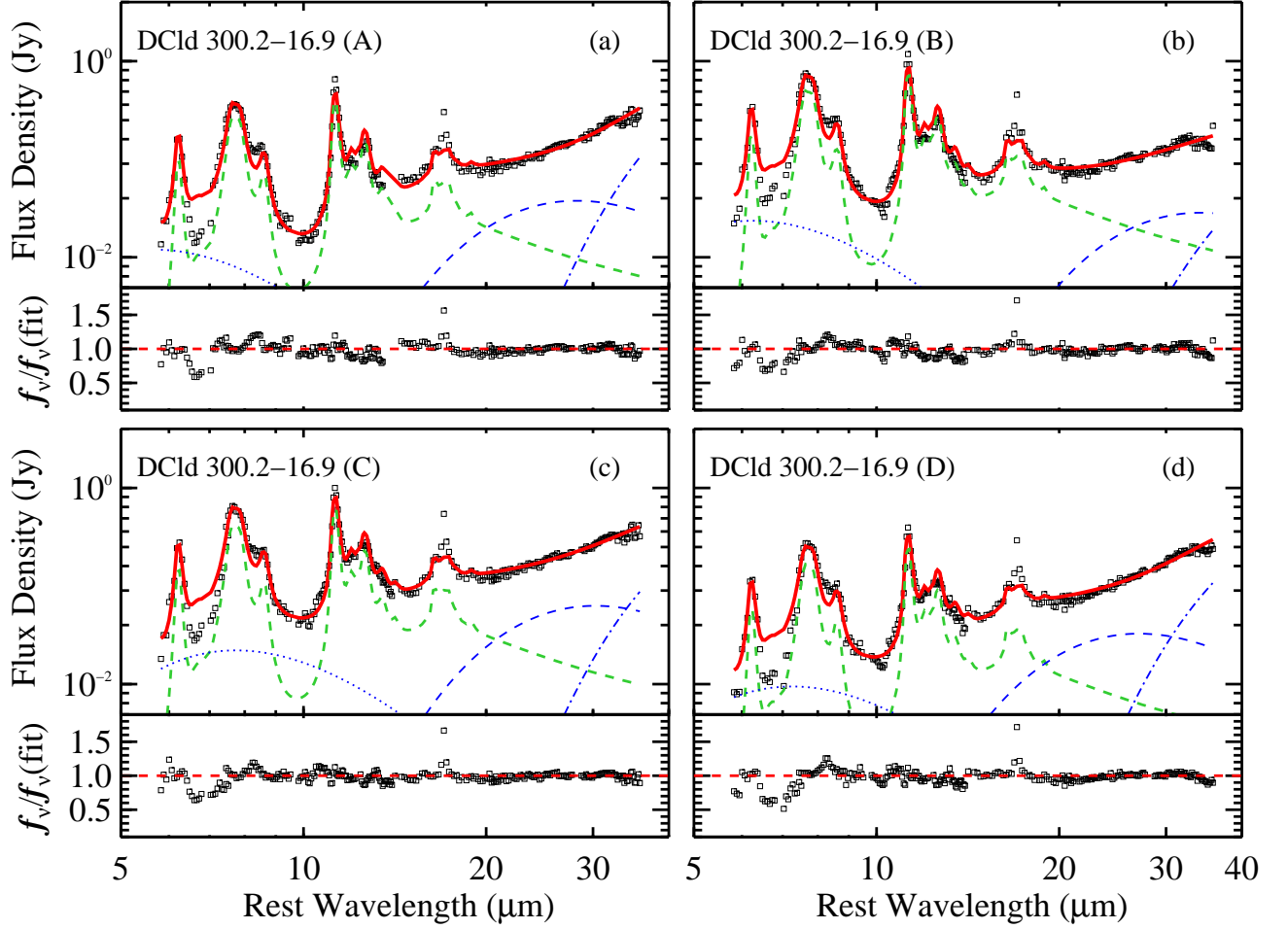


Fig. 5.— Decomposition of the IRS spectra of Galactic HLCs (a) DCld 300.2–16.9(A), (b) DCld 300.2–16.9(B), (c) DCld 300.2–16.9(C), and (d) DCld 300.2–16.9(D). For each source, the top panel shows the observed spectrum (black squares) and the best-fit model (solid red line), comprising a theoretical PAH template (green dashed line) and three modified blackbody components (blue lines) for the hot (dotted), warm (dashed), and cold (dot-dashed) dust continuum. The bottom panel shows the ratio of the observed spectrum with the best-fit model.

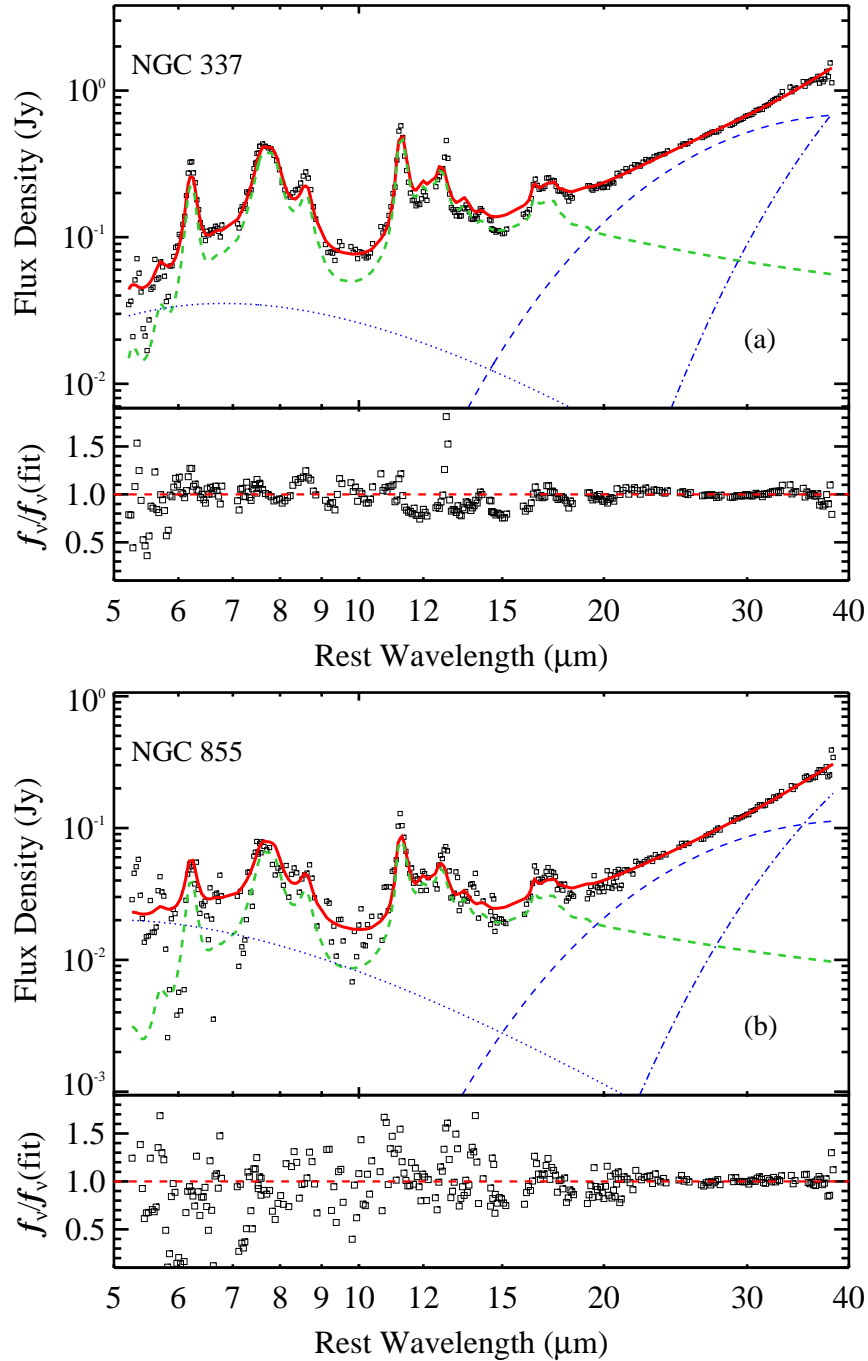


Fig. 6.— Decomposition of the IRS spectra of the SINGS H II galaxies (a) NGC 337 and (b) NGC 855. For each source, the top panel shows the observed spectrum (black squares) and the best-fit model (solid red line), comprising a theoretical PAH template (green dashed line) and three modified blackbody components (blue lines) for the hot (dotted), warm (dashed), and cold (dot-dashed) dust continuum. The bottom panel shows the ratio of the observed spectrum with the best-fit model. The results for all SINGS H II galaxies analyzed in this study are available in the online version of the paper.

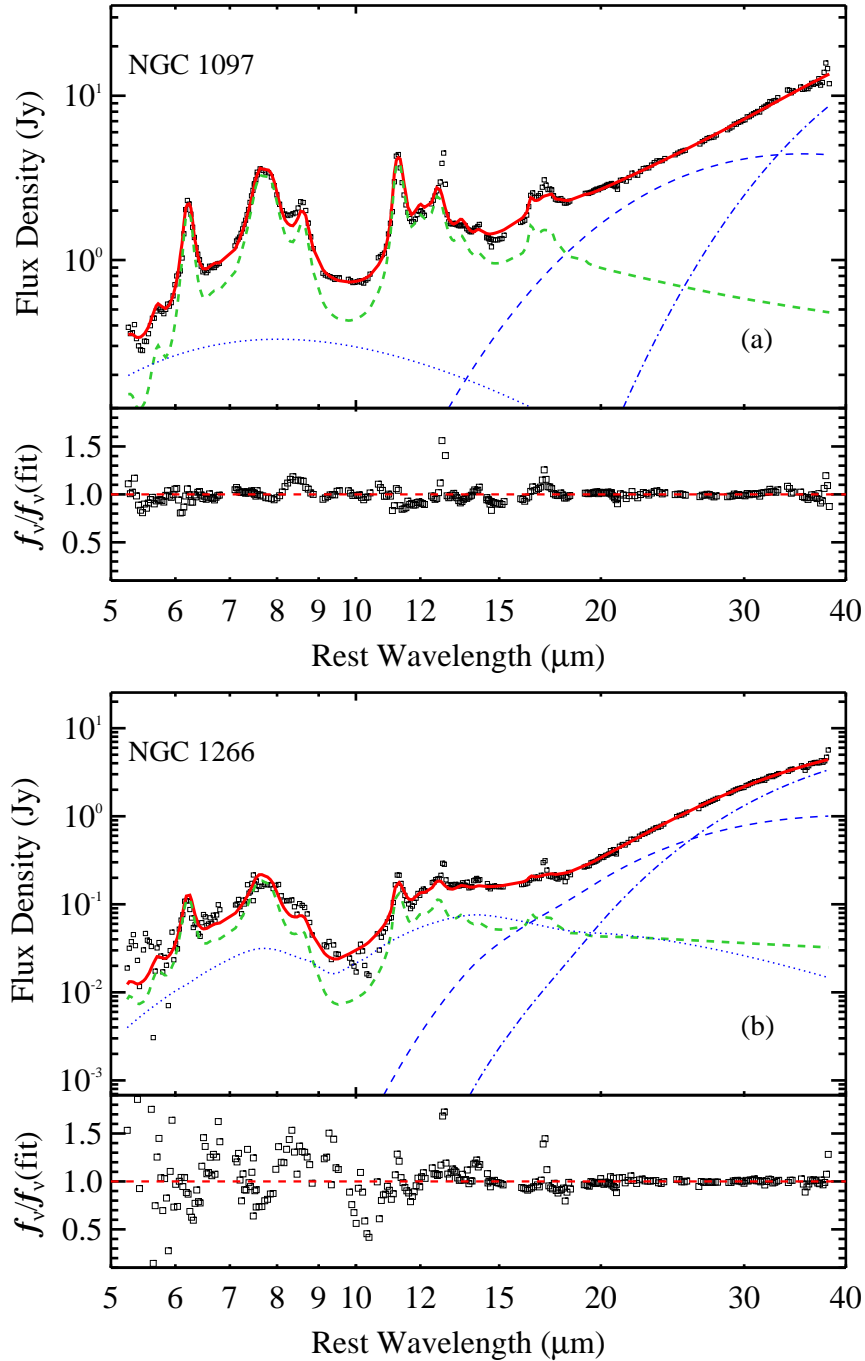


Fig. 7.— Decomposition of the IRS spectra of the SINGS AGNs (a) NGC 1097 and (b) NGC 1266. For each source, the top panel shows the observed spectrum (black squares) and the best-fit model (solid red line), comprising a theoretical PAH template (green dashed line) and three modified blackbody components (blue lines) for the hot (dotted), warm (dashed), and cold (dot-dashed) dust continuum. The bottom panel shows the ratio of the observed spectrum with the best-fit model. The results for all SINGS AGN galaxies analyzed in this study are available in the online version of the paper.

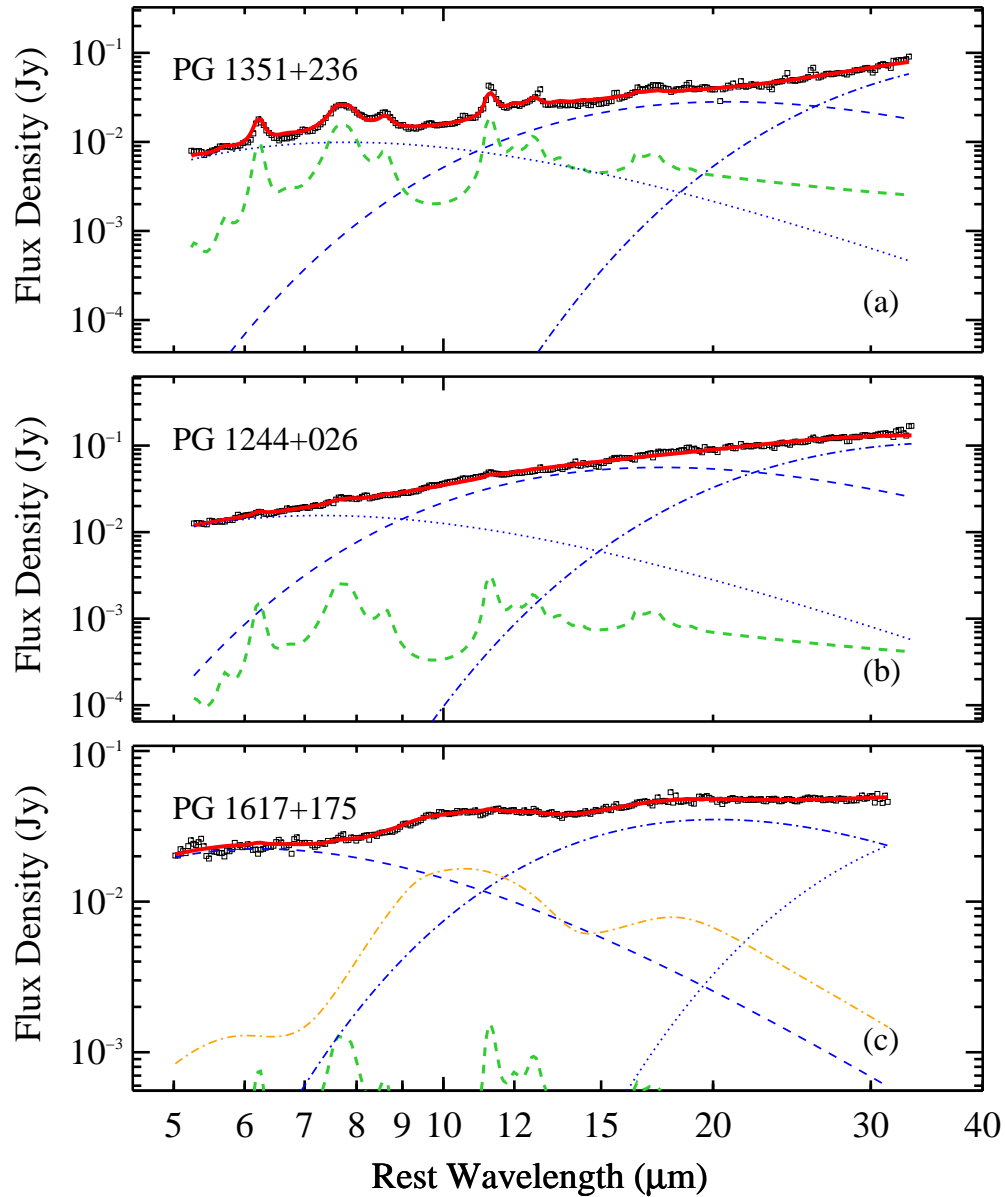


Fig. 8.— Decomposition of the IRS spectra of the quasars (a) PG 1351+236, which shows strong PAH emission; (b) PG 1244+026, which shows very weak PAH emission and a flat featureless continuum; and (c) PG 1617+175, which shows no PAH features but strong silicate emission at 10 and 18 μm . For each source, we show the observed spectrum (black squares) and the best-fit model (solid red line), comprising a theoretical PAH template (green dashed line) and three modified blackbody components (blue lines) for the hot (dotted), warm (dashed), and cold (dot-dashed) dust continuum. The silicate emission component in PG 1617+175 is shown as an orange dot-dashed line.

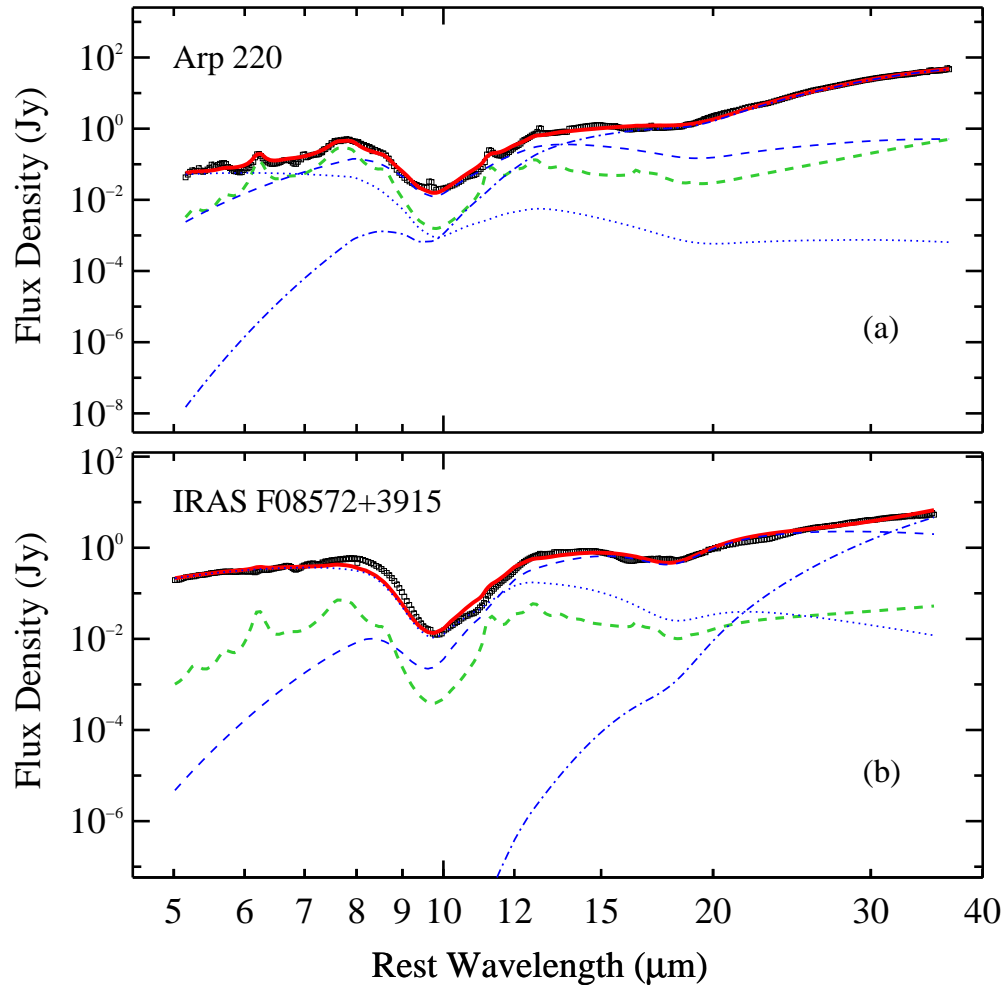


Fig. 9.— Decomposition of the IRS spectra of the highly obscured, IR-luminous galaxies (a) Arp 220, which shows PAH emission and silicate absorption, and (b) IRAS F08572+3915, which does not have detectable PAH emission but has strong silicate absorption at 10 and 18 μm . For each source, we show the observed spectrum (black squares) and the best-fit model (solid red line), comprising a theoretical PAH template (green dashed line) and three modified blackbody components (blue lines) for the hot (dotted), warm (dashed), and cold (dot-dashed) dust continuum.

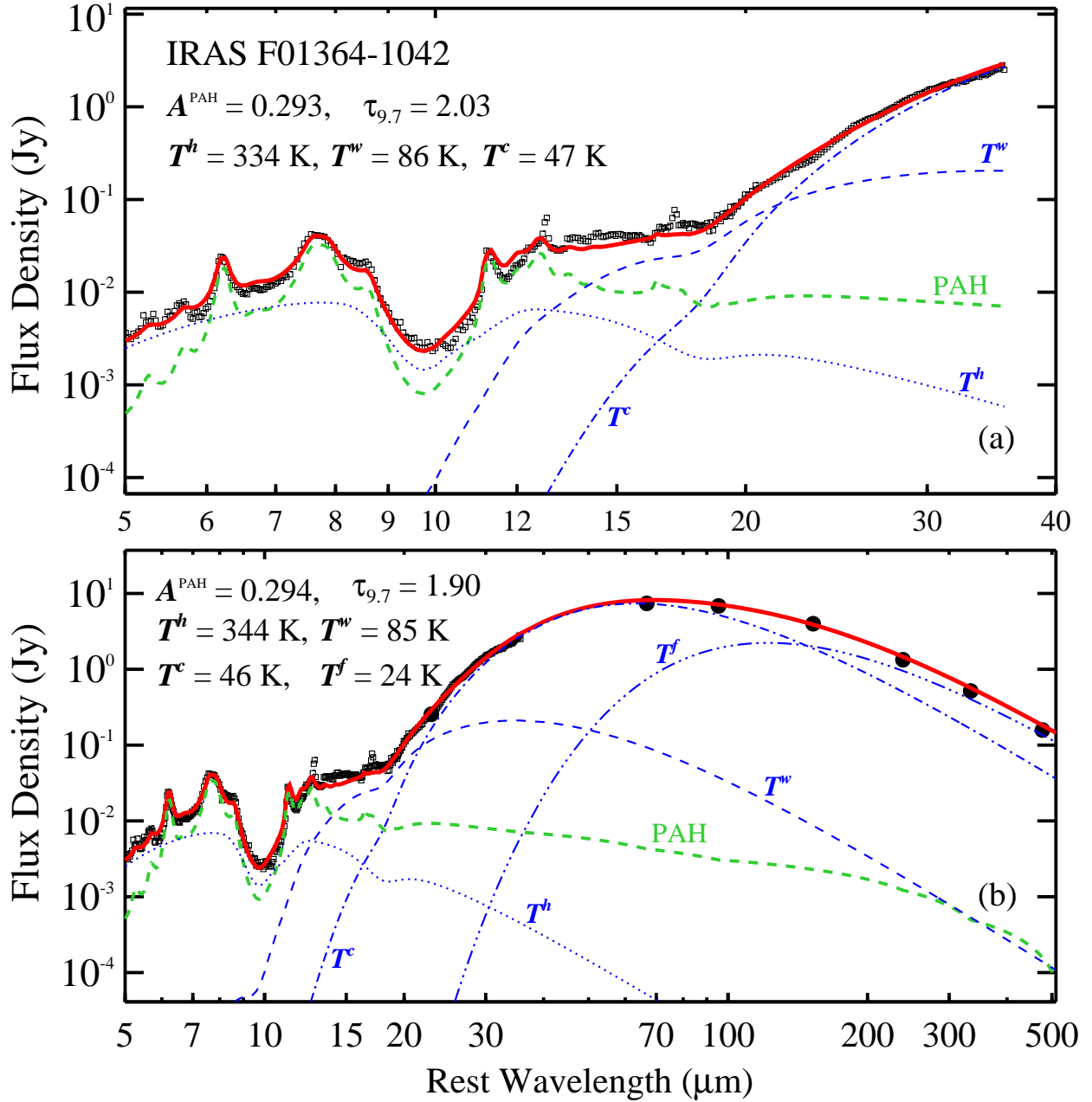


Fig. 10.— (a) Decomposition of the IRS spectrum of IRAS F01364–1042 (black squares). The best-fit model (solid red line) comprises a theoretical PAH template (green dashed line) and three modified blackbody components (blue lines) for the hot (dotted), warm (dashed), and cold (dot-dashed) dust continuum. (b) Decomposition of the IRS spectrum of IRAS F01364–1042 with the SED extended to the FIR using photometric measurements from *Herschel* at 70, 100, 160, 250, 350, and 500 μm . An additional cold dust component with $T^f = 24$ K is required to fit the long-wavelength data, but the best-fit parameters of the original fit to the IRS are not significantly affected.

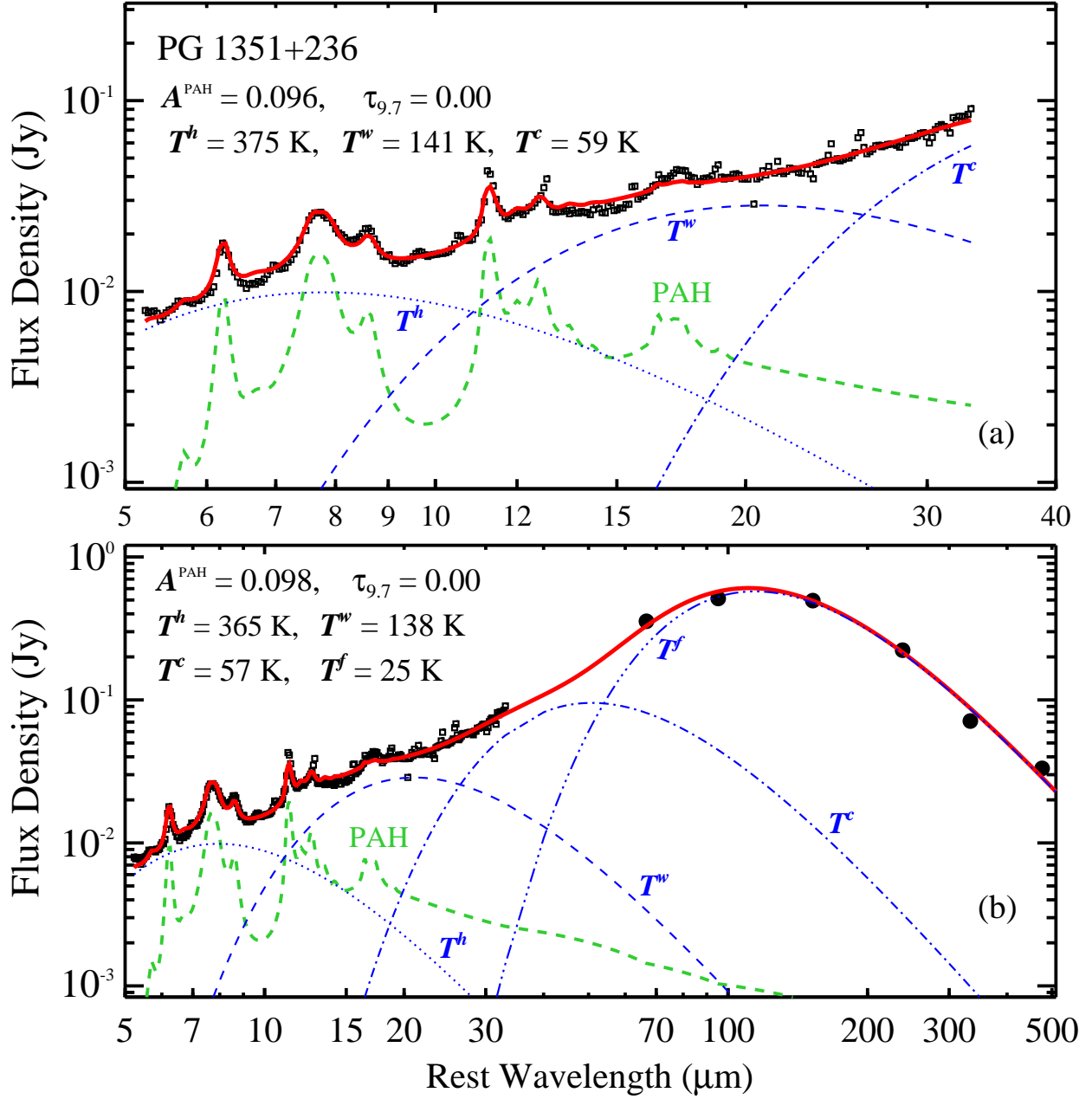


Fig. 11.— (a) Decomposition of the IRS spectrum of PG 1351+236 (black squares). The best-fit model (solid red line) comprises a theoretical PAH template (green dashed line) and three modified blackbody components (blue lines) for the hot (dotted), warm (dashed), and cold (dot-dashed) dust continuum. (b) Decomposition of the IRS spectrum of PG 1351+236 with the SED extended to the FIR using photometric measurements from *Herschel* at 70, 100, 160, 250, 350, and 500 μm . An additional cold dust component with $T^f = 25$ K is required to fit the long-wavelength data, but the best-fit parameters of the original fit to the IRS are not significantly affected.

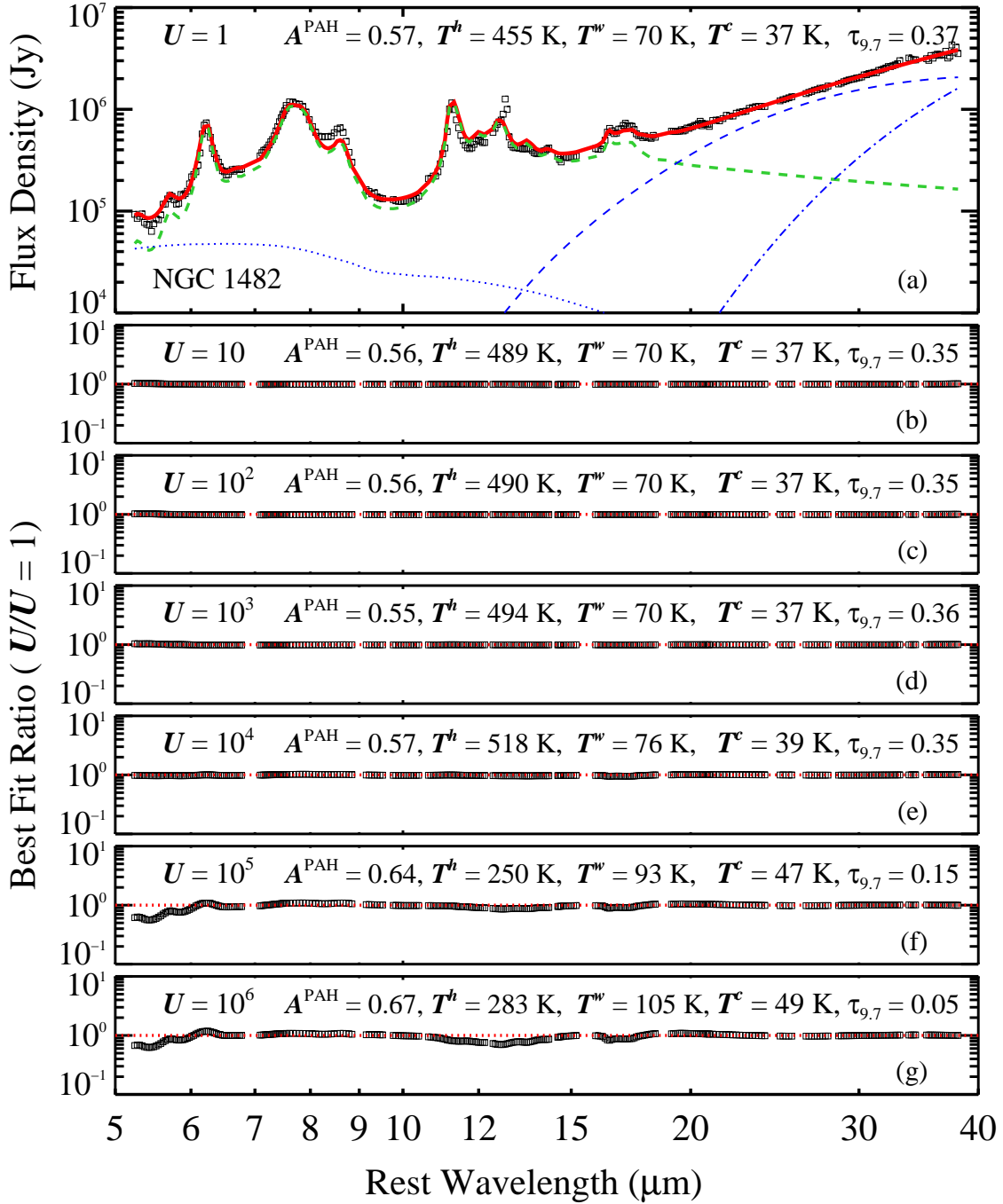


Fig. 12.— (a) Decomposition of the IRS spectrum of NGC1482 (black squares). The best-fit model (solid red line) comprises a theoretical PAH template calculated with $U = 1$ and dust grains with sizes $a < 20$ Å (green dashed line) and three modified blackbody components (blue lines) for the hot (dotted), warm (dashed), and cold (dot-dashed) dust continuum. The bottom panels show the ratio of the best-fit model relative to the model with $U = 1$ for (b) $U = 10$, (c) $U = 10^2$, (d) $U = 10^3$, (e) $U = 10^4$, (f) $U = 10^5$, and (g) $U = 10^6$. The derived model parameters are relatively insensitive to U within the range explored.

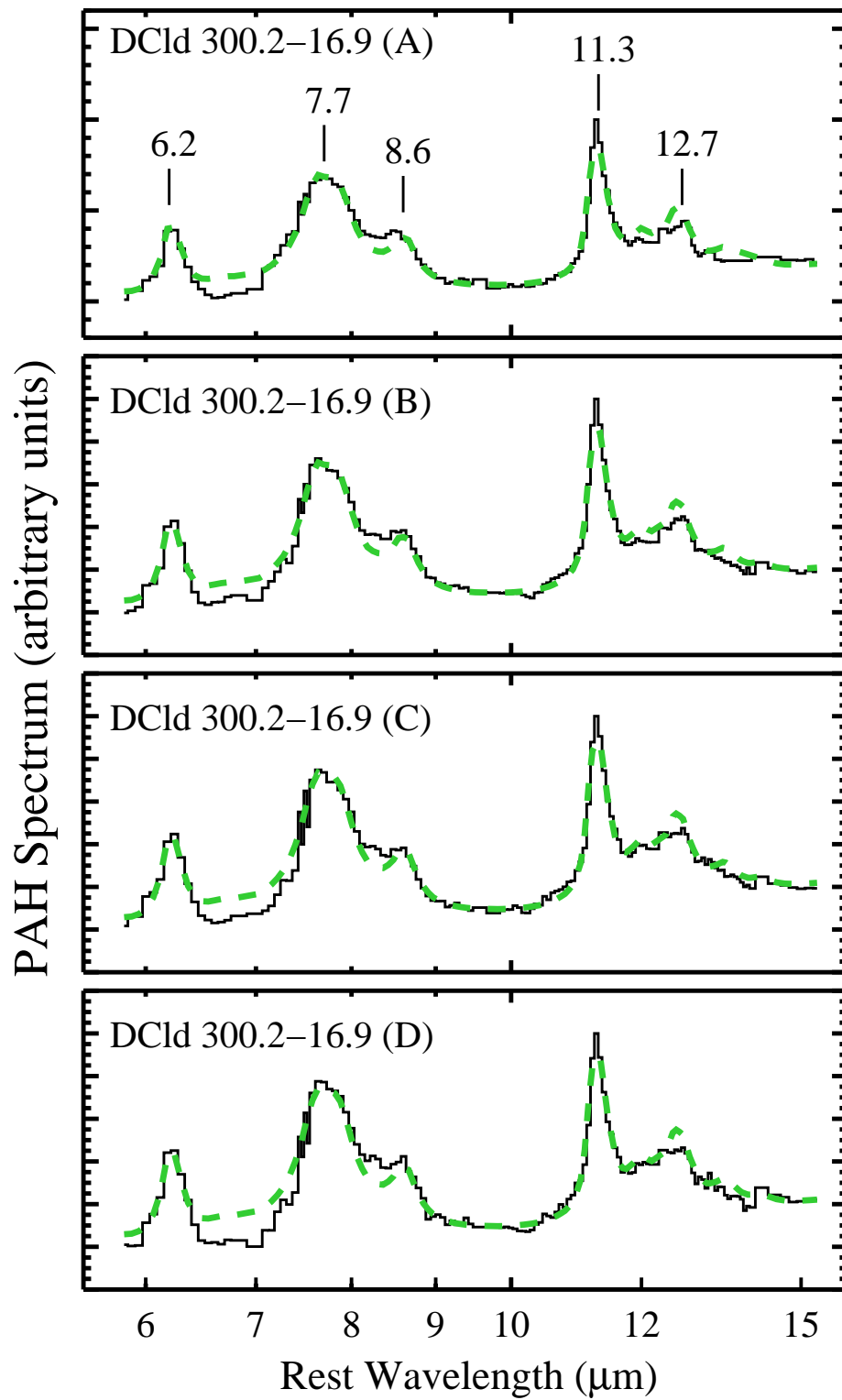


Fig. 13.— Comparison of the observed PAH spectra for the HLCs (black histograms), obtained from our decomposition, with the best-fit theoretical template (green dashed line). The five most prominent PAH features are labeled.

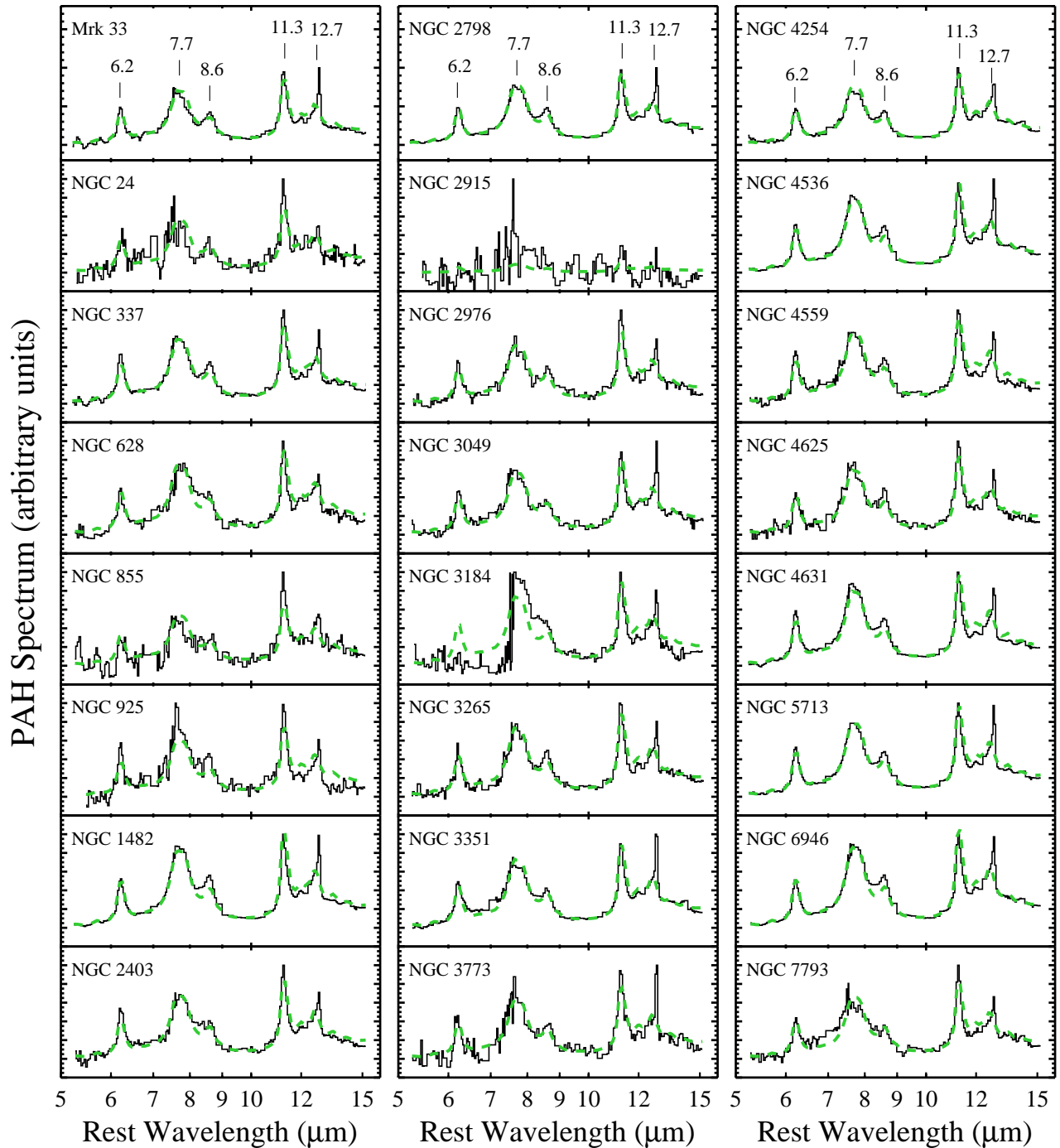


Fig. 14.— Comparison of the observed PAH spectra for the SINGS H II galaxies (black histograms), obtained from our decomposition, with the best-fit theoretical template (green dashed line). The five most prominent PAH features are labeled. The PAH spectra are remarkably invariant.

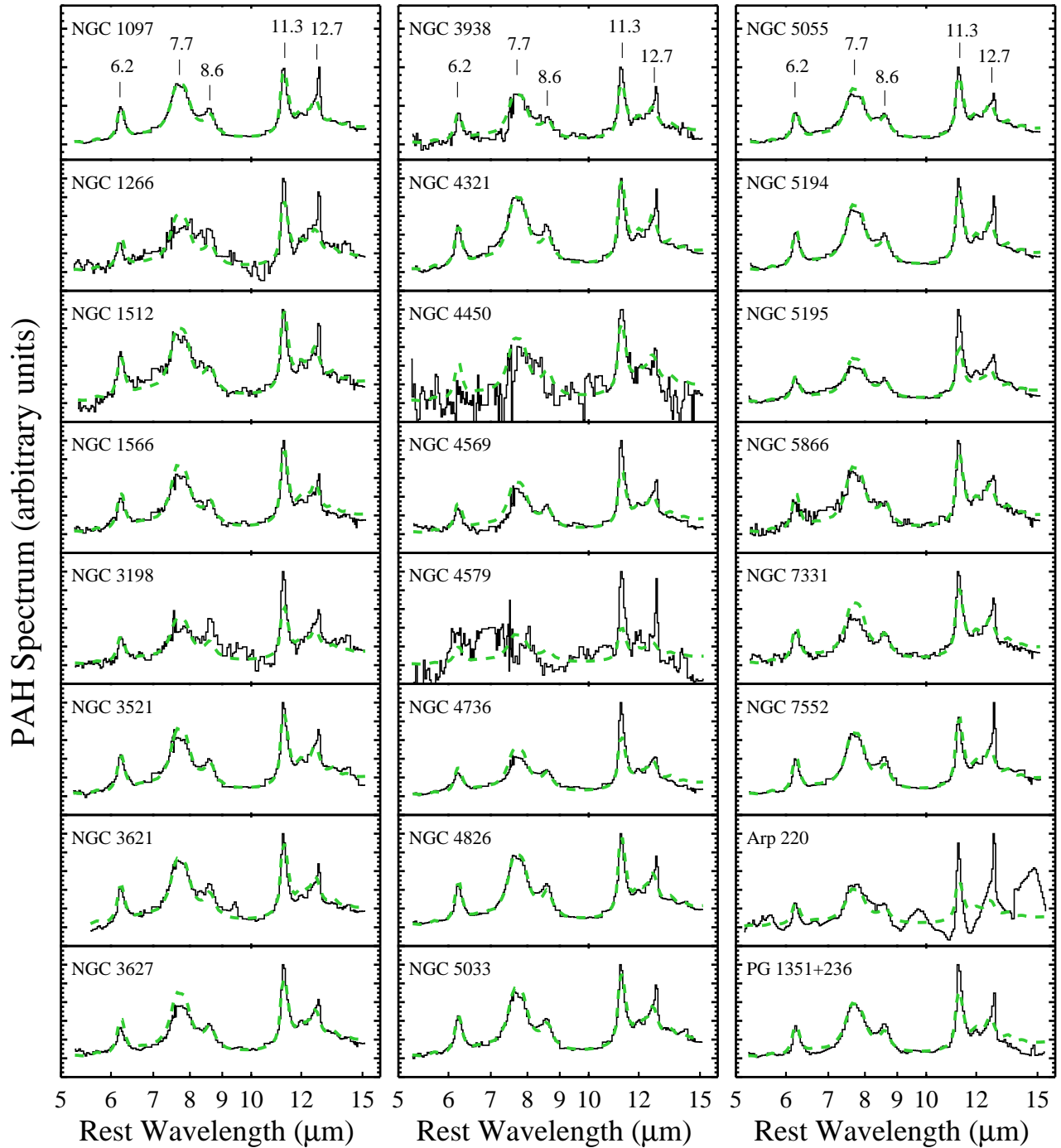


Fig. 15.— Comparison of the observed PAH spectra for the SINGS AGNs, Arp 220, and PG 1351+236 (black histograms), obtained from our decomposition, with the best-fit theoretical template (green dashed line). The five most prominent PAH features are labeled. The PAH spectra are remarkably invariant.

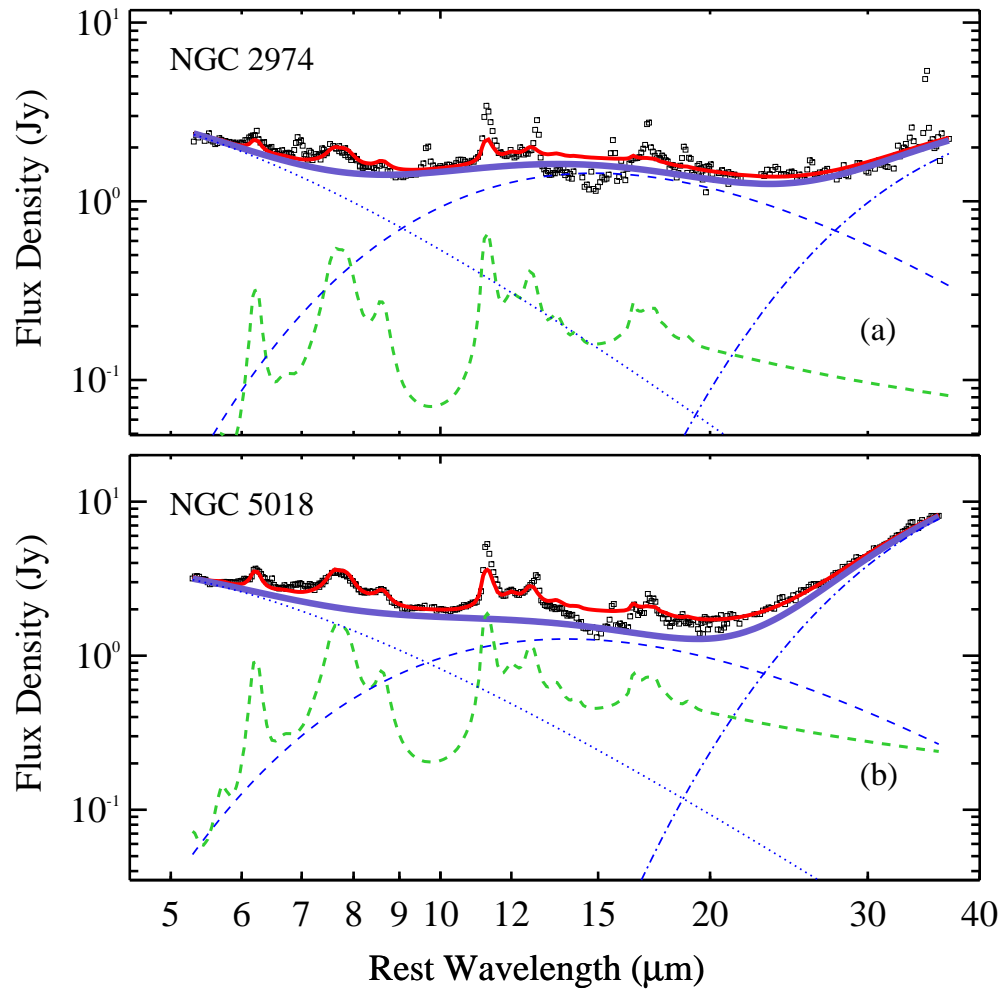


Fig. 16.— Decomposition of the *Spitzer*/IRS spectra of the elliptical galaxies (a) NGC2974 and (b) NGC5018, which show peculiar PAH emission (Kaneda et al. 2008). For each source, we show the observed spectrum (black squares) and the best-fit model (solid red line), which comprises a theoretical PAH template (green dashed line) and three modified blackbody components (blue lines) for the hot (dotted), warm (dashed), and cold (dot-dashed) dust continuum. Also shown is the overall continuum (purple line) obtained by summing the three modified blackbody components.

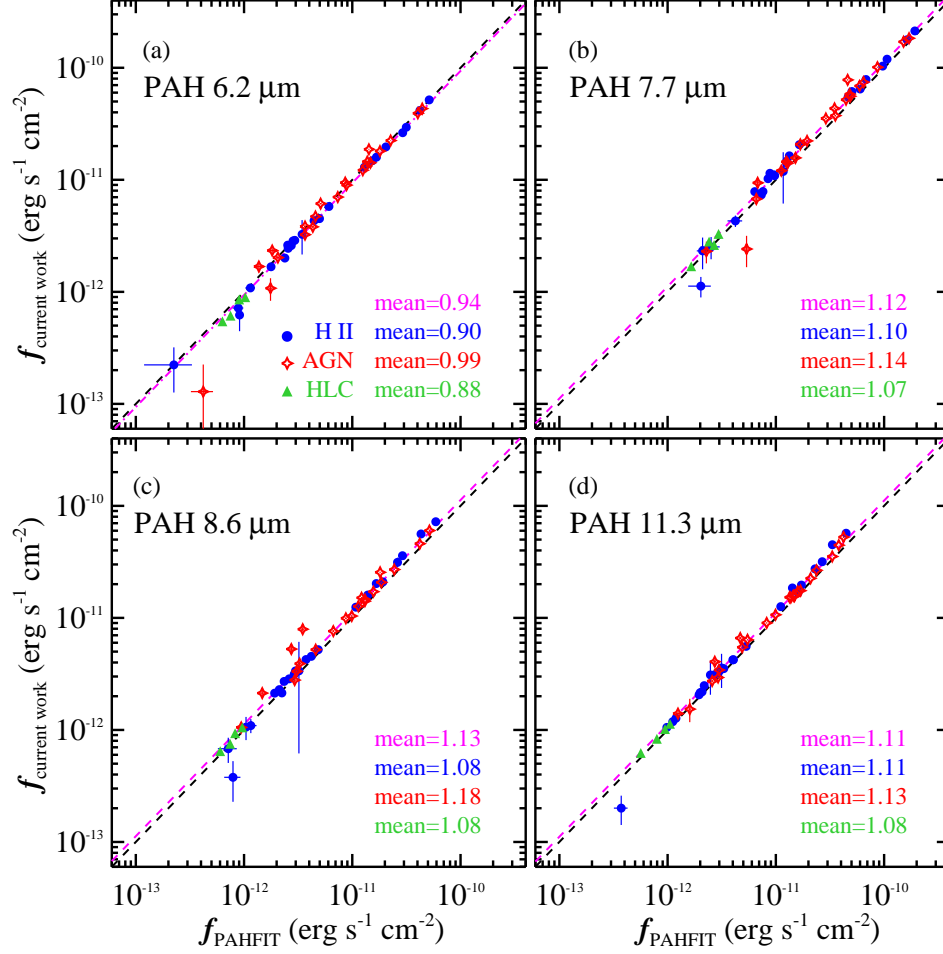


Fig. 17.— Comparison of the PAH fluxes derived from the current template-fitting method with those from PAHFIT for the features at (a) 6.2 μm, (b) 7.7 μm, (c) 8.6 μm, and (d) 11.3 μm. Our PAH fluxes were derived directly from the observed spectra, after subtraction of the best-fit model continuum. In each panel, the black dashed line indicates the one-to-one relation, and the magenta dashed line represents the mean value of all SINGS H II galaxies, AGNs, and HLCs calculated from the ratio of fluxes from our measurements and those derived from PAHFIT. Separate mean ratios for the HLCs, H II galaxies, and AGNs are also displayed.

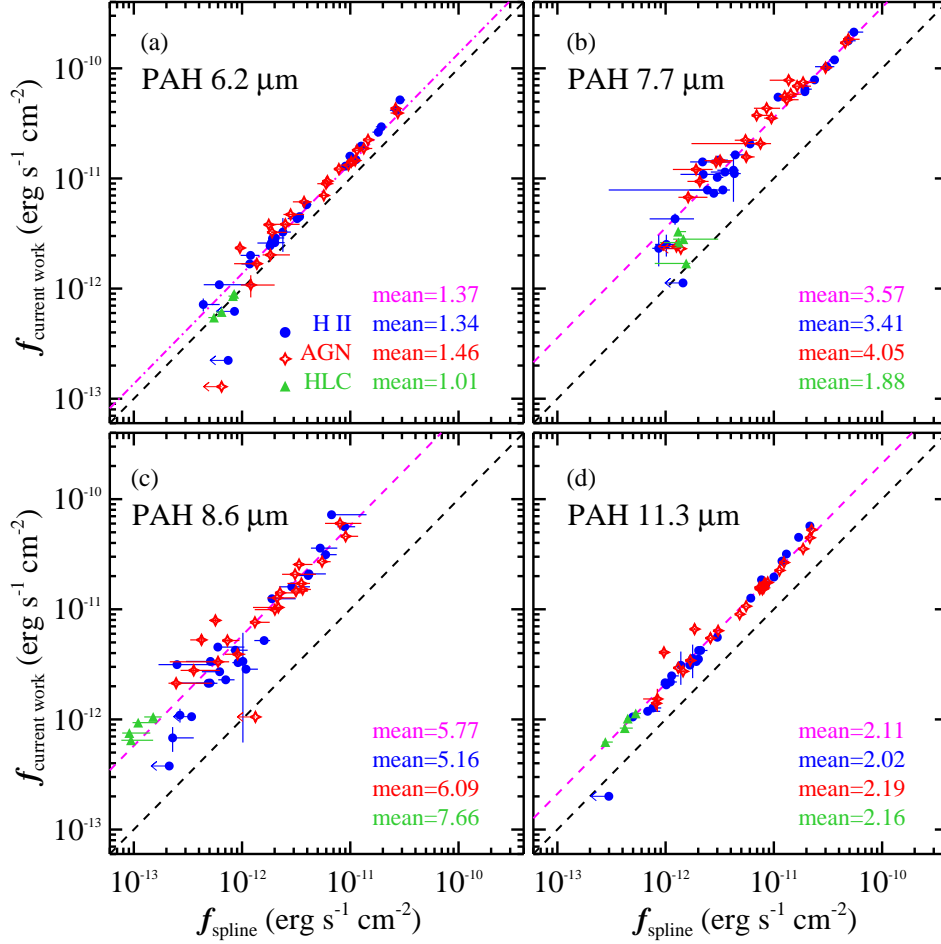


Fig. 18.— Comparison of the PAH fluxes derived from the current template-fitting method with those from the spline fit method, for the features at (a) 6.2 μm, (b) 7.7 μm, (c) 8.6 μm, and (d) 11.3 μm. Our PAH fluxes were derived directly from the observed spectra after subtraction of the best-fit model continuum. In each panel, the black dashed line indicates the one-to-one relation, and the magenta dashed line represents the mean value of all SINGS H II galaxies, AGNs, and HLCs calculated from the ratio of fluxes from our measurements and those derived from the spline method. Separate mean ratios for the HLCs, H II galaxies, and AGNs are also displayed.

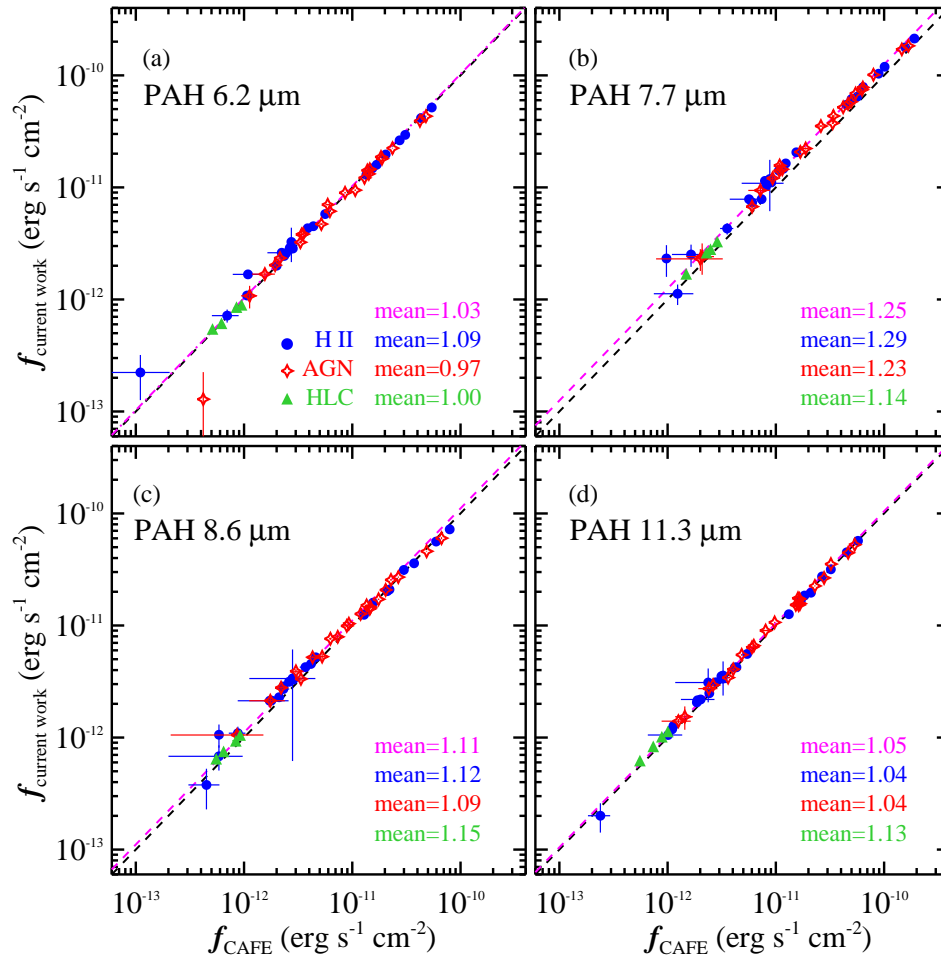


Fig. 19.— Comparison of the PAH fluxes derived from the current template-fitting method with those from CAFE for the features at (a) 6.2 μm , (b) 7.7 μm , (c) 8.6 μm , and (d) 11.3 μm . Our PAH fluxes were derived directly from the observed spectra after subtraction of the best-fit continuum model. In each panel, the black dashed line indicates the one-to-one relation, and the magenta dashed line represents the mean value of all SINGS H II galaxies, AGNs, and HLCs, calculated from the ratio of fluxes from our measurements and those derived from CAFE. Separate mean ratios for the HLCs, H II galaxies, and AGNs are also displayed.

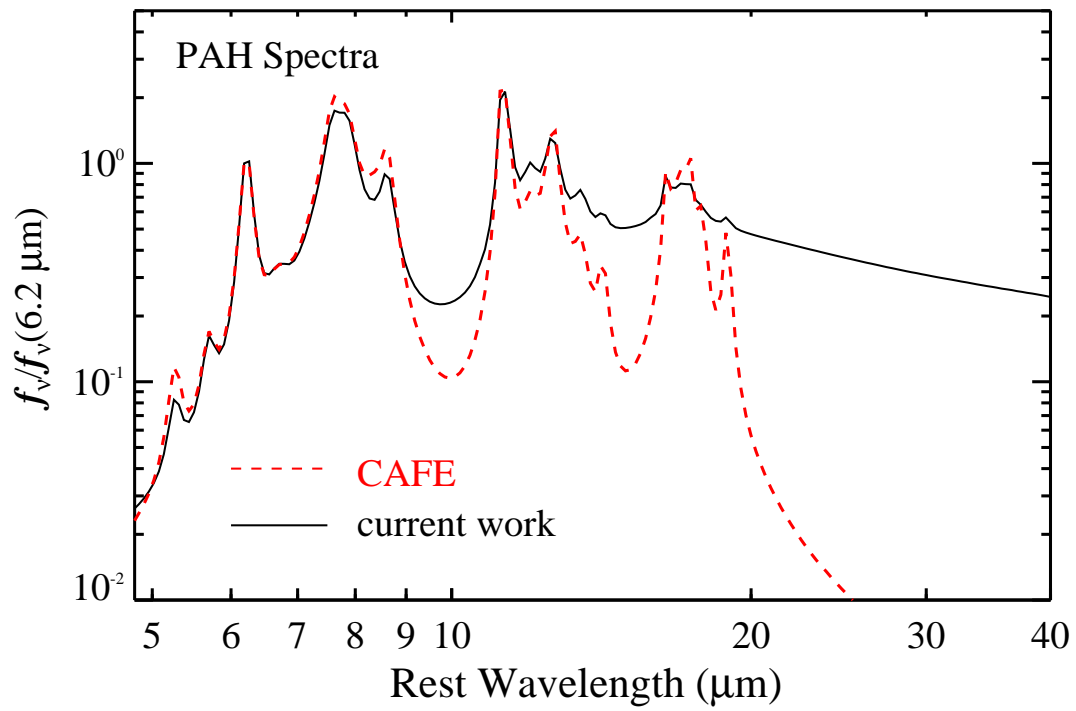


Fig. 20.— Comparison of the PAH template spectrum adopted in the current work (solid black line) with that used in CAFE (red dashed line; Marshall et al. 2007).

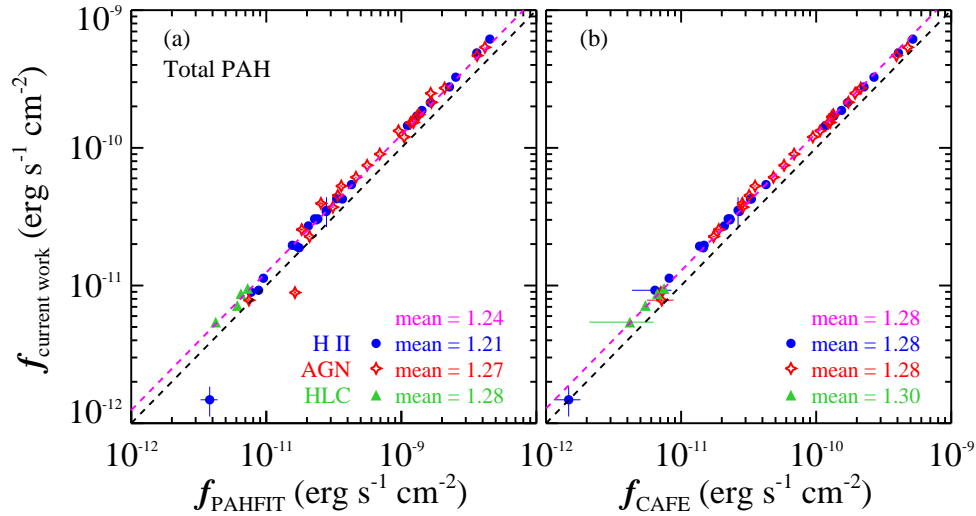


Fig. 21.— Comparison of the total PAH flux derived from the current template-fitting method with those from (a) PAHFIT and (b) CAFE, considering PAH emission between 5 and 20 μm . The black dashed line indicates the one-to-one relation, and the magenta dashed line represents the mean value of all SINGS H II galaxies, AGNs, and HLCs calculated from the ratio of fluxes from our measurements and those of the other methods. Separate mean ratios for the HLCs, H II galaxies, and AGNs are also given.

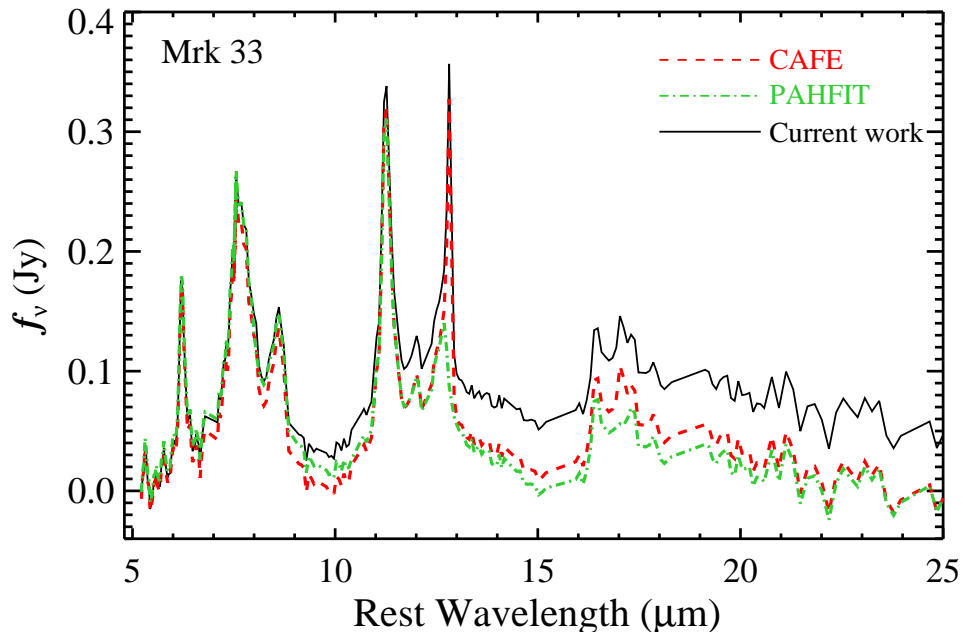


Fig. 22.— Comparison of the “residual” PAH spectra of Mrk 33, a star-forming galaxy, obtained by subtracting (from its *Spitzer*/IRS spectrum) the best-fit continuum derived, respectively, from our technique (black solid line), PAHFIT (green dot-dashed line), and CAFE (red dashed line).

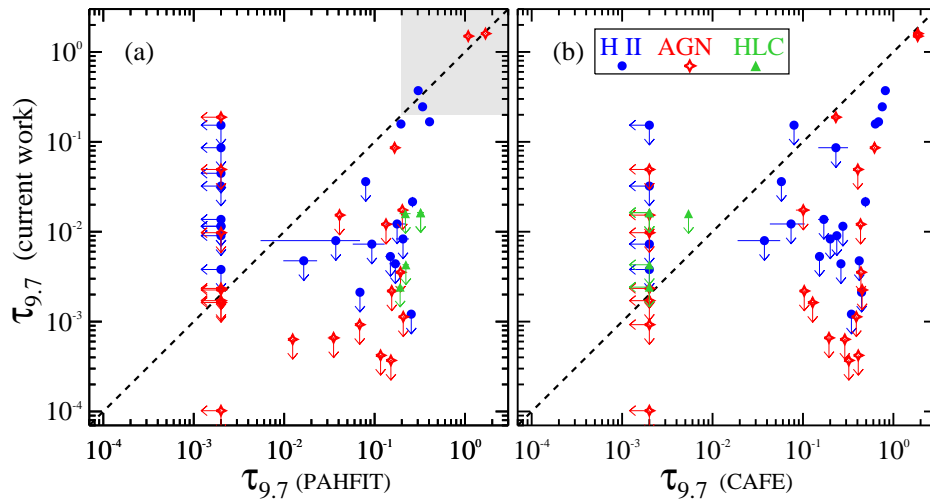


Fig. 23.— Comparison of the $9.7\ \mu\text{m}$ optical depth derived from our template-fitting method with those from (a) PAHFIT and (b) CAFE. Objects that have extinction values equal to zero from PAHFIT or CAFE are assigned an artificial value of 2×10^{-3} . In panel (a), the two methods give comparable extinction values when $\tau_{9.7} > 0.2$ (shaded region).

Table 1. Basic Parameters for Galactic High-latitude Clouds

| Source | R.A. (J2000) (hh mm ss.s) | Decl. (J2000) (dd mm ss) | Type | Distance (pc) | Extraction Aperture (arcsec \times arcsec) |
|---------------------|------------------------------|-----------------------------|------|------------------|---|
| (1) | (2) | (3) | (4) | (5) | (6) |
| DCld 300.2-16.9 (A) | 11 54 23.1 | -79 31 42 | HLC | 70 \pm 15 | 142.8 \times 10.7 |
| DCld 300.2-16.9 (B) | 11 52 08.3 | -79 09 33 | HLC | 70 \pm 15 | 142.8 \times 10.7 |
| DCld 300.2-16.9 (C) | 11 48 24.4 | -79 18 00 | HLC | 70 \pm 15 | 142.8 \times 10.7 |
| DCld 300.2-16.9 (D) | 11 55 33.8 | -79 20 54 | HLC | 70 \pm 15 | 142.8 \times 10.7 |

Table 2. Basic Parameters for SINGS Sample

| Source | R.A. (J2000) (hh mm ss.s) | Decl. (J2000) (dd mm ss.s) | Type | Distance (Mpc) | Extraction Aperture (arcsec \times arcsec) |
|----------------|------------------------------|-------------------------------|---------|-------------------|---|
| (1) | (2) | (3) | (4) | (5) | (6) |
| Mrk 33 | 10 32 31.82 | +54 24 02.5 | H II | 22.9 | 52 \times 30 |
| NGC 24 | 00 09 56.37 | -24 57 51.2 | H II | 7.3 | 52 \times 30 |
| NGC 337 | 00 59 50.20 | -07 34 45.8 | H II | 22.4 | 52 \times 30 |
| NGC 628 | 01 36 41.60 | +15 47 00.0 | H II | 7.3 | 52 \times 30 |
| NGC 855 | 02 14 03.70 | +27 52 38.4 | H II | 9.6 | 52 \times 30 |
| NGC 925 | 02 27 17.25 | +33 34 41.6 | H II | 9.1 | 52 \times 30 |
| NGC 1482 | 03 54 38.88 | -20 30 07.1 | H II | 23.2 | 52 \times 30 |
| NGC 2403 | 07 36 49.95 | +65 36 03.5 | H II | 3.2 | 52 \times 30 |
| NGC 2798 | 09 17 22.80 | +41 59 59.4 | H II | 26.2 | 52 \times 30 |
| NGC 2915 | 09 26 10.03 | -76 37 32.2 | H II | 3.8 | 52 \times 30 |
| NGC 2976 | 09 47 15.22 | +67 55 00.3 | H II | 3.6 | 52 \times 30 |
| NGC 3049 | 09 54 49.59 | +09 16 18.1 | H II | 23.9 | 52 \times 30 |
| NGC 3184 | 10 18 16.90 | +41 25 24.7 | H II | 11.1 | 52 \times 30 |
| NGC 3265 | 10 31 06.80 | +28 47 45.6 | H II | 23.2 | 52 \times 30 |
| NGC 3351 | 10 43 57.72 | +11 42 13.5 | H II | 9.3 | 52 \times 30 |
| NGC 3773 | 11 38 12.98 | +12 06 45.8 | H II | 11.9 | 52 \times 30 |
| NGC 4254 | 12 18 49.57 | +14 24 57.5 | H II | 16.6 | 52 \times 30 |
| NGC 4536 | 12 34 27.03 | +02 11 16.5 | H II | 14.4 | 52 \times 30 |
| NGC 4559 | 12 35 57.58 | +27 57 34.2 | H II | 10.3 | 52 \times 30 |
| NGC 4625 | 12 41 52.68 | +41 16 26.9 | H II | 9.2 | 52 \times 30 |
| NGC 4631 | 12 42 07.80 | +32 32 34.6 | H II | 8.1 | 52 \times 30 |
| NGC 5713 | 14 40 11.38 | -00 17 24.2 | H II | 29.4 | 52 \times 30 |
| NGC 6946 | 20 34 52.23 | +60 09 14.4 | H II | 6.8 | 52 \times 30 |
| NGC 7793 | 23 57 49.84 | -32 35 27.1 | H II | 3.8 | 52 \times 30 |
| NGC 1097 | 02 46 18.86 | -30 16 27.2 | LINER | 17.1 | 52 \times 30 |
| NGC 1266 | 03 16 00.71 | -02 25 36.9 | LINER | 30.0 | 52 \times 30 |
| NGC 1512 | 04 03 54.17 | -43 20 54.4 | LINER | 11.8 | 52 \times 30 |
| NGC 1566 | 04 20 00.33 | -54 56 16.6 | Seyfert | 20.3 | 52 \times 30 |
| NGC 3198 | 10 19 54.84 | +45 32 58.7 | LINER | 13.7 | 52 \times 30 |
| NGC 3521 | 11 05 48.58 | -00 02 07.3 | LINER | 10.1 | 52 \times 30 |
| NGC 3621 | 11 18 16.51 | -32 48 49.3 | LINER | 6.6 | 52 \times 30 |
| NGC 3627 | 11 20 15.04 | +12 59 29.0 | Seyfert | 9.4 | 52 \times 30 |
| NGC 3938 | 11 52 49.32 | +44 07 13.6 | LINER | 13.3 | 52 \times 30 |
| NGC 4321 | 12 22 54.87 | +15 49 19.2 | LINER | 14.3 | 52 \times 30 |
| NGC 4450 | 12 28 29.71 | +17 05 08.7 | LINER | 16.6 | 52 \times 30 |
| NGC 4569 | 12 36 49.76 | +13 09 45.5 | Seyfert | 16.6 | 52 \times 30 |
| NGC 4579 | 12 37 43.53 | +11 49 03.8 | Seyfert | 16.6 | 52 \times 30 |
| NGC 4736 | 12 50 53.15 | +41 07 14.4 | LINER | 5.0 | 52 \times 30 |
| NGC 4826 | 12 56 43.59 | +21 40 58.0 | Seyfert | 5.0 | 52 \times 30 |
| NGC 5033 | 13 13 27.32 | +36 35 35.2 | Seyfert | 14.8 | 52 \times 30 |
| NGC 5055 | 13 15 49.35 | +42 01 45.7 | LINER | 7.8 | 52 \times 30 |
| NGC 5194 | 13 29 52.80 | +47 11 43.5 | Seyfert | 7.8 | 52 \times 30 |
| NGC 5195 | 13 29 59.50 | +47 15 56.7 | Seyfert | 8.0 | 52 \times 30 |
| NGC 5866 | 15 06 29.48 | +55 45 45.0 | LINER | 15.1 | 52 \times 30 |
| NGC 7331 | 22 37 04.15 | +34 24 55.3 | LINER | 14.5 | 52 \times 15 |
| NGC 7552 | 23 16 10.83 | -42 35 05.5 | LINER | 21.0 | 52 \times 30 |

Table 3. Basic Parameters for Quasars and Obscured Galaxies

| Source | R.A. (J2000) (hh mm ss.s) | Decl. (J2000) (dd mm ss.s) | Type | Distance (Mpc) |
|------------------|------------------------------|-------------------------------|---------------|-------------------|
| (1) | (2) | (3) | (4) | (5) |
| Arp 220 | 15 34 57.23 | +23 30 11.3 | AGN+starburst | 78.6 |
| PG 1244+026 | 12 46 35.25 | +02 22 08.8 | Quasar | 213.1 |
| PG 1351+236 | 13 54 06.43 | +23 25 49.1 | Quasar | 245.4 |
| PG 1617+175 | 16 20 11.29 | +17 24 27.7 | Quasar | 529.6 |
| IRAS F01364-1042 | 01 38 52.79 | -10 27 12.1 | AGN+starburst | 213.1 |
| IRAS F08572+3915 | 09 00 25.35 | +39 03 54.0 | AGN+starburst | 261.2 |

Table 4. PAH Fluxes Measured from Current Method

| Source | PAH (6.2 μm) ($\text{erg s}^{-1}\text{cm}^{-2}$) | Err (6.2 μm) ($\text{erg s}^{-1}\text{cm}^{-2}$) | PAH (7.7 μm) ($\text{erg s}^{-1}\text{cm}^{-2}$) | Err (7.7 μm) ($\text{erg s}^{-1}\text{cm}^{-2}$) | PAH (8.6 μm) ($\text{erg s}^{-1}\text{cm}^{-2}$) | Err (8.6 μm) ($\text{erg s}^{-1}\text{cm}^{-2}$) | PAH (11.3 μm) ($\text{erg s}^{-1}\text{cm}^{-2}$) | Err (11.3 μm) ($\text{erg s}^{-1}\text{cm}^{-2}$) |
|---------------------|---|---|---|---|---|---|--|--|
| (1) | (2) | (3) | (4) | (5) | (6) | (7) | (8) | (9) |
| Mrk 33..... | 3.26E-12 | 1.11E-12 | 1.19E-11 | 5.74E-12 | 3.37E-12 | 2.75E-12 | 3.57E-12 | 1.20E-12 |
| NGC 24..... | 7.17E-13 | 9.56E-14 | 2.52E-12 | 5.66E-13 | 6.80E-13 | 1.72E-13 | 1.05E-12 | 6.88E-14 |
| NGC 337..... | 5.78E-12 | 8.24E-14 | 2.06E-11 | 5.61E-13 | 5.20E-12 | 1.19E-13 | 5.57E-12 | 4.88E-14 |
| NGC 628..... | 2.61E-12 | 7.57E-14 | 1.09E-11 | 4.79E-13 | 3.36E-12 | 1.21E-13 | 3.10E-12 | 1.04E-12 |
| NGC 855..... | 6.21E-13 | 1.76E-13 | 2.32E-12 | 7.30E-13 | 1.06E-12 | 2.48E-13 | 1.19E-12 | 7.75E-14 |
| NGC 925..... | 2.00E-12 | 8.63E-14 | 7.33E-12 | 5.51E-13 | 2.14E-12 | 1.40E-13 | 2.06E-12 | 5.77E-14 |
| NGC 1482..... | 4.16E-11 | 1.34E-13 | 1.78E-10 | 7.70E-13 | 5.61E-11 | 2.80E-13 | 4.50E-11 | 1.83E-13 |
| NGC 2403..... | 4.50E-12 | 7.90E-14 | 1.41E-11 | 4.68E-13 | 4.54E-12 | 1.42E-13 | 4.23E-12 | 5.72E-14 |
| NGC 2798..... | 1.59E-11 | 1.85E-13 | 6.46E-11 | 1.10E-12 | 2.03E-11 | 4.49E-13 | 1.85E-11 | 3.60E-13 |
| NGC 2915..... | - | - | 1.12E-12 | 2.33E-13 | 3.78E-13 | 1.49E-13 | 2.00E-13 | 5.86E-14 |
| NGC 2976..... | 2.85E-12 | 7.56E-14 | 1.11E-11 | 4.89E-13 | 2.86E-12 | 1.32E-13 | 3.53E-12 | 5.52E-14 |
| NGC 3049..... | 2.45E-12 | 7.26E-14 | 1.02E-11 | 4.88E-13 | 2.29E-12 | 1.32E-13 | 2.49E-12 | 5.70E-14 |
| NGC 3184..... | 2.23E-13 | 9.66E-14 | 7.86E-12 | 2.41E-13 | 3.14E-12 | 1.47E-13 | 2.15E-12 | 6.20E-14 |
| NGC 3265..... | 2.88E-12 | 9.22E-14 | 1.14E-11 | 5.97E-13 | 3.28E-12 | 1.55E-13 | 3.11E-12 | 6.78E-14 |
| NGC 3351..... | 1.29E-11 | 8.06E-14 | 5.47E-11 | 5.41E-13 | 1.25E-11 | 1.46E-13 | 1.26E-11 | 6.10E-14 |
| NGC 3773..... | 1.08E-12 | 8.31E-14 | 4.30E-12 | 5.00E-13 | 1.09E-12 | 1.56E-13 | 1.27E-12 | 6.51E-14 |
| NGC 4254..... | 1.48E-11 | 7.68E-14 | 6.14E-11 | 5.43E-13 | 1.60E-11 | 1.45E-13 | 1.68E-11 | 6.13E-14 |
| NGC 4536..... | 2.94E-11 | 2.10E-13 | 1.19E-10 | 1.18E-12 | 3.59E-11 | 4.52E-13 | 3.17E-11 | 3.35E-13 |
| NGC 4559..... | 4.32E-12 | 8.01E-14 | 1.64E-11 | 5.30E-13 | 4.25E-12 | 1.50E-13 | 4.23E-12 | 5.96E-14 |
| NGC 4625..... | 1.67E-12 | 7.32E-14 | 7.84E-12 | 4.49E-13 | 2.13E-12 | 1.37E-13 | 2.19E-12 | 5.71E-14 |
| NGC 4631..... | 2.63E-11 | 1.35E-12 | 1.04E-10 | 7.46E-12 | 3.13E-11 | 3.14E-12 | 2.74E-11 | 2.36E-12 |
| NGC 5713..... | 1.97E-11 | 7.99E-14 | 7.85E-11 | 5.02E-13 | 2.09E-11 | 1.34E-13 | 1.96E-11 | 5.42E-14 |
| NGC 6946..... | 5.17E-11 | 1.69E-13 | 2.13E-10 | 9.60E-13 | 7.22E-11 | 4.12E-13 | 5.70E-11 | 2.77E-13 |
| NGC 7793..... | 2.59E-12 | 7.63E-14 | 1.47E-11 | 4.79E-13 | 2.71E-12 | 1.28E-13 | 3.36E-12 | 5.04E-14 |
| NGC 1097..... | 3.92E-11 | 7.17E-14 | 1.71E-10 | 4.48E-13 | 4.60E-11 | 1.29E-13 | 4.46E-11 | 5.66E-14 |
| NGC 1266..... | 2.34E-12 | 1.07E-13 | 1.21E-11 | 7.49E-13 | 5.27E-12 | 3.23E-13 | 4.06E-12 | 1.80E-13 |
| NGC 1512..... | 3.24E-12 | 8.55E-14 | 1.41E-11 | 5.18E-13 | 3.33E-12 | 1.55E-13 | 3.43E-12 | 6.12E-14 |
| NGC 1566..... | 4.71E-12 | 7.17E-14 | 2.23E-11 | 4.64E-13 | 5.20E-12 | 1.24E-13 | 6.38E-12 | 5.43E-14 |
| NGC 3198..... | 3.80E-12 | 1.09E-13 | 1.57E-11 | 6.98E-13 | 7.92E-12 | 3.50E-13 | 6.61E-12 | 1.70E-13 |
| NGC 3521..... | 1.45E-11 | 1.23E-13 | 5.82E-11 | 6.80E-13 | 1.51E-11 | 2.51E-13 | 1.72E-11 | 1.02E-13 |
| NGC 3621..... | 7.01E-12 | 8.08E-14 | 3.53E-11 | 5.28E-13 | 9.92E-12 | 1.48E-13 | 9.02E-12 | 6.04E-14 |
| NGC 3627..... | 9.45E-12 | 9.47E-14 | 4.34E-11 | 5.90E-13 | 1.27E-11 | 1.52E-13 | 1.53E-11 | 6.22E-14 |
| NGC 3938..... | 2.02E-12 | 6.94E-14 | 6.74E-12 | 4.69E-13 | 2.79E-12 | 1.43E-13 | 2.94E-12 | 6.37E-14 |
| NGC 4321..... | 1.42E-11 | 7.91E-14 | 6.89E-11 | 5.10E-13 | 1.72E-11 | 1.46E-13 | 1.58E-11 | 6.35E-14 |
| NGC 4450..... | 1.29E-13 | 9.60E-14 | 2.30E-12 | 5.07E-13 | 1.05E-12 | 1.09E-13 | 1.40E-12 | 6.27E-14 |
| NGC 4569..... | 6.13E-12 | 8.24E-14 | 2.07E-11 | 4.94E-13 | 7.62E-12 | 1.54E-13 | 1.07E-11 | 6.37E-14 |
| NGC 4579..... | 1.08E-12 | 2.46E-13 | 2.41E-12 | 7.50E-13 | - | - | 1.53E-12 | 3.61E-13 |
| NGC 4736..... | 1.87E-11 | 7.99E-14 | 7.80E-11 | 4.99E-13 | 2.55E-11 | 1.41E-13 | 3.53E-11 | 6.36E-14 |
| NGC 4826..... | 2.24E-11 | 8.12E-14 | 1.01E-10 | 5.01E-13 | 2.70E-11 | 1.54E-13 | 2.66E-11 | 6.14E-14 |
| NGC 5033..... | 1.32E-11 | 8.47E-14 | 5.19E-11 | 5.33E-13 | 1.46E-11 | 1.56E-13 | 1.52E-11 | 6.32E-14 |
| NGC 5055..... | 1.22E-11 | 7.91E-14 | 5.57E-11 | 5.03E-13 | 1.41E-11 | 1.37E-13 | 1.56E-11 | 5.63E-14 |
| NGC 5194..... | 1.80E-11 | 7.44E-14 | 7.44E-11 | 4.70E-13 | 2.08E-11 | 1.48E-13 | 2.25E-11 | 6.29E-14 |
| NGC 5195..... | 8.96E-12 | 9.33E-14 | 3.74E-11 | 5.31E-13 | 1.04E-11 | 1.69E-13 | 1.75E-11 | 7.13E-14 |
| NGC 5866..... | 1.68E-12 | 1.95E-13 | 9.40E-12 | 6.95E-13 | 2.13E-12 | 2.14E-13 | 2.73E-12 | 7.36E-14 |
| NGC 7331..... | 3.83E-12 | 9.97E-14 | 1.45E-11 | 5.58E-13 | 3.91E-12 | 1.70E-13 | 5.47E-12 | 6.41E-14 |
| NGC 7552..... | 4.32E-11 | 4.70E-13 | 1.84E-10 | 2.87E-12 | 6.02E-11 | 1.29E-12 | 5.27E-11 | 1.06E-12 |
| DCld 300.2-16.9 (A) | 6.13E-13 | 1.37E-14 | 2.62E-12 | 5.93E-14 | 7.52E-13 | 1.67E-14 | 8.33E-13 | 9.28E-15 |
| DCld 300.2-16.9 (B) | 8.95E-13 | 1.34E-14 | 3.29E-12 | 6.07E-14 | 1.05E-12 | 1.65E-14 | 1.13E-12 | 9.10E-15 |
| DCld 300.2-16.9 (C) | 8.54E-13 | 1.24E-14 | 2.81E-12 | 5.91E-14 | 9.35E-13 | 1.67E-14 | 1.02E-12 | 9.39E-15 |

Table 4—Continued

| Source | PAH (6.2 μm) ($\text{erg s}^{-1}\text{cm}^{-2}$) | Err (6.2 μm) ($\text{erg s}^{-1}\text{cm}^{-2}$) | PAH (7.7 μm) ($\text{erg s}^{-1}\text{cm}^{-2}$) | Err (7.7 μm) ($\text{erg s}^{-1}\text{cm}^{-2}$) | PAH (8.6 μm) ($\text{erg s}^{-1}\text{cm}^{-2}$) | Err (8.6 μm) ($\text{erg s}^{-1}\text{cm}^{-2}$) | PAH (11.3 μm) ($\text{erg s}^{-1}\text{cm}^{-2}$) | Err (11.3 μm) ($\text{erg s}^{-1}\text{cm}^{-2}$) |
|---------------------|---|---|---|---|---|---|--|--|
| (1) | (2) | (3) | (4) | (5) | (6) | (7) | (8) | (9) |
| DCld 300.2-16.9 (D) | 5.45E-13 | 1.28E-14 | 1.69E-12 | 5.99E-14 | 6.47E-13 | 1.65E-14 | 6.23E-13 | 9.54E-15 |

Table 5. PAH Fluxes Measured from PAHFIT

| Source | PAH (6.2 μm) (erg s ⁻¹ cm ⁻²) | Err (6.2 μm) (erg s ⁻¹ cm ⁻²) | PAH (7.7 μm) (erg s ⁻¹ cm ⁻²) | Err (7.7 μm) (erg s ⁻¹ cm ⁻²) | PAH (8.6 μm) (erg s ⁻¹ cm ⁻²) | Err (8.6 μm) (erg s ⁻¹ cm ⁻²) | PAH (11.3 μm) (erg s ⁻¹ cm ⁻²) | Err (11.3 μm) (erg s ⁻¹ cm ⁻²) |
|---------------------|---|---|---|---|---|---|--|--|
| (1) | (2) | (3) | (4) | (5) | (6) | (7) | (8) | (9) |
| Mrk 33..... | 3.44E-12 | 8.56E-14 | 1.17E-11 | 4.89E-13 | 3.21E-12 | 1.06E-13 | 3.15E-12 | 4.44E-14 |
| NGC 24..... | 8.85E-13 | 9.97E-14 | 2.52E-12 | 5.09E-13 | 7.15E-13 | 1.42E-13 | 9.83E-13 | 6.21E-14 |
| NGC 337..... | 6.08E-12 | 8.10E-14 | 1.65E-11 | 5.60E-13 | 4.84E-12 | 1.15E-13 | 5.31E-12 | 5.66E-14 |
| NGC 628..... | 2.53E-12 | 7.75E-14 | 9.75E-12 | 4.99E-13 | 2.99E-12 | 1.14E-13 | 2.48E-12 | 5.16E-14 |
| NGC 855..... | 9.09E-13 | 7.58E-14 | 2.10E-12 | 2.43E-13 | 1.04E-12 | 1.32E-13 | 1.11E-12 | 6.27E-14 |
| NGC 925..... | 2.38E-12 | 9.33E-14 | 7.34E-12 | 5.39E-13 | 2.24E-12 | 1.27E-13 | 1.95E-12 | 5.49E-14 |
| NGC 1482..... | 4.22E-11 | 1.27E-13 | 1.63E-10 | 5.23E-13 | 4.32E-11 | 1.49E-13 | 3.33E-11 | 9.29E-14 |
| NGC 2403..... | 4.98E-12 | 7.73E-14 | 1.26E-11 | 4.58E-13 | 4.18E-12 | 1.41E-13 | 4.06E-12 | 6.58E-14 |
| NGC 2798..... | 1.67E-11 | 9.94E-14 | 6.01E-11 | 6.28E-13 | 1.67E-11 | 1.37E-13 | 1.42E-11 | 6.05E-14 |
| NGC 2915..... | 9.58E-14 | 9.04E-14 | 2.03E-12 | 4.79E-13 | 7.91E-13 | 1.35E-13 | 3.73E-13 | 5.37E-14 |
| NGC 2976..... | 2.83E-12 | 7.38E-14 | 9.63E-12 | 4.78E-13 | 2.61E-12 | 1.25E-13 | 3.30E-12 | 5.12E-14 |
| NGC 3049..... | 2.56E-12 | 6.72E-14 | 8.47E-12 | 4.69E-13 | 2.12E-12 | 1.18E-13 | 2.18E-12 | 5.28E-14 |
| NGC 3184..... | 2.25E-13 | 1.05E-13 | 7.60E-12 | 2.57E-13 | 2.91E-12 | 1.42E-13 | 2.00E-12 | 6.32E-14 |
| NGC 3265..... | 2.94E-12 | 1.03E-13 | 8.81E-12 | 5.96E-13 | 3.01E-12 | 1.45E-13 | 2.72E-12 | 6.44E-14 |
| NGC 3351..... | 1.29E-11 | 9.53E-14 | 4.65E-11 | 5.76E-13 | 1.08E-11 | 1.39E-13 | 1.11E-11 | 6.39E-14 |
| NGC 3773..... | 1.15E-12 | 1.18E-13 | 4.23E-12 | 6.54E-13 | 1.16E-12 | 1.49E-13 | 1.19E-12 | 6.20E-14 |
| NGC 4254..... | 1.53E-11 | 7.68E-14 | 5.04E-11 | 5.68E-13 | 1.39E-11 | 1.40E-13 | 1.60E-11 | 7.30E-14 |
| NGC 4536..... | 3.15E-11 | 1.24E-13 | 1.06E-10 | 6.29E-13 | 2.91E-11 | 1.66E-13 | 2.68E-11 | 9.51E-14 |
| NGC 4559..... | 4.43E-12 | 8.39E-14 | 1.33E-11 | 5.52E-13 | 3.73E-12 | 1.58E-13 | 4.01E-12 | 7.42E-14 |
| NGC 4625..... | 1.78E-12 | 7.23E-14 | 6.38E-12 | 4.45E-13 | 1.92E-12 | 1.38E-13 | 2.08E-12 | 6.61E-14 |
| NGC 4631..... | 2.92E-11 | 9.15E-14 | 9.71E-11 | 5.95E-13 | 2.62E-11 | 1.59E-13 | 2.30E-11 | 8.39E-14 |
| NGC 5713..... | 2.04E-11 | 1.05E-13 | 6.81E-11 | 6.02E-13 | 1.91E-11 | 1.35E-13 | 1.72E-11 | 5.69E-14 |
| NGC 6946..... | 5.14E-11 | 1.26E-13 | 1.92E-10 | 7.39E-13 | 5.91E-11 | 1.97E-13 | 4.46E-11 | 1.10E-13 |
| NGC 7793..... | 2.73E-12 | 7.23E-14 | 1.26E-11 | 4.82E-13 | 2.34E-12 | 1.16E-13 | 3.01E-12 | 4.57E-14 |
| NGC 1097..... | 4.03E-11 | 8.98E-14 | 1.51E-10 | 4.90E-13 | 4.20E-11 | 1.24E-13 | 3.81E-11 | 5.53E-14 |
| NGC 1266..... | 1.82E-12 | 1.55E-13 | 1.12E-11 | 6.83E-13 | 2.73E-12 | 1.88E-13 | 2.72E-12 | 8.95E-14 |
| NGC 1512..... | 3.66E-12 | 9.38E-14 | 1.28E-11 | 5.12E-13 | 3.06E-12 | 1.40E-13 | 2.98E-12 | 5.76E-14 |
| NGC 1566..... | 4.57E-12 | 7.60E-14 | 1.94E-11 | 4.85E-13 | 4.59E-12 | 1.06E-13 | 5.47E-12 | 4.51E-14 |
| NGC 3198..... | 4.32E-12 | 1.18E-13 | 1.52E-11 | 7.04E-13 | 3.48E-12 | 1.32E-13 | 4.69E-12 | 1.25E-13 |
| NGC 3521..... | 1.38E-11 | 9.61E-14 | 4.81E-11 | 5.10E-13 | 1.22E-11 | 1.35E-13 | 1.59E-11 | 6.12E-14 |
| NGC 3621..... | 7.34E-12 | 8.24E-14 | 2.90E-11 | 5.49E-13 | 8.72E-12 | 1.54E-13 | 8.22E-12 | 7.47E-14 |
| NGC 3627..... | 8.60E-12 | 1.09E-13 | 3.49E-11 | 5.96E-13 | 1.14E-11 | 1.26E-13 | 1.34E-11 | 5.35E-14 |
| NGC 3938..... | 2.05E-12 | 7.73E-14 | 6.60E-12 | 2.00E-13 | 2.94E-12 | 1.34E-13 | 2.92E-12 | 5.92E-14 |
| NGC 4321..... | 1.47E-11 | 8.54E-14 | 5.93E-11 | 5.57E-13 | 1.57E-11 | 1.57E-13 | 1.45E-11 | 8.16E-14 |
| NGC 4450..... | 4.20E-13 | 9.69E-14 | 2.28E-12 | 2.35E-13 | 9.41E-13 | 9.24E-14 | 1.25E-12 | 5.62E-14 |
| NGC 4569..... | 5.10E-12 | 1.09E-13 | 1.68E-11 | 2.42E-13 | 6.68E-12 | 1.20E-13 | 9.93E-12 | 5.03E-14 |
| NGC 4579..... | 1.76E-12 | 7.83E-14 | 5.36E-12 | 2.99E-13 | 2.17E-13 | 6.43E-14 | 1.60E-12 | 4.26E-14 |
| NGC 4736..... | 1.42E-11 | 1.16E-13 | 4.60E-11 | 5.05E-13 | 1.81E-11 | 1.41E-13 | 3.32E-11 | 6.03E-14 |
| NGC 4826..... | 2.26E-11 | 9.47E-14 | 8.69E-11 | 5.19E-13 | 2.44E-11 | 1.46E-13 | 2.38E-11 | 6.73E-14 |
| NGC 5033..... | 1.33E-11 | 9.08E-14 | 4.45E-11 | 5.16E-13 | 1.31E-11 | 1.41E-13 | 1.37E-11 | 6.00E-14 |
| NGC 5055..... | 1.25E-11 | 1.01E-13 | 4.88E-11 | 5.37E-13 | 1.31E-11 | 1.28E-13 | 1.49E-11 | 5.45E-14 |
| NGC 5194..... | 1.80E-11 | 9.65E-14 | 6.46E-11 | 4.94E-13 | 1.85E-11 | 1.43E-13 | 2.09E-11 | 6.57E-14 |
| NGC 5195..... | 8.85E-12 | 8.45E-14 | 3.55E-11 | 5.00E-13 | 9.88E-12 | 1.38E-13 | 1.69E-11 | 6.15E-14 |
| NGC 5866..... | 1.37E-12 | 9.03E-14 | 6.79E-12 | 4.79E-13 | 1.47E-12 | 1.36E-13 | 2.58E-12 | 6.02E-14 |
| NGC 7331..... | 3.66E-12 | 8.21E-14 | 1.25E-11 | 4.90E-13 | 3.26E-12 | 1.28E-13 | 4.88E-12 | 5.12E-14 |
| NGC 7552..... | 4.43E-11 | 1.27E-13 | 1.70E-10 | 7.21E-13 | 5.16E-11 | 1.71E-13 | 4.22E-11 | 9.81E-14 |
| DCld 300.2-16.9 (A) | 7.50E-13 | 1.53E-14 | 2.69E-12 | 8.09E-14 | 7.43E-13 | 1.67E-14 | 7.95E-13 | 1.08E-14 |
| DCld 300.2-16.9 (B) | 1.03E-12 | 1.54E-14 | 2.95E-12 | 6.64E-14 | 9.63E-13 | 1.47E-14 | 1.05E-12 | 9.55E-15 |
| DCld 300.2-16.9 (C) | 9.02E-13 | 1.50E-14 | 2.42E-12 | 2.83E-14 | 8.26E-13 | 1.58E-14 | 9.45E-13 | 9.99E-15 |

Table 5—Continued

| Source | PAH (6.2 μm) ($\text{erg s}^{-1}\text{cm}^{-2}$) | Err (6.2 μm) ($\text{erg s}^{-1}\text{cm}^{-2}$) | PAH (7.7 μm) ($\text{erg s}^{-1}\text{cm}^{-2}$) | Err (7.7 μm) ($\text{erg s}^{-1}\text{cm}^{-2}$) | PAH (8.6 μm) ($\text{erg s}^{-1}\text{cm}^{-2}$) | Err (8.6 μm) ($\text{erg s}^{-1}\text{cm}^{-2}$) | PAH (11.3 μm) ($\text{erg s}^{-1}\text{cm}^{-2}$) | Err (11.3 μm) ($\text{erg s}^{-1}\text{cm}^{-2}$) |
|---------------------|---|---|---|---|---|---|--|--|
| (1) | (2) | (3) | (4) | (5) | (6) | (7) | (8) | (9) |
| DCld 300.2-16.9 (D) | 6.31E-13 | 1.53E-14 | 1.65E-12 | 2.56E-14 | 6.02E-13 | 1.51E-14 | 5.65E-13 | 9.87E-15 |

Table 6. PAH Fluxes Measured from Spline Technique

| Source (1) | PAH (6.2 μm) ($\text{erg s}^{-1}\text{cm}^{-2}$) (2) | lower limit (3) | upper limit (4) | PAH (7.7 μm) ($\text{erg s}^{-1}\text{cm}^{-2}$) (5) | lower limit (6) | upper limit (7) | PAH (8.6 μm) ($\text{erg s}^{-1}\text{cm}^{-2}$) (8) | lower limit (9) | upper limit (10) | PAH (11.3 μm) ($\text{erg s}^{-1}\text{cm}^{-2}$) (11) | lower limit (12) | upper limit (13) |
|---------------------|--|-----------------------|-----------------------|--|-----------------------|-----------------------|--|-----------------------|------------------------|--|------------------------|------------------------|
| Mrk 33 | 2.38E-12 | 2.14E-12 | 2.83E-12 | 4.24E-12 | 3.00E-12 | 4.74E-12 | 1.02E-12 | 9.27E-13 | 1.09E-12 | 1.78E-12 | 1.72E-12 | 1.85E-12 |
| NGC 24 | 4.38E-13 | 4.37E-13 | 6.21E-13 | 1.02E-12 | 8.01E-13 | 1.35E-12 | 2.28E-13 | 2.12E-13 | 3.58E-13 | 4.97E-13 | 4.95E-13 | 5.61E-13 |
| NGC 337 | 3.95E-12 | 3.66E-12 | 4.37E-12 | 6.02E-12 | 5.81E-12 | 7.70E-12 | 1.60E-12 | 1.30E-12 | 1.82E-12 | 3.00E-12 | 2.83E-12 | 3.11E-12 |
| NGC 628 | 2.01E-12 | 1.73E-12 | 2.47E-12 | 2.22E-12 | 1.37E-12 | 3.10E-12 | 5.10E-13 | 3.04E-13 | 6.18E-13 | 1.38E-12 | 1.36E-12 | 1.45E-12 |
| NGC 855 | < 8.52E-13 | - | - | 8.63E-13 | 7.53E-13 | 1.39E-12 | < 3.42E-13 | - | - | 6.82E-13 | 6.49E-13 | 8.92E-13 |
| NGC 925 | 1.20E-12 | 9.70E-13 | 1.45E-12 | 2.78E-12 | 2.42E-12 | 3.16E-12 | 5.05E-13 | 2.72E-13 | 5.60E-13 | 1.01E-12 | 8.96E-13 | 1.11E-12 |
| NGC 1482 | 2.68E-11 | 2.32E-11 | 2.80E-11 | 4.87E-11 | 4.74E-11 | 5.70E-11 | 8.86E-12 | 7.60E-12 | 1.11E-11 | 1.69E-11 | 1.62E-11 | 1.74E-11 |
| NGC 2403 | 3.40E-12 | 2.69E-12 | 3.73E-12 | 2.19E-12 | 1.68E-12 | 3.90E-12 | 5.97E-13 | 5.63E-13 | 1.05E-12 | 2.11E-12 | 2.02E-12 | 2.29E-12 |
| NGC 2798 | 9.93E-12 | 9.05E-12 | 1.07E-11 | 1.94E-11 | 1.79E-11 | 2.24E-11 | 4.09E-12 | 3.36E-12 | 4.50E-12 | 7.69E-12 | 7.30E-12 | 7.85E-12 |
| NGC 2915 | < 4.02E-13 | - | - | < 1.45E-12 | - | - | < 2.12E-13 | - | - | < 2.99E-13 | - | - |
| NGC 2976 | 1.91E-12 | 1.75E-12 | 2.08E-12 | 4.32E-12 | 2.98E-12 | 4.94E-12 | 1.09E-12 | 1.07E-12 | 1.40E-12 | 2.01E-12 | 1.86E-12 | 2.02E-12 |
| NGC 3049 | 1.82E-12 | 1.72E-12 | 1.95E-12 | 3.00E-12 | 2.75E-12 | 3.41E-12 | 7.06E-13 | 6.03E-13 | 8.52E-13 | 1.14E-12 | 1.10E-12 | 1.32E-12 |
| NGC 3184 | < 7.44E-13 | - | - | 3.38E-12 | 2.97E-13 | 3.93E-12 | 2.51E-13 | 1.69E-13 | 6.38E-13 | 9.88E-13 | 9.60E-13 | 1.19E-12 |
| NGC 3265 | 2.02E-12 | 1.92E-12 | 2.45E-12 | 3.54E-12 | 2.61E-12 | 3.72E-12 | 9.18E-13 | 8.14E-13 | 9.75E-13 | 1.68E-12 | 1.59E-12 | 1.78E-12 |
| NGC 3351 | 9.03E-12 | 8.54E-12 | 9.41E-12 | 1.09E-11 | 1.05E-11 | 1.53E-11 | 1.89E-12 | 1.87E-12 | 3.13E-12 | 6.12E-12 | 6.08E-12 | 6.36E-12 |
| NGC 3773 | 6.16E-13 | 4.42E-13 | 1.36E-12 | 1.22E-12 | 7.11E-13 | 1.83E-12 | 2.67E-13 | 2.51E-13 | 2.69E-13 | 7.62E-13 | 7.41E-13 | 9.11E-13 |
| NGC 4254 | 1.13E-11 | 9.75E-12 | 1.22E-11 | 1.93E-11 | 1.82E-11 | 2.07E-11 | 2.88E-12 | 2.21E-12 | 4.24E-12 | 8.40E-12 | 7.71E-12 | 8.84E-12 |
| NGC 4536 | 1.94E-11 | 1.72E-11 | 2.06E-11 | 3.63E-11 | 3.24E-11 | 3.99E-11 | 5.27E-12 | 4.33E-12 | 7.58E-12 | 1.31E-11 | 1.22E-11 | 1.34E-11 |
| NGC 4559 | 3.23E-12 | 2.64E-12 | 3.29E-12 | 4.40E-12 | 3.92E-12 | 5.60E-12 | 8.67E-13 | 7.82E-13 | 1.13E-12 | 2.02E-12 | 1.97E-12 | 2.44E-12 |
| NGC 4625 | 1.18E-12 | 9.86E-13 | 1.36E-12 | 2.43E-12 | 1.66E-12 | 2.98E-12 | 4.86E-13 | 3.75E-13 | 5.92E-13 | 1.11E-12 | 1.05E-12 | 1.27E-12 |
| NGC 4631 | 1.81E-11 | 1.60E-11 | 1.92E-11 | 3.09E-11 | 2.40E-11 | 3.62E-11 | 5.92E-12 | 5.32E-12 | 7.48E-12 | 1.19E-11 | 1.13E-11 | 1.22E-11 |
| NGC 5713 | 1.26E-11 | 1.11E-11 | 1.33E-11 | 2.38E-11 | 2.17E-11 | 2.59E-11 | 4.15E-12 | 3.75E-12 | 5.95E-12 | 1.00E-11 | 9.21E-12 | 1.05E-11 |
| NGC 6946 | 2.88E-11 | 2.72E-11 | 3.21E-11 | 5.49E-11 | 4.82E-11 | 6.69E-11 | 6.71E-12 | 6.42E-12 | 1.41E-11 | 2.15E-11 | 2.02E-11 | 2.18E-11 |
| NGC 7793 | 1.86E-12 | 1.39E-12 | 2.07E-12 | 3.08E-12 | 2.66E-12 | 3.75E-12 | 6.21E-13 | 4.25E-13 | 6.33E-13 | 1.92E-12 | 1.66E-12 | 1.98E-12 |
| NGC 1097 | 2.75E-11 | 2.36E-11 | 2.77E-11 | 4.56E-11 | 4.39E-11 | 5.20E-11 | 9.06E-12 | 8.73E-12 | 1.18E-11 | 2.15E-11 | 2.05E-11 | 2.23E-11 |
| NGC 1266 | 9.56E-13 | 8.73E-13 | 1.05E-12 | 1.91E-12 | 1.17E-12 | 2.72E-12 | 4.22E-13 | 3.32E-13 | 4.64E-13 | 9.64E-13 | 9.06E-13 | 1.01E-12 |
| NGC 1512 | 1.89E-12 | 1.86E-12 | 2.59E-12 | 2.92E-12 | 2.57E-12 | 3.97E-12 | 6.00E-13 | 2.15E-13 | 7.60E-13 | 1.69E-12 | 1.58E-12 | 1.77E-12 |
| NGC 1566 | 2.81E-12 | 2.41E-12 | 3.74E-12 | 5.47E-12 | 4.35E-12 | 6.99E-12 | 7.32E-13 | 6.69E-13 | 9.46E-13 | 3.05E-12 | 2.90E-12 | 3.30E-12 |
| NGC 3198 | 1.77E-12 | 1.57E-12 | 2.07E-12 | 5.56E-12 | 5.34E-12 | 6.64E-12 | 5.67E-13 | 4.95E-13 | 6.40E-13 | 1.85E-12 | 1.72E-12 | 2.02E-12 |
| NGC 3521 | 1.11E-11 | 1.01E-11 | 1.15E-11 | 1.43E-11 | 1.37E-11 | 1.79E-11 | 3.63E-12 | 3.27E-12 | 4.32E-12 | 8.23E-12 | 8.15E-12 | 8.67E-12 |
| NGC 3621 | 5.70E-12 | 5.14E-12 | 6.09E-12 | 9.49E-12 | 8.14E-12 | 1.01E-11 | 2.01E-12 | 1.31E-12 | 2.24E-12 | 4.83E-12 | 4.69E-12 | 5.11E-12 |
| NGC 3627 | 6.15E-12 | 5.89E-12 | 6.58E-12 | 8.58E-12 | 6.54E-12 | 1.14E-11 | 2.11E-12 | 1.71E-12 | 3.08E-12 | 7.41E-12 | 7.12E-12 | 7.95E-12 |
| NGC 3938 | 1.83E-12 | 1.55E-12 | 2.77E-12 | 1.61E-12 | 1.31E-12 | 2.43E-12 | 3.58E-13 | 2.71E-13 | 6.24E-13 | 1.31E-12 | 1.30E-12 | 1.40E-12 |
| NGC 4321 | 1.02E-11 | 9.32E-12 | 1.04E-11 | 1.64E-11 | 1.54E-11 | 2.20E-11 | 3.53E-12 | 2.63E-12 | 4.25E-12 | 7.37E-12 | 7.20E-12 | 7.81E-12 |
| NGC 4450 | < 6.47E-13 | - | - | < 1.38E-12 | - | - | < 1.33E-12 | - | - | 8.16E-13 | 7.50E-13 | 8.73E-13 |
| NGC 4569 | 3.74E-12 | 2.95E-12 | 4.41E-12 | 7.52E-12 | 1.73E-12 | 9.42E-12 | 1.31E-12 | 1.26E-12 | 1.80E-12 | 5.54E-12 | 5.24E-12 | 5.73E-12 |
| NGC 4579 | 1.20E-12 | 9.76E-13 | 2.00E-12 | < 1.26E-12 | - | - | < 1.54E-13 | - | - | 8.39E-13 | 6.20E-13 | 8.68E-13 |
| NGC 4736 | 1.33E-11 | 1.07E-11 | 1.60E-11 | 1.37E-11 | 9.15E-12 | 1.46E-11 | 3.36E-12 | 2.93E-12 | 4.48E-12 | 1.86E-11 | 1.84E-11 | 1.94E-11 |
| NGC 4826 | 1.46E-11 | 1.40E-11 | 1.54E-11 | 3.00E-11 | 2.83E-11 | 3.46E-11 | 5.48E-12 | 5.43E-12 | 6.59E-12 | 1.24E-11 | 1.19E-11 | 1.34E-11 |
| NGC 5033 | 9.61E-12 | 8.06E-12 | 9.71E-12 | 1.32E-11 | 1.16E-11 | 1.69E-11 | 3.15E-12 | 2.87E-12 | 4.05E-12 | 7.84E-12 | 7.44E-12 | 8.09E-12 |
| NGC 5055 | 7.84E-12 | 7.07E-12 | 8.92E-12 | 1.26E-11 | 1.11E-11 | 1.62E-11 | 2.24E-12 | 2.03E-12 | 3.65E-12 | 8.08E-12 | 7.49E-12 | 8.20E-12 |
| NGC 5194 | 1.15E-11 | 1.05E-11 | 1.22E-11 | 1.86E-11 | 1.85E-11 | 2.43E-11 | 3.09E-12 | 2.34E-12 | 4.81E-12 | 1.13E-11 | 1.07E-11 | 1.18E-11 |
| NGC 5195 | 5.97E-12 | 4.95E-12 | 7.00E-12 | 6.93E-12 | 6.44E-12 | 9.53E-12 | 2.16E-12 | 1.26E-12 | 2.38E-12 | 8.77E-12 | 8.26E-12 | 9.16E-12 |
| NGC 5866 | 1.37E-12 | 8.44E-13 | 1.54E-12 | 2.07E-12 | 1.59E-12 | 2.49E-12 | 2.46E-13 | 2.09E-13 | 5.31E-13 | 1.45E-12 | 1.33E-12 | 1.52E-12 |
| NGC 7331 | 2.51E-12 | 1.76E-12 | 3.40E-12 | 3.19E-12 | 2.29E-12 | 4.18E-12 | 9.09E-13 | 6.96E-13 | 1.07E-12 | 2.59E-12 | 2.41E-12 | 2.80E-12 |
| NGC 7552 | 2.62E-11 | 2.52E-11 | 2.71E-11 | 4.87E-11 | 4.66E-11 | 6.19E-11 | 8.04E-12 | 5.84E-12 | 1.27E-11 | 2.23E-11 | 2.10E-11 | 2.23E-11 |
| DCld 300.2-16.9 (A) | 6.47E-13 | 5.76E-13 | 6.90E-13 | 1.32E-12 | 8.85E-13 | 1.54E-12 | 9.09E-14 | 7.81E-14 | 1.42E-13 | 4.20E-13 | 3.77E-13 | 4.97E-13 |
| DCld 300.2-16.9 (B) | 8.45E-13 | 8.04E-13 | 9.07E-13 | 1.31E-12 | 1.26E-12 | 1.54E-12 | 1.51E-13 | 1.25E-13 | 1.81E-13 | 5.29E-13 | 4.94E-13 | 5.92E-13 |
| DCld 300.2-16.9 (C) | 8.24E-13 | 7.49E-13 | 8.38E-13 | 1.46E-12 | 1.17E-12 | 3.06E-12 | 1.10E-13 | 9.73E-14 | 1.63E-13 | 4.46E-13 | 4.25E-13 | 4.76E-13 |

Table 6—Continued

| Source (1) | PAH (6.2 μm) ($\text{erg s}^{-1}\text{cm}^{-2}$) (2) | lower limit (3) | upper limit (4) | PAH (7.7 μm) ($\text{erg s}^{-1}\text{cm}^{-2}$) (5) | lower limit (6) | upper limit (7) | PAH (8.6 μm) ($\text{erg s}^{-1}\text{cm}^{-2}$) (8) | lower limit (9) | upper limit (10) | PAH (11.3 μm) ($\text{erg s}^{-1}\text{cm}^{-2}$) (11) | lower limit (12) | upper limit (13) |
|---------------------|--|-----------------------|-----------------------|--|-----------------------|-----------------------|--|-----------------------|------------------------|--|------------------------|------------------------|
| DCld 300.2-16.9 (D) | 5.50E-13 | 4.88E-13 | 5.54E-13 | 1.55E-12 | 7.93E-13 | 1.69E-12 | 9.42E-14 | 7.67E-14 | 1.51E-13 | 2.77E-13 | 2.60E-13 | 3.25E-13 |

Table 7. PAH Fluxes Measured Using Template in CAFE

| Source | PAH (6.2 μm) ($\text{erg s}^{-1}\text{cm}^{-2}$) | Err (6.2 μm) ($\text{erg s}^{-1}\text{cm}^{-2}$) | PAH (7.7 μm) ($\text{erg s}^{-1}\text{cm}^{-2}$) | Err (7.7 μm) ($\text{erg s}^{-1}\text{cm}^{-2}$) | PAH (8.6 μm) ($\text{erg s}^{-1}\text{cm}^{-2}$) | Err (8.6 μm) ($\text{erg s}^{-1}\text{cm}^{-2}$) | PAH (11.3 μm) ($\text{erg s}^{-1}\text{cm}^{-2}$) | Err (11.3 μm) ($\text{erg s}^{-1}\text{cm}^{-2}$) |
|---------------------|---|---|---|---|---|---|--|--|
| (1) | (2) | (3) | (4) | (5) | (6) | (7) | (8) | (9) |
| Mrk 33..... | 2.74E-12 | 3.88E-12 | 8.79E-12 | 1.50E-11 | 2.80E-12 | 9.63E-12 | 3.25E-12 | 9.47E-12 |
| NGC 24..... | 6.98E-13 | 1.93E-13 | 1.65E-12 | 5.50E-13 | 5.85E-13 | 3.85E-13 | 1.01E-12 | 3.54E-13 |
| NGC 337..... | 5.61E-12 | 2.40E-13 | 1.55E-11 | 1.23E-12 | 4.60E-12 | 4.83E-13 | 5.43E-12 | 4.05E-13 |
| NGC 628..... | 2.23E-12 | 5.84E-13 | 8.31E-12 | 3.48E-12 | 2.84E-12 | 1.72E-12 | 2.37E-12 | 1.19E-12 |
| NGC 855..... | - | - | 9.75E-13 | 1.61E-12 | 5.86E-13 | 1.22E-12 | 1.10E-12 | 1.15E-12 |
| NGC 925..... | 2.00E-12 | 8.69E-14 | 6.04E-12 | 5.61E-13 | 1.79E-12 | 1.50E-13 | 1.86E-12 | 6.41E-14 |
| NGC 1482..... | 4.32E-11 | 1.08E-13 | 1.57E-10 | 6.32E-13 | 5.95E-11 | 2.37E-13 | 4.52E-11 | 1.36E-13 |
| NGC 2403..... | 4.37E-12 | 1.55E-13 | 1.07E-11 | 7.50E-13 | 4.15E-12 | 3.29E-13 | 4.32E-12 | 2.33E-13 |
| NGC 2798..... | 1.68E-11 | 9.05E-14 | 5.66E-11 | 6.08E-13 | 2.10E-11 | 2.15E-13 | 1.84E-11 | 1.41E-13 |
| NGC 2915..... | - | - | 1.24E-12 | 4.91E-13 | 4.49E-13 | 1.43E-13 | 2.39E-13 | 5.55E-14 |
| NGC 2976..... | 2.82E-12 | 7.49E-14 | 9.09E-12 | 4.87E-13 | 2.30E-12 | 1.31E-13 | 3.14E-12 | 5.61E-14 |
| NGC 3049..... | 2.35E-12 | 1.18E-13 | 8.10E-12 | 7.17E-13 | 2.11E-12 | 2.47E-13 | 2.43E-12 | 1.93E-13 |
| NGC 3184..... | 1.10E-13 | 9.53E-14 | 7.38E-12 | 2.40E-13 | 2.60E-12 | 1.46E-13 | 1.89E-12 | 6.41E-14 |
| NGC 3265..... | 2.64E-12 | 1.92E-13 | 7.92E-12 | 6.77E-13 | 2.85E-12 | 4.43E-13 | 2.79E-12 | 3.56E-13 |
| NGC 3351..... | 1.35E-11 | 1.18E-13 | 4.49E-11 | 7.23E-13 | 1.28E-11 | 2.57E-13 | 1.32E-11 | 1.77E-13 |
| NGC 3773..... | 1.07E-12 | 8.09E-14 | 3.55E-12 | 4.94E-13 | 8.76E-13 | 1.54E-13 | 1.13E-12 | 6.57E-14 |
| NGC 4254..... | 1.53E-11 | 1.16E-13 | 5.00E-11 | 7.39E-13 | 1.55E-11 | 2.65E-13 | 1.70E-11 | 1.99E-13 |
| NGC 4536..... | 3.08E-11 | 1.14E-13 | 1.01E-10 | 7.05E-13 | 3.72E-11 | 2.57E-13 | 3.22E-11 | 1.56E-13 |
| NGC 4559..... | 3.87E-12 | 1.97E-13 | 1.23E-11 | 1.05E-12 | 3.69E-12 | 4.23E-13 | 4.17E-12 | 3.28E-13 |
| NGC 4625..... | 1.09E-12 | 3.01E-13 | 5.65E-12 | 1.90E-12 | 1.73E-12 | 8.52E-13 | 2.02E-12 | 6.91E-13 |
| NGC 4631..... | 2.74E-11 | 1.25E-13 | 8.90E-11 | 7.13E-13 | 2.99E-11 | 2.70E-13 | 2.67E-11 | 1.70E-13 |
| NGC 5713..... | 2.03E-11 | 1.12E-13 | 6.40E-11 | 6.68E-13 | 2.21E-11 | 2.45E-13 | 2.11E-11 | 1.72E-13 |
| NGC 6946..... | 5.42E-11 | 1.09E-13 | 1.90E-10 | 6.67E-13 | 7.94E-11 | 2.92E-13 | 5.74E-11 | 1.66E-13 |
| NGC 7793..... | 2.45E-12 | 1.39E-13 | 1.17E-11 | 8.27E-13 | 2.31E-12 | 3.06E-13 | 3.22E-12 | 2.36E-13 |
| NGC 1097..... | 4.21E-11 | 1.01E-13 | 1.46E-10 | 6.15E-13 | 4.86E-11 | 2.36E-13 | 4.66E-11 | 1.65E-13 |
| NGC 1266..... | 2.15E-12 | 1.13E-13 | 9.33E-12 | 7.84E-13 | 5.27E-12 | 3.70E-13 | 4.03E-12 | 1.81E-13 |
| NGC 1512..... | 3.32E-12 | 1.15E-13 | 1.08E-11 | 6.72E-13 | 3.35E-12 | 2.53E-13 | 3.62E-12 | 1.56E-13 |
| NGC 1566..... | 5.18E-12 | 2.32E-13 | 1.89E-11 | 1.34E-12 | 4.29E-12 | 5.94E-13 | 6.02E-12 | 5.08E-13 |
| NGC 3198..... | 3.41E-12 | 1.13E-13 | 1.08E-11 | 7.30E-13 | 7.34E-12 | 3.99E-13 | 6.26E-12 | 1.88E-13 |
| NGC 3521..... | 1.45E-11 | 2.46E-13 | 4.96E-11 | 1.25E-12 | 1.36E-11 | 5.24E-13 | 1.65E-11 | 3.89E-13 |
| NGC 3621..... | 5.93E-12 | 2.90E-13 | 2.61E-11 | 1.80E-12 | 8.90E-12 | 8.13E-13 | 8.04E-12 | 6.17E-13 |
| NGC 3627..... | 1.07E-11 | 1.81E-13 | 3.40E-11 | 1.06E-12 | 1.19E-11 | 4.74E-13 | 1.53E-11 | 3.98E-13 |
| NGC 3938..... | 1.94E-12 | 6.98E-14 | 6.03E-12 | 2.00E-13 | 2.20E-12 | 1.46E-13 | 2.63E-12 | 6.73E-14 |
| NGC 4321..... | 1.38E-11 | 1.15E-13 | 5.45E-11 | 7.25E-13 | 1.75E-11 | 2.77E-13 | 1.64E-11 | 1.90E-13 |
| NGC 4450..... | 4.20E-13 | 5.47E-13 | 2.01E-12 | 1.22E-12 | 8.60E-13 | 6.50E-13 | 1.26E-12 | 3.77E-13 |
| NGC 4569..... | 6.21E-12 | 8.10E-14 | 1.68E-11 | 2.61E-13 | 6.28E-12 | 1.74E-13 | 9.74E-12 | 7.98E-14 |
| NGC 4579..... | 1.12E-12 | 1.88E-13 | 2.08E-12 | 5.98E-13 | - | - | 1.44E-12 | 2.68E-13 |
| NGC 4736..... | 1.84E-11 | 5.15E-13 | 6.36E-11 | 1.47E-12 | 2.28E-11 | 4.88E-13 | 3.22E-11 | 1.38E-13 |
| NGC 4826..... | 2.35E-11 | 1.09E-13 | 7.97E-11 | 6.60E-13 | 2.66E-11 | 2.63E-13 | 2.79E-11 | 1.73E-13 |
| NGC 5033..... | 1.42E-11 | 1.12E-13 | 4.19E-11 | 6.72E-13 | 1.47E-11 | 2.53E-13 | 1.62E-11 | 1.74E-13 |
| NGC 5055..... | 1.30E-11 | 1.25E-13 | 4.65E-11 | 7.39E-13 | 1.45E-11 | 2.96E-13 | 1.67E-11 | 2.22E-13 |
| NGC 5194..... | 1.88E-11 | 1.25E-13 | 6.25E-11 | 7.18E-13 | 2.03E-11 | 3.05E-13 | 2.29E-11 | 2.34E-13 |
| NGC 5195..... | 8.57E-12 | 1.19E-13 | 3.35E-11 | 6.18E-13 | 9.29E-12 | 2.17E-13 | 1.60E-11 | 9.63E-14 |
| NGC 5866..... | 1.56E-12 | 3.72E-13 | 7.19E-12 | 1.63E-12 | 1.75E-12 | 6.32E-13 | 2.40E-12 | 4.83E-13 |
| NGC 7331..... | 3.51E-12 | 1.18E-13 | 1.15E-11 | 6.28E-13 | 3.01E-12 | 2.11E-13 | 4.83E-12 | 8.52E-14 |
| NGC 7552..... | 4.79E-11 | 1.06E-13 | 1.68E-10 | 7.11E-13 | 6.67E-11 | 2.86E-13 | 5.35E-11 | 1.94E-13 |
| DCld 300.2-16.9 (A) | 6.19E-13 | 1.62E-14 | 2.29E-12 | 6.95E-14 | 6.47E-13 | 2.25E-14 | 7.37E-13 | 1.18E-14 |
| DCld 300.2-16.9 (B) | 9.48E-13 | 2.74E-14 | 2.87E-12 | 1.16E-13 | 9.20E-13 | 4.52E-14 | 1.01E-12 | 2.51E-14 |
| DCld 300.2-16.9 (C) | 8.52E-13 | 3.75E-14 | 2.49E-12 | 1.55E-13 | 8.39E-13 | 6.22E-14 | 8.85E-13 | 3.10E-14 |

Table 7—Continued

| Source | PAH (6.2 μm) ($\text{erg s}^{-1}\text{cm}^{-2}$) | Err (6.2 μm) ($\text{erg s}^{-1}\text{cm}^{-2}$) | PAH (7.7 μm) ($\text{erg s}^{-1}\text{cm}^{-2}$) | Err (7.7 μm) ($\text{erg s}^{-1}\text{cm}^{-2}$) | PAH (8.6 μm) ($\text{erg s}^{-1}\text{cm}^{-2}$) | Err (8.6 μm) ($\text{erg s}^{-1}\text{cm}^{-2}$) | PAH (11.3 μm) ($\text{erg s}^{-1}\text{cm}^{-2}$) | Err (11.3 μm) ($\text{erg s}^{-1}\text{cm}^{-2}$) |
|---------------------|---|---|---|---|---|---|--|--|
| (1) | (2) | (3) | (4) | (5) | (6) | (7) | (8) | (9) |
| DCld 300.2-16.9 (D) | 5.11E-13 | 8.59E-13 | 1.49E-12 | 2.57E-12 | 5.53E-13 | 1.59E-12 | 5.55E-13 | 1.29E-12 |

Table 8. Extinctions Measured from the Current Method, PAHFIT, and CAFE

| Source (1) | This Work | | PAHFIT | | CAFE | |
|---------------------|---------------------|---------------------------------|---------------------|---------------------------------|---------------------|---------------------------------|
| | $\tau_{9.7}$ (2) | $\text{Err}(\tau_{9.7})$ (3) | $\tau_{9.7}$ (4) | $\text{Err}(\tau_{9.7})$ (5) | $\tau_{9.7}$ (6) | $\text{Err}(\tau_{9.7})$ (7) |
| Mrk 33..... | < 1.53E-01 | – | – | – | 7.96E-02 | 2.38E-01 |
| NGC 24..... | < 8.60E-02 | – | – | – | 2.31E-01 | 8.35E-02 |
| NGC 337..... | < 5.30E-03 | – | 1.49E-01 | 1.77E-02 | 1.52E-01 | 1.36E-02 |
| NGC 628..... | < 7.96E-03 | – | 3.72E-02 | 3.17E-02 | 3.75E-02 | 1.85E-02 |
| NGC 855..... | < 3.61E-02 | – | 7.97E-02 | 8.04E-02 | 5.77E-02 | 7.36E-02 |
| NGC 925..... | < 1.15E-02 | – | – | – | < 5.67E-03 | – |
| NGC 1482..... | 3.71E-01 | 1.99E-03 | 3.03E-01 | 6.97E-03 | 8.15E-01 | 1.94E-03 |
| NGC 2403..... | < 4.40E-03 | – | 1.70E-01 | 2.35E-02 | 2.63E-01 | 1.52E-02 |
| NGC 2798..... | 1.58E-01 | 4.05E-03 | 1.96E-01 | – | 6.31E-01 | 4.14E-03 |
| NGC 2915..... | < 3.22E-02 | – | – | – | – | – |
| NGC 2976..... | < 3.80E-03 | – | – | – | – | – |
| NGC 3049..... | < 1.15E-02 | – | – | – | 2.76E-01 | 2.10E-02 |
| NGC 3184..... | < 7.28E-03 | – | 9.32E-02 | 3.58E-02 | – | – |
| NGC 3265..... | < 1.37E-02 | – | – | – | 1.70E-01 | 2.29E-02 |
| NGC 3351..... | < 4.75E-03 | – | 1.65E-02 | 6.68E-03 | 4.19E-01 | 5.05E-03 |
| NGC 3773..... | < 4.47E-02 | – | – | – | < 1.47E-02 | – |
| NGC 4254..... | < 1.21E-03 | – | 2.54E-01 | 8.68E-03 | 3.43E-01 | 4.10E-03 |
| NGC 4536..... | 1.67E-01 | 2.55E-03 | 4.05E-01 | 7.13E-03 | 6.85E-01 | 2.83E-03 |
| NGC 4559..... | < 8.31E-03 | – | 2.06E-01 | 3.35E-02 | 2.00E-01 | 1.89E-02 |
| NGC 4625..... | < 1.22E-02 | – | 1.77E-01 | 4.50E-02 | 7.38E-02 | 3.08E-02 |
| NGC 4631..... | 2.15E-02 | 2.86E-03 | 2.63E-01 | 7.42E-03 | 4.91E-01 | 3.09E-03 |
| NGC 5713..... | < 2.12E-03 | – | 6.89E-02 | – | 4.45E-01 | 3.56E-03 |
| NGC 6946..... | 2.45E-01 | 1.61E-03 | 3.40E-01 | 5.07E-03 | 7.53E-01 | 1.69E-03 |
| NGC 7793..... | < 9.03E-03 | – | – | – | 2.36E-01 | 1.85E-02 |
| NGC 1097..... | < 4.93E-02 | – | – | – | 4.04E-01 | 1.32E-03 |
| NGC 1266..... | 1.50E+00 | 2.56E-02 | 1.08E+00 | – | 1.86E+00 | 2.48E-02 |
| NGC 1512..... | < 2.25E-03 | – | – | – | 4.51E-01 | 1.67E-02 |
| NGC 1566..... | < 1.63E-03 | – | – | – | 1.28E-01 | 9.87E-03 |
| NGC 3198..... | 1.60E+00 | 1.99E-02 | 1.68E+00 | 1.82E-02 | 1.86E+00 | 1.88E-02 |
| NGC 3521..... | < 6.59E-04 | – | 3.52E-02 | 4.86E-03 | 1.94E-01 | 4.11E-03 |
| NGC 3621..... | < 2.19E-03 | – | 1.55E-01 | 1.63E-02 | 1.03E-01 | 9.22E-03 |
| NGC 3627..... | < 6.34E-04 | – | 1.24E-02 | – | 2.90E-01 | 7.43E-03 |
| NGC 3938..... | < 2.34E-03 | – | – | – | – | – |
| NGC 4321..... | < 3.54E-03 | – | 1.93E-01 | 9.62E-03 | 4.38E-01 | 4.87E-03 |
| NGC 4450..... | < 9.75E-03 | – | – | – | – | – |
| NGC 4569..... | < 1.71E-03 | – | – | – | – | – |
| NGC 4579..... | 1.88E-01 | 2.40E-02 | – | – | 2.31E-01 | 2.07E-02 |
| NGC 4736..... | < 1.02E-04 | – | – | – | – | – |
| NGC 4826..... | < 4.21E-04 | – | 1.16E-01 | 4.44E-03 | 4.09E-01 | 2.32E-03 |
| NGC 5033..... | < 1.21E-02 | – | 1.34E-01 | – | 4.33E-01 | 4.27E-03 |
| NGC 5055..... | < 1.13E-03 | – | 2.07E-01 | – | 3.89E-01 | 4.97E-03 |
| NGC 5194..... | < 3.70E-04 | – | 1.51E-01 | 4.52E-03 | 3.21E-01 | 3.31E-03 |
| NGC 5195..... | < 1.53E-02 | – | 4.09E-02 | – | – | – |
| NGC 5866..... | < 1.74E-02 | – | 2.02E-01 | – | 1.01E-01 | 1.72E-02 |
| NGC 7331..... | < 9.25E-04 | – | 6.83E-02 | – | – | – |
| NGC 7552..... | 8.60E-02 | 2.17E-03 | 1.66E-01 | 4.97E-03 | 6.18E-01 | 1.44E-03 |
| DCld 300.2-16.9 (A) | < 1.63E-02 | – | 3.23E-01 | 2.77E-02 | – | – |
| DCld 300.2-16.9 (B) | < 2.42E-03 | – | 1.92E-01 | 1.90E-02 | – | – |
| DCld 300.2-16.9 (C) | < 4.29E-03 | – | 2.22E-01 | 1.86E-02 | – | – |
| DCld 300.2-16.9 (D) | < 1.59E-02 | – | 2.19E-01 | 3.08E-02 | 5.42E-03 | 1.32E-02 |